Title
Non-standard Models of Dark Matter and Their Experimental Signatures

Permalink
https://escholarship.org/uc/item/4vk4r6q1

Author
Freytsis, Marat

Publication Date
2012

Non-standard Models of Dark Matter and Their Experimental Signatures

by

Marat Freytsis

A dissertation submitted in partial satisfaction of the
requirements for the degree of
Doctor of Philosophy
in
Physics
in the
Graduate Division
of the
University of California, Berkeley

Committee in charge:

Dr. Zoltan Ligeti, Co-Chair
Prof. Lawrence J. Hall, Co-Chair
Prof. Yasunori Nomura
Prof. Nicolai Reshetikhin

Spring 2012

Non-standard Models of Dark Matter and Their Experimental Signatures

Abstract

Non-standard Models of Dark Matter and Their Experimental Signatures

by

Marat Freytsis

Doctor of Philosophy in Physics

University of California, Berkeley

Dr. Zoltan Ligeti, Co-Chair

Prof. Lawrence J. Hall, Co-Chair

The weakly interacting massive particle (WIMP) paradigm gives an elegant mechanism for the generation of dark matter densities with the appropriate properties to be consistent with current observations. While in its minimal implementation, the only opportunity to test the reality of the scenario is by directly detecting the WIMP itself, cosmic ray anomalies observed several years ago imply the possibility of an extended dark matter sector in which secondary annihilations or decays can occur before interacting with the standard model. This opens up the possibility of detecting other parts of dark sector in a much wider set of experiments than those typically considered in connection to dark matter. In this dissertation I study several alternative models, capable of yielding signals across a broad range of experimental approaches.

I study the prospects for detecting a light boson X with mass $m_X \lesssim 100$ MeV at a low energy electron-proton collider. Focus is on the case where X dominantly decays to e^+e^- as motivated by recent "dark force" models. In order to evade direct and indirect constraints, X must have small couplings to the standard model ($\alpha_X \lesssim 10^{-8}$) and a sufficiently large mass ($m_X \gtrsim 10$ MeV). By comparing the signal and background cross sections for the $e^- p\, e^+ e^-$ final state, I conclude that dark force detection requires an integrated luminosity of around 1 ab^{-1}. This proposal is currently being implements by the DarkLight collaboration at the Thomas Jefferson National Accelerator Facility.

I also investigate the bounds on axion-like states from flavor-changing neutral current $b \to s$ decays, assuming the axion couples to the standard model through mixing with the Higgs sector. Such GeV-scale axions have received renewed attention in connection with observed cosmic ray excesses. I find that existing $B \to K\ell^+\ell^-$ data impose stringent bounds on the axion decay constant in the multi-TeV range, relevant for constraining the "axion portal" model of dark matter. Such bounds also constrain light Higgs scenarios in the next-to-minimal supersymmetric standard model. These bounds can be improved by dedicated searches in B-factory data and at LHCb.

While looking at direct dark matter detection experiments themselves, it is often assumed that the first evidence for dark matter will come from experiments probing spin-independent interactions, with much higher sensitivities due to coherence effects. I explore models that would be invisible in such experiments, but detectable via spin-dependent interactions. The existence of much larger (or even only) spin-dependent tree-level interactions is not sufficient, due to potential spin-independent subdominant or loop-induced interactions, and I find that in this way most models with detectable spin-dependent interactions would also generate detectable spin-independent interactions. Models in which a light pseudoscalar acts as the mediator seem to uniquely evade this conclusion. In presenting a particular viable dark matter model generating such an interaction, a tens of MeV–GeV-scale axion is found to be an attractive candidate independently of considerations presented earlier.

Dedicated to
the hope that there is always something new around the corner

Contents

List of Figures

List of Tables

Acknowledgments

I would like to thank my advisor, Zoltan Ligeti, for all of his insights and help over the years. He has been invaluable, not just for acquiring the technical understanding necessary, but also for providing a tempering combination of curiosity and skepticism that I hope to emulate in my career. I would also like to thank my other collaborators, from whom I have also learned much, Jesse Thaler, Tomer Volansky, Greg Ovanesyan, and Jon Walsh, as well as many other faculty, postdocs, and graduate students of the Berkeley CTP, without whose willingness to put up with my questions I wouldn't have realized that occasionally I do have interesting ones. I would also like to thank the Marco Battaglia group for, in the early stages of my PH.D., giving me a healthy respect for the work that experimentalists do to make their data usable, even if it did scare me away from being one myself. Finally, I need to thank my family for have supported me throughout my education and research so far, and who have worked hard to ensure that I had the opportunities to pursue my interests.

Chapter 1

Introduction

One of the most significant developments in our scientific understanding of the universe has been the realization—now from multiple independent observations over almost 80 years—that most of the matter in the universe could not be baryonic matter we are familiar with on Earth, but instead is composed of some as-yet unknown species we call dark matter (DM). Dark matter was first proposed by Fritz Zwicky in order to account for the radial velocity dispersion of galaxies in the Coma cluster [1]. It is this paper which introduced the term *dunkle (kalte) Meterie* (dark cold, *i.e.* non-relativistic, matter) into the field. Soon thereafter, the outer regions of galaxies were measured to have larger rotational velocities than was expected based on the distribution of luminous matter [2, 3]. It is worth noting that papers on galaxy clusters and galactic rotation curves did not make any connection between the two, and that both were received with a fair amount of skepticism at the time.

The turning point occurred when Ref. [4] showed that instabilities in models of galactic disks could be solved by the addition of a massive spherical component. Thereafter, previous measurements on galactic rotation curves [5], and new measurements of X-rays for hot gas in elliptical galaxies [6] were shown to be consistent in the amount of additional matter required. Additional evidence later came from gravitational lensing, which has allowed not just for the detection of the dark matter, but also for the construction of three-dimensional maps of its distribution [7]. The methods of X-ray spectrography and gravitational lensing recently converged in the observation of the Bullet cluster, formed in the collision of two large galaxy clusters [8]. By measuring the luminous and total mass separately using the two techniques, one could see the luminous matter lagging behind the total mass, as one would expect from a weakly-interacting dark matter. This observation effectively eliminated alternative theories for earlier observations, such as modifications of gravity, from serious contention.

Such astrophysical measurements also agree with cosmological ones stemming from the study of the cosmic microwave background (CMB). The WMAP experiment's best fit to the ΛCDM model's parameters yield the baryonic and total matter components in the universe as, respectively, $\Omega_b h^2 = 0.024 \pm 0.001$ and $\Omega_m h^2 = 0.14 \pm 0.02$, where $\Omega_m h^2$ is defined as the density relative to the critical density for eventual recollapse, $\Omega_m h^2 = \rho/\rho_{\text{crit}}$ [9]. The evidence points to dark matter making up over 80% of matter in the universe. Indirect measurement of the baryonic component from element abundances due to primordial nucleosynthesis [10, 11], the X-ray emission from hot gases from inverse scattering off the CMB due to the Sunyaev-Zel'dovich effect [12], and absorption lines from the intergalactic medium making up the Lyman-α forest [13] are all also consistent with the WMAP results. Simultaneously, analyses of large-structure formation also require a component with the properties of dark matter in order to generate the density perturbations necessary for galaxy and galactic cluster formation [14, 15].

Given all the current observational constraints, the best candidates for DM are new elementary particles [16, 17]. However, with all evidence for DM being of an astrophysical nature, and due to gravitational interactions, nothing is actually known about their microscopic properties, such as particle mass or non-gravitational interactions and their strength. A particularly attractive paradigm in this regard has come to be known as the weakly-interacting massive particle (WIMP). Extensions of the standard model (SM) often require some new symmetry in order to eliminate the generation of SM effective operators, such as those mediating proton decay, that are highly constrained by experiment. This typically has the effect of making the lightest particle having differing symmetry properties from the standard model to be absolutely stable. If such particles interact with the standard model with weak-scale coupling, and have weak-scale masses, then the Boltzmann equations indicate that upon falling out of thermal equilibrium in the early universe, the relic density generated is within the range necessary to act as the astrophysically-required dark matter.

Simultaneously, this provides a potential method for observing dark matter's particle properties, for if the particles making up DM were in equilibrium with the rest of the universe though weak-scale interactions in the early universe, the DM present in our galaxies right now should also interact with regular matter with weak interaction strength. This direct detection of DM, while requiring very clean, low-background experiments due to the extremely low rate of weak interactions, proceeds from general arguments, and is thus a promising avenue independent of the specific underlying model of dark matter.

Of course, such general considerations can only provide a very limited set of signals. Historically, connections were drawn to models of new physics which were attracting for independent reasons like solutions to the hierarchy problem, which also happened to have a particle with the properties given above. In this role, supersymmetry has traditionally been the leading candidate [18].

An alternative motivation for associating additional signals with the dark sector is provided by a series of astrophysical anomalies recorded several years ago. These include the WMAP Haze [19, 20], the PAMELA, FERMI, and H.E.S.S. e^+/e^- excesses [21, 22, 23, 24], and the INTEGRAL 511 keV excess [25, 26]. In explaining these observations, a general framework emerged, in which the DM itself remains at the weak scale as above, but now interacts with a GeV-scale boson [27, 28, 29, 30]. The excessed of electrons and positrons detected could then be explained by dark matter first annihilating into these light bosons, which then decay to the standard model, with only the light leptons being kinematically accessible. The existence of these light states motivates a fresh look at a lower-energy regime than that currently occupied by the collider high-energy frontier, for some aspects of the dark sector could be accessible there.

Purely theoretical, top-down, motivations for considering such particles also exist. Hidden sectors, coupling to the standard model though a kinetic mixing term such as $\epsilon F'_{\mu\nu} F^{\mu\nu}_{\mathrm{EM}}$, with $F'_{\mu\nu}$ the field strength tensor of some new gauge field, are generic in string compactifications [31, 32]. Correct masses and couplings can also be generated perturbatively if the standard model Higgs also couples to the hidden sector [33, 34, 35, 36] (models with often preserve supersymmetry as well).

In this dissertation, I survey the potential for various experimental approaches to probe the new framework discussed above. This involves considering new relatively low-energy collider experiements, connections to B-factory datasets, and a new look at traditional direct detection efforts.

In Ch. 2, I study the possibility of detecting a light boson X with mass $m_X \lesssim 100$ MeV at a low energy electron-proton collider. In the considered setup, X dominantly decays to e^+e^- as motivated by recent "dark force" models via the process $e^-p \to e^-p\,X \to e^-\,e^+e^-$. A notable advantage of such a setup is that the only background is produced by QED and extremely well understood, with hadrons enable to be produced kinematically, and thus nonperturbative effects kept at a minimum. After considering direct and indirect constraints already provided by existing data, I show that a significant portion of the accessible parameter space is left allowed. More precisely, X must have small couplings to the standard model ($\alpha_X \lesssim 10^{-8}$) and a sufficiently large mass ($m_X \gtrsim 10$ MeV). By comparing the signal and background cross sections for the final state, I conclude that dark force detection in the selected mass range for all couplings not already excluded requires an integrated luminosity of around 1 ab^{-1}. I also identify additional ways to extend the reach of such a setup, including vertex tracking to complete with beam dump searches and a search for an invisible decay of the X boson. This proposal is currently being implements by the DarkLight collaboration at the Thomas Jefferson National Accelerator Facility.

The setup of Ch. 2 is particularly well suited for models where light boson are present due to kinematic mixing with the U(1) electromagnetic (or hypercharge) field. Due to the required coupling to electrons, it proves unsuitable if such couplings are diractly proportional to mass, as is the case if the mixing is instead in the Higgs sector, as is the case in "axion portal"-type scenarios. In Ch. 3, I therefore consider bounds on axion-like states from flavor-changing neutral current $b \to s$ decays, assuming the axion couples to the standard model through mixing with the Higgs sector. I find that existing $B \to K\ell^+\ell^-$ data, already present in the BaBar and Belle B-factory datasets impose stringent bounds on an axion decay constant in the multi-TeV range. Independent of dark matter concerns, such bounds also constrain light Higgs scenarios in the next-to-minimal supersymmetric standard model. I proceed to discuss particular focused analyses by which these bounds can be improved by dedicated searches in B-factory data and at LHCb.

Finally, in Ch. 4, I look toward direct dark matter detection experiments themselves. Due to nuclear coherence effects yielding much larger effective couplings of DM to nucleons, it is often assumed that the first evidence for dark matter will come from experiments probing spin-independent interactions. I preform a model-independent analysis of possible couplings in order to identify models that would be invisible in such experiments, but detectable via spin-dependent interactions. The existence of much larger (or even only) spin-dependent tree-level interactions is found to not be sufficient, due to potential spin-independent subdominant or loop-induced interactions, and I find that in this way most models with detectable spin-dependent interactions would also generate spin-independent interactions though would be just as easily detectable. Models in which a light pseudoscalar acts as the mediator seem to uniquely evade this conclusion, which leads me again to consider a tens of MeV–GeV-scale axion from independent considerations to those presented in earlier chapters.

Chapter 2

Dark Force Detection in Low Energy *ep* Collisions[1]

2.1 Introduction

While the gravitational evidence for dark matter is overwhelming [5, 38, 9, 39], direct measurements of the spectrum and properties of dark matter have so far been elusive. However, recent astrophysical anomalies—such as those mentioned in Ch. 1—could be evidence for dark matter annihilation, decay, or up-scattering in our galactic halo. With these observations, an intriguing paradigm for dark matter has emerged, where TeV-scale dark matter interacts with a GeV-scale boson [27, 28, 29, 30]. This new light boson X typically has a mass in the range

$$2m_e < m_X \lesssim \text{few GeV}, \tag{2.1}$$

with an $\mathcal{O}(1)$ branching fraction $X \to e^+e^-$.[2]

What is the best way to look for light bosons with small couplings to the standard model? Indirect constraints from lepton anomalous magnetic moments require the coupling of X to leptons to be $\alpha_X \lesssim 10^{-8}$ [33, 41], much smaller than the electromagnetic coupling $\alpha_{\text{EM}} \simeq 1/137$.[3] Therefore, any direct production mode for X faces a large irreducible background from an equivalent process where X is replaced by an off-shell photon γ^*. A number of studies at lepton colliders have concluded that around 1 ab^{-1} of data is needed to see the process $e^+e^- \to \gamma + X$ [44, 33, 45, 46, 43, 36, 47]. While such large integrated luminosities have been achieved at the B-factories, it is worthwhile to consider alternative experimental setups that might be more easily scaled to multi-ab^{-1} data sets.

One standard method to find new particles with small couplings is fixed-target experiments, either with a high intensity beam on a thin target or a "beam dump" experiment

---

[1] This chapter, as well as App. A, was co-written with Grigory Ovanesyan and Jesse Thaler and published in [37]

[2] For a recent study of models with even lighter bosons, see Ref. [40].

[3] There are additional direct constraints on X from rare meson decays [33, 42, 41, 43].

on a thick target. As we will see, such experiments already constrain the X parameter space [48, 49]. Recent studies in Refs. [43, 50] have concluded that improved fixed-target experiments can cover a wide range of masses and coupling for X, especially if X has a sufficiently long lifetime to yield a displaced vertex or if X has a decay mode to penetrating muons. Even in the case of prompt X boson decay, the luminosity achievable in traditional fixed-target experiments approaches 1 ab^{-1}/day, so with good energy resolution and control over systematics, the irreducible γ^* background could be beaten by statistics, and one can simply search for electron pairs that reconstruct a narrow X resonance. However, full event reconstruction is impossible in this context, since one cannot measure the spectrum of the recoiling nucleus, so traditional fixed-target experiments lack a crucial kinematic cross-check that is available in lepton colliders.

In this chaper, we propose searching for an X boson in low-energy electron-proton collisions through the process

$$e^- p \to e^- p + X, \qquad X \to e^+ e^-. \tag{2.2}$$

With a high intensity electron beam on a diffuse hydrogen gas target, one combines the high statistics of a traditional fixed-target experiment with the full event reconstruction potential of a lepton collider. To our knowledge, this experimental setup was first suggested in Ref. [51], motivated by a different dark matter scenario with an invisibly decaying X boson [52]. In that context, the recoiling proton spectrum was crucial for discovery. Here, we focus on X bosons that decay visibly to e^+e^-. Like the fixed-target proposals in Refs. [43, 50], one is still looking for a narrow X resonance on top of a huge radiative QED background, but here the recoiling proton and electron spectrum can be used to over-constrain the kinematics.

As in Ref. [51], we consider an electron beam with energy $E_e \simeq 100$ MeV, where the scattering is dominated by elastic scattering and associated radiative processes. In particular, pion production is kinematically forbidden as are nuclear excitations. Such a setup is being actively considered for installation at the Free Electron Laser (FEL) at the Thomas Jefferson Lab National Accelerator Facility (JLab), replacing the laser cavity with a hydrogen gas target.[4] Where the reach in X parameter space overlaps, this proposal of a high intensity beam on a diffuse target is complementary to the proposal in Ref. [50] of a diffuse beam on a high density target. We will argue that for the same integrated luminosity, the X reach in ep collisions is comparable to e^+e^- and e^-e^- collisions. Since 1 ab^{-1}/month is achievable with the FEL beam on a hydrogen gas target, low-energy ep collisions are in principle a cost-effective way to search for the X boson.

In our study, we will focus on irreducible physics backgrounds and assume idealized detectors. While there are important experimental backgrounds, we will assume that these can be controlled using, for example, information about recoiling proton and electron. The JLab FEL setup is in principle sensitive to:

$$\begin{aligned} m_X < 2m_e &: X \to \gamma\gamma, \text{invisible} \\ 2m_e < m_X \lesssim 100 \text{ MeV} &: X \to e^+e^-, \gamma\gamma, \text{invisible} \end{aligned} \tag{2.3}$$

---

[4] For an alternative low-energy search using a positron beam incident on a hydrogen target, see Ref. [53].

In models with rich dark sectors, one can even imagine multi-body X decay modes or more than one X field [54, 46]. For simplicity, we will only look at $X \to e^+e^-$, and focus on the case that X couples only to electrons and not to protons. To capture a wide range of possible "dark boson" scenarios, we allow X to be scalar, pseudoscalar, vector, or axial-vector.[5]

In the next section, we summarize the conclusion of our study, that with 1 month to 1 year of running at the JLab FEL, one can probe an interesting parameter space for the X boson. In Sec. 2.3, we outline our theoretical setup, and review indirect and direct constraints on the X boson properties. We study the reach for X in ep collisions in Sec. 2.4 and show how a matrix element method can be used to extend the X boson reach. Comparisons to other X boson collider searches appear in Sec. 2.5. Two benchmark scenarios appear in Sec. 2.6, showing an example analysis strategy as well as a variety of kinematic distributions. We consider an alternative displaced vertex search in Sec. 2.7 and conclude in Sec. 2.8.

---

[5] In the case of a light vector boson, X is often referred to as a U-boson.

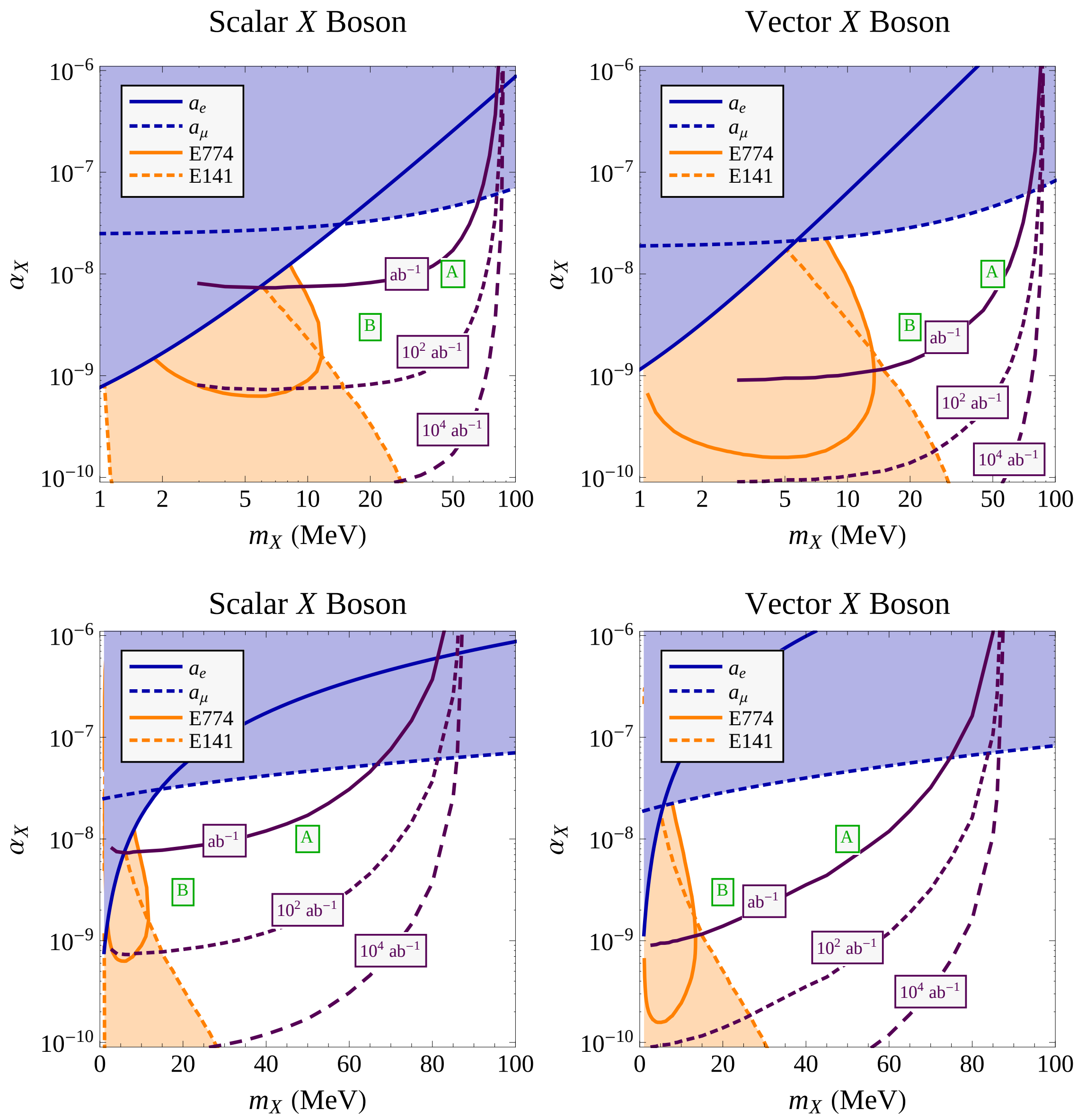

Figure 2.1: Summary of this study, showing constraints and reach on the m_X–α_X plane. The scalar couplings are on the left, vector couplings on the right. The top plots are logarithmic in m_X, while the bottom plots are linear in m_X to highlight the relevant parameter space. Blue curves: bounds from lepton anomalous magnetic moments. Orange curves: bounds from prior beam dump experiments. Purple curves: luminosity necessary to achieve $S/\sqrt{B} = 5$ assuming $m_{e^+e^-}$ invariant mass resolution of 1 MeV, and a detector acceptance of $-2 < \eta < 2$, $\mathrm{KE}_p > 0.5$ MeV, and $\mathrm{KE}_{e^\pm} > 5$ MeV. The reach in the pseudoscalar and axial-vector cases are the same as the scalar and vector cases, respectively, but the anomalous magnetic moment bounds differ. The points labelled “A” and “B” correspond to the benchmark scenarios studied in Sec. 2.6.

2.2 Summary

The key results of our study are summarized in this section. We take an electron beam with a fiducial energy of 100 MeV, incident on a proton target at rest in the lab frame. At the FEL facility, the proton target is likely to be a hydrogen gas storage cell, which is sufficiently diffuse to allow recirculation of the FEL beam [55]. In Fig. 2.1, we show a plot of the m_X–α_X plane for the case that X has scalar or vector couplings to electrons.[6] Here, m_X is the mass of the X boson, and $\alpha_X \equiv \lambda_X^2/4\pi$ is the coupling of the X boson to electrons, normalized such that it can be roughly compared with $\alpha_{\text{EM}} \simeq 1/137$.

There are three sets of curves shown on the m_X–α_X plane:

- Indirect constraints from anomalous magnetic moments. An X boson that couples to electrons will radiatively generate a_e and, assuming lepton universality, a_μ. The shaded region is excluded, as explained in Sec. 2.3.1.

- Direct constraints from beam dump experiments. When the X boson is sufficiently long-lived, high intensity beam dump experiments are sensitive to the decay $X \to e^+e^-$. The shaded region is excluded, as explained in Sec. 2.3.2.

- Discovery reach in *ep* scattering. As detailed in Sec. 2.4.2, we use an idealized detector with pseudorapidity coverage $-2 < \eta < 2$ (i.e. tracking up to 15.4° of the beamline), kinetic energy thresholds of $\text{KE}_p > 0.5$ MeV and $\text{KE}_{e^\pm} > 5$ MeV, and invariant mass resolution of 1 MeV. Assuming no systematic errors, the curves show the integrated luminosity needed to achieve a 5σ discovery with statistics alone, i.e. $S/\sqrt{B} = 5$ in a 1 MeV resolution bin centered around m_X. If the energy resolution is improved, this integrated luminosity required for discovery improves linearly. Also, the reach of the experiment can be further improved using a matrix element method, as proposed in Sec. 2.4.3.

In addition, the points labelled "A" and "B" indicated the benchmark scenarios considered in Sec. 2.6.

We see that with an integrated luminosity of 1 ab^{-1}, there is a range of X boson masses and couplings that are consistent with known bounds but visible in low energy *ep* scattering. With an average current of 10 mA, the FEL beam produces 6×10^{16} electrons per second [56], while a hydrogen gas target of thickness 10^{19} cm^{-2} is expected to be technically feasible [55]. Thus, the expected luminosity of the JLab FEL setup is 6×10^{35} cm^{-2} s^{-1}, which corresponds to 1.6 ab^{-1}/month. With one month to one year of running, such a facility could probe an interesting range of X boson masses and couplings.

---

[6] The plots for pseudoscalar and axial-vector couplings appear later in the text. The reach for the pseudoscalar (axial-vector) is the same as the scalar (vector), but the magnetic moment bounds differ.

2.3 New Light Bosons

We consider four kinds of coupling for the new light boson X: scalar, pseudoscalar, vector, and axial-vector. For simplicity, we assume that X only couples to electrons (and other charged leptons), and show in App. A.5 that proton couplings do not drastically change our conclusions. In the scalar and pseudoscalar cases, we augment the standard model with a new boson X that couples to the electron field ψ_e as

$$\mathcal{L}_{s/p} = \overline{\psi}_e \left(\lambda_s + \lambda_p \gamma^5\right) \psi_e X. \tag{2.4}$$

For the vector and axial-vector cases, we add a massive vector X_μ with couplings

$$\mathcal{L}_{v/a} = \overline{\psi}_e \left(\lambda_v \gamma^\mu + \lambda_a \gamma^\mu \gamma^5\right) \psi_e X_\mu. \tag{2.5}$$

While more exotic operators are possible, Eqs. (2.4) and (2.5) cover the generic possibilities for how X can couple to electrons.

In a complete theory, there is usually some kind of lepton universality, yielding equivalent couplings of X to muons and taus. Assuming that X does not introduce lepton flavor violation, then the coupling of X to the different leptons will either be approximately equal or proportional to the lepton masses.[7] As we will see below, though, if the couplings are indeed proportional to the lepton masses, then the constraints from a_μ exclude any of the interesting region for this study.

For convenience where relevant, we define

$$\lambda_X \equiv \sqrt{|\lambda_s|^2 + |\lambda_p|^2} \text{ or } \sqrt{|\lambda_v|^2 + |\lambda_a|^2}, \qquad \alpha_X \equiv \frac{\lambda_X^2}{4\pi}. \tag{2.6}$$

In the text, we work in the limit $m_e \ll m_X$, and present formulas for finite m_e in App. A.1.

2.3.1 Indirect Constraints

Previous studies of the indirect constraints on the X boson appear in Ref. [33]. The strongest indirect bounds comes from the effect of the X boson on the anomalous magnetic moments of the electron and muon, a_e and a_μ, arising from X boson loops. We take the limits to be $\delta a_e < 1.7 \cdot 10^{-11}$ [41] and $\delta a_\mu < 2.9 \cdot 10^{-9}$ [57]. However, it should be noted that in the case of vector or pseudoscalar couplings, the a_μ bound should not be taken as a hard constraint. We have chosen a limit such that the addition of the X boson does not significantly change the agreement between experiment and theoretical predictions. Yet with the currently observed muon magnetic moment anomaly the agreement between theory and experiment in a_μ actually improves for vector or pseudoscalar couplings just above the constraint.

---

[7] In the special case that X is a pseudo Nambu-Goldstone boson (such as in Ref. [30]), one expects $\lambda_p = m_\ell / f_a$, where m_ℓ is the mass of the lepton and f_a is the decay constant.

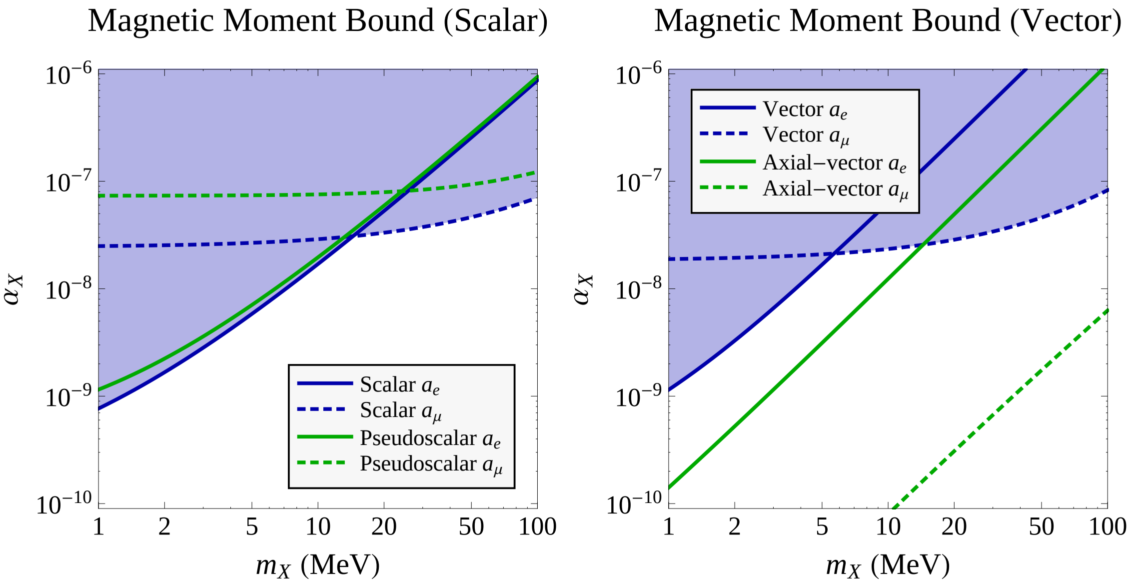

Figure 2.2: Constraints on the X boson mass m_X and coupling α_X from anomalous magnetic moments, $a_e = (\frac{g-2}{2})_e$ and $a_\mu = (\frac{g-2}{2})_\mu$. We assume lepton universality with $\alpha_X^e = \alpha_X^\mu$.

If the couplings of the X boson to leptons were proportional to the lepton masses, then the a_μ constraint would exclude the interesting parameter range for this study. The reason is that the production rate for X bosons is proportional to α_X^e, but the constraint on a_μ is on $\alpha_X^\mu = \alpha_X^e (m_\mu/m_e)^2$. Thus, the effective bound on α_X^e is almost 5 orders of magnitude stronger than if $\alpha_X^e = \alpha_X^\mu$. For this reason, we focus on the case with lepton universal couplings.

The formula for the anomalous magnetic moment appears in App. A.1.1, mirroring known results from Refs. [58, 59]. Taking the limit $m_e \ll m_X$,

$$\delta a^e_{s/p} = \frac{1}{16\pi^2}\frac{m_e^2}{m_X^2}\left(\lambda_s^2\left(\log\frac{m_e^2}{m_X^2} - \frac{7}{6}\right) - \lambda_p^2\left(\log\frac{m_e^2}{m_X^2} - \frac{11}{6}\right)\right), \tag{2.7}$$

$$\delta a^e_{v/a} = \frac{1}{16\pi^2}\frac{m_e^2}{m_X^2}\left(\lambda_v^2\frac{4}{3} - \lambda_a^2\frac{20}{3}\right) + \mathcal{O}\left(\frac{m_e^4}{m_X^4}\right). \tag{2.8}$$

The calculation in the muon case does not admit a simple approximate form since $m_\mu \approx m_X$ in the range under consideration, so one must use the full formula from the appendix.

The constraints on the coupling of the X boson to electrons and muons are shown in Fig. 2.2, assuming $\alpha_X^e = \alpha_X^\mu$. For $m_X \gtrsim 10$ MeV, the a_μ bound dominates, giving roughly $\alpha_X \lesssim 10^{-7} - 10^{-8}$, except for the axial-vector case, for which the bound excludes much of the interesting parameter space for this study. Thus, we see that the coupling of the X boson to leptons must be 5 to 7 orders of magnitude weaker than the electromagnetic coupling $\alpha_{\rm EM} \simeq 1/137$.

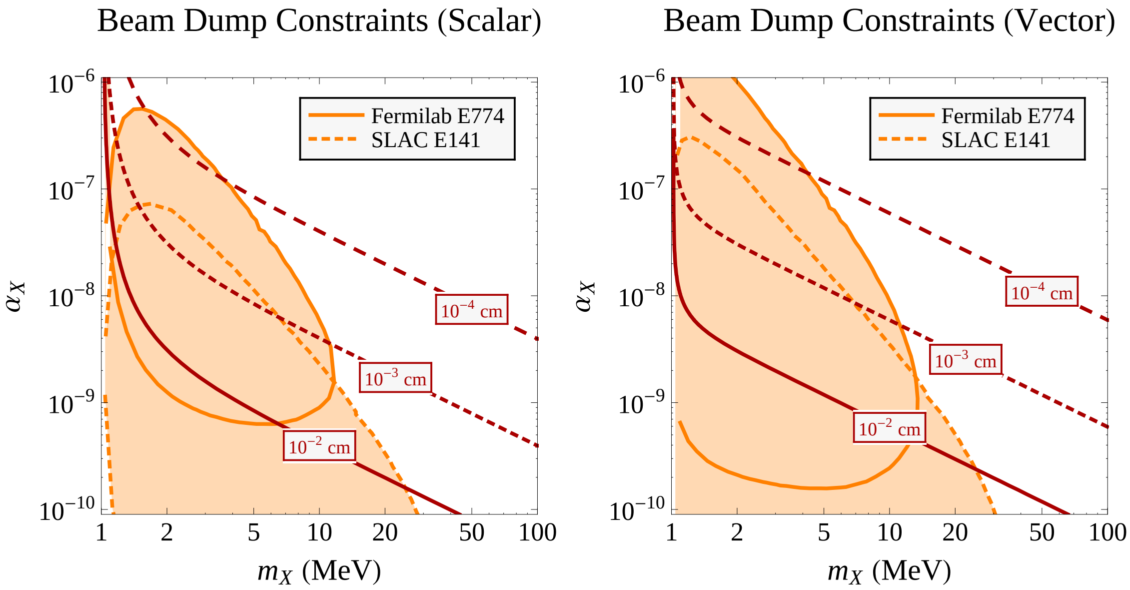

Figure 2.3: Constraints on the X boson mass m_X and coupling α_X due to prior beam dump experiments, E774 at Fermilab and E141 at SLAC. The red lines correspond to X boson lifetimes. The lifetime (and corresponding beam dump constraints) of the pseudoscalar and axial-vector are nearly identical to the scalar and vector, respectively, except in the very low mass region.

2.3.2 Direct Constraints

The strongest direct constraints on the X boson come from beam dump experiments. As explained below, other direct constraints from rare meson decay modes, production from cosmic rays, or supernova cooling either fall outside the parameter space under consideration or are subsumed by the beam dump and anomalous magnetic moment constraints.

Despite the small coupling of the X boson to electrons, it still has a sizable production rate in beam dump experiments because of their very high luminosity. As long as the X boson lifetime is sufficiently long, the decay of X to electrons happens at finite displacement from the target. Using the couplings in Eqs. (2.4) and (2.5), the X boson width has been calculated in App. A.1.2. In the limit $m_e \ll m_X$, the width is linear with mass

$$\Gamma_{s/p} = \frac{\alpha_X}{2} m_X + \mathcal{O}\left(\frac{m_e^2}{m_X^2}\right), \qquad \Gamma_{v/a} = \frac{\alpha_X}{3} m_X + \mathcal{O}\left(\frac{m_e^2}{m_X^2}\right). \tag{2.9}$$

Roughly, the beam dump constraints are relevant for lifetimes longer than $\sim 10^{-3}$ cm.

As discussed in Ref. [50], the two experiments relevant in the parameter space of interest are Fermilab's E774 and SLAC's E141 electron beam dumps, both originally searches for MeV-scale axions. E774 consisted of a dump of $5.2 \cdot 10^9$ electrons at 275 GeV on a 19.6-cm tungsten target, with a 20-cm wide detector 7.25 meters away. With the trigger requiring a decay product with energy of 2.75 GeV, 17 events, i.e., decays reconstructing to a mass resonance, would qualify for discovery [49]. The E141 beam dump consisted of a 9 GeV source with $2 \cdot 10^{15}$ electrons incident on a 12-cm tungsten target with a detector 35 m away down a 7.5-cm pipe. The trigger consisted of a decay with at least 4.5 GeV energy deposition on the detector. Given the background, 1000 events would constitute discovery, with the greater number of events necessary due to the lack of veto counters on this experiment [48].

To determine the excluded parameter space, we mirror the analysis of the vector case from Ref. [50] and extend it to the other X boson couplings. In particular, we use an approximate formula for the cross section and kinematics for X boson production and decay in order to model the coherent nuclear effects involved in the beam dump experiments. The excluded regions are shown in Fig. 2.3, with X boson lifetimes overlayed. The upper diagonal boundary of the excluded region corresponds to when the X boson lifetime is sufficiently short that X decays to electrons within the shielding of the beam. Naively, one would then expect the upper boundary to be along lines of constant lifetime. The discrepancy is due to the fact that lower-mass bosons are created with higher average Lorentz factors, allowing more potential X boson events to be seen in the detector downstream past the shielding. The lower boundary of the excluded region is determined by the rate of X boson production. If the typical X boson decays past the detector, then this boundary would be approximately horizontal. The reason is that for an X decay length ℓ_X and distance to detector L, the fraction of decayed X bosons, approximately L/ℓ_X, cancels the $1/m_X$ mass dependence in the production rate. When the decay length becomes less than the distance to the detector, the lower boundary rises at a diagonal.

Note that the beam dump constraints exclude any of the parameter space accessible in this search where X is a very long-lived particle. This is important, because if X were too long-lived, then it would decay outside of a typical detector volume, and be inaccessible in the *ep* scattering experiment under consideration. Regions of moderate X lifetime are still allowed, so the X might decay with a displaced vertex in *ep* scattering. We will return to this possibility in Sec. 2.7.

We can also consider direct constraints that rely on model-dependent assumptions on hadronic couplings. Most of these end up being either irrelevant or superfluous in the region of interest. For example, B-factories provide constraints on the X boson coupling constant though rare Υ decays, but such constraints currently only apply for $m_X \geq 2m_\mu$, and are thus beyond the range of interest [60]. A recent BaBar analysis [61] does constrain dark force models, but relies on a model-dependent signature present only in non-Abelian dark sectors. Some proton beam dumps, such as CHARM at CERN [62] do cover some of the parameter space in question, but rule out areas of parameter space already covered by the electron beam dumps. There also exist bounds from the rare pion decay mode $\pi^0 \to e^+e^-$ [42], which can place some additional constraints in a small region close to where the electron and muon anomalous magnetic moment bounds intersect.

There are also potential bounds that end up being irrelevant since the X boson is short-lived in the parameter space of interest. For example, X bosons could potentially be observed due to cosmic rays interacting with the earth, such that X bosons could be seen at detectors such as AMANDA and IceCube. However, these experiments rule out couplings that are smaller (equivalently, lifetimes that are longer) than those we are trying to observe here [50]. Additionally, neutrino searches such as LSND and MiniBooNE can also be used to place constraints on MeV scale bosons, but again at much lower couplings [63]. Another constraint comes from supernovae, where X boson production could lead to additional cooling of the core. However, the X boson would have to travel at least $\mathcal{O}(10\text{ km})$ in order to escape the core. Thus, such constraints require lifetimes for the boson to be several orders of magnitude longer than those considered in this search. Detailed calculations done for the axion case in Ref. [64] agree with this rough estimate.

Assuming hadronic couplings, strong bounds on the X boson might be obtained from data mining the existing pion decay data set from the KTeV collaboration.[8] Over the course of two runs, approximately $1.8 \cdot 10^6$ decays of $\pi^0 \to e^+e^-\gamma$ with invariant mass $m_{e^+e^-} > 65$ MeV have been reconstructed [65]. Assuming this can be extended to the whole invariant mass range, this should give a data set of close to $6 \cdot 10^7$ decays. One can then look for an X boson by looking for a small peak in the $m_{e^+e^-}$ spectrum, in a search much like the $e^+e^- \to e^+e^-\gamma$ search described later in Sec. 2.5. Using an approximate formula for the reach from Ref. [43], a search looking for X bosons should be able to detect couplings as low as $\alpha_X \sim \text{few} \times 10^{-8}$, an improvement on current bounds, but not matching the reach for the search proposed in this chapter.

2.4 *ep* Scattering Below the Pion Threshold

We now describe a promising venue for a light X boson search: low-energy ep scattering. Despite the above constraints on α_X, the cross section for X boson production in $ep \to ep+X$ is quite large, on the order of picobarns. The X would then decay promptly to e^+e^-, yielding an $e^-p\,e^+e^-$ final state where the electron/positron pair reconstructs a narrow X resonance. The envisioned experimental setup is sketched in Fig. 2.4, where a high intensity electron beam is incident on a hydrogen gas target. Assuming a sufficiently large tracking volume, all four outgoing fermions can in principle be reconstructed.

As we will see, the primary challenge for this search is the large irreducible QED background, roughly four orders of magnitude larger than the signal, making this a background limited search. In this section, we summarize the signal and background calculations and present the reach for the X boson, first using simple cuts on the detector geometry and then including full information about the event kinematics through a matrix element method.

2.4.1 Cross Section Calculations

In the range of couplings allowed by the anomalous magnetic moment bounds, the width of the X boson is an eV or smaller. Therefore, to calculate the signal rate for $e^-p \to e^-p\,e^+e^-$, we can safely use the narrow width approximation. Since the angular distribution of the decay $X \to e^+e^-$ is relevant for understanding the vector couplings, we maintain full

---

[8] We thank Maxim Pospelov for bringing this possibility to our attention.

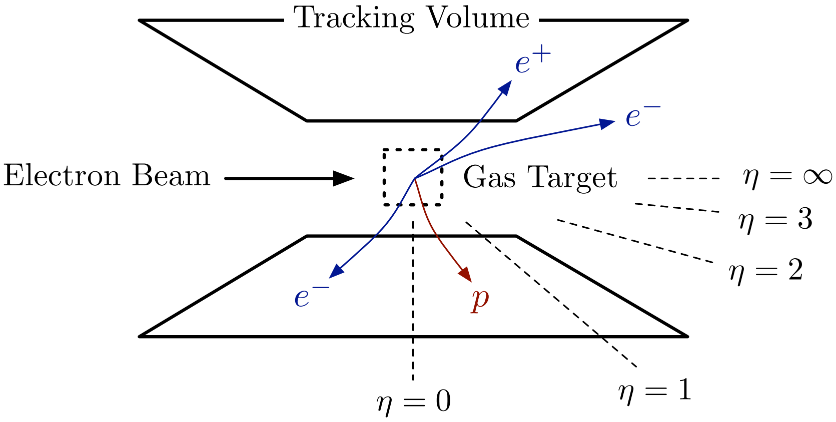

Figure 2.4: The envisioned experimental setup to probe $e^- p \to e^- p\, e^+ e^-$ scattering, where a high intensity electron beam is incident on a diffuse hydrogen gas target. In order to reconstruct all four outgoing fermions, a large tracking volume is needed, and we will consider $-2 < \eta < 2$ coverage as a benchmark. While this is a fixed target experiment where most of the tracks go in the forward direction, we take a detector symmetric around $\eta = 0$ for simplicity. For reference, $\eta = 1$ is an angle to the beamline of $\theta = 40.4°$, $\eta = 2$ is $\theta = 15.4°$, $\eta = 3$ is $\theta = 5.7°$, and $\eta = 4$ is $\theta = 2.1°$.

polarization information in the signal process $e^- p \to e^- p\, e^+ e^-$ as explained in App. A.2. We used a custom matrix element/phase space generator to calculate the signal cross sections, and checked the results with `CompHEP 4.5.1` [66]. In particular, we used `CompHEP` to verify that any interference between the signal and background processes is a subdominant effect given the narrowness of the X boson.

For the couplings in Eqs. (2.4) and (2.5), the diagrams that contribute to the signal cross section appear in Fig. 2.5. In the limit that $m_e \to 0$, the cross section for the pseudoscalar (axial-vector) case is identical to the scalar (vector) case. While we keep finite m_e effects in our calculations, we will only show reaches for the scalar and vector cases, since the finite m_e effects are small. While there could be contributions to the signal from X boson couplings to the proton, we argue in App. A.5 that such effects can be ignored. In reconstructing the X resonance, there is combinatoric confusion about which electron to pair with the positron, and this confusion is included in our plots. We neglect the electromagnetic form factor of the proton, which is a fair approximation since we are considering incoming electron energies $E_e \ll m_{\text{proton}}$.

The background to $e^- p \to e^- p\, e^+ e^-$ is due to QED radiative processes $e^- p \to e^- p + \gamma^*$ with $\gamma^* \to e^+ e^-$ and to the Bethe-Heitler trident process, shown in Fig. 2.6. Details of these backgrounds appear in App. A.3, where we again ignore the proton form factor. We calculated the background cross sections using a custom phase space generator interfaced with the stand-alone version of `MadGraph 4.4.17` [67], and checked the results using `CompHEP`.

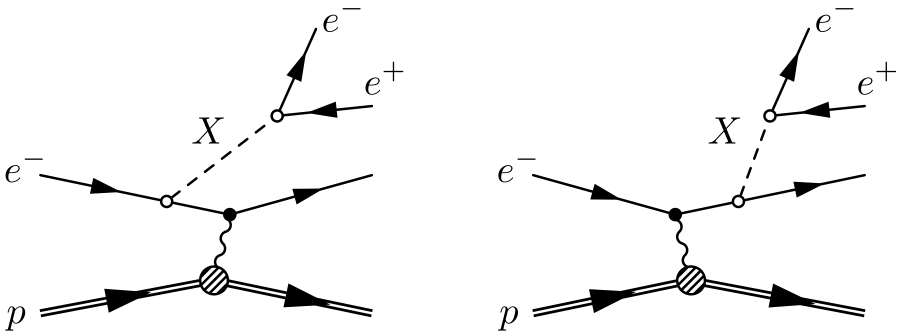

Figure 2.5: Diagrams contributing to the X boson signal. Here, the X boson propagator is evaluated in the narrow-width approximation.

Because we are considering $m_X \sim E_e$, thinking of the γ^* as coming from initial or final state radiation is not a good approximation to the background process. In the region of phase space where an e^+e^- pair fakes an X resonance, the photon is far off-shell relative to the energy scales involved, so we are far away from soft-collinear limit. In particular, it should be noted that considerable (constructive) interference increases the background above naive expectations from the Weizsäcker-Williams approximation. To give a sense of how important this interference is, one sees changes on the order of 10% in cross sections with e^-p collisions versus $e^-\bar{p}$ collisions, whereas the sign of the proton charge would be irrelevant in the Weizsäcker-Williams picture.

In principle, there is another background we should consider. Since the proposed JLab FEL experiment is really an electron-hydrogen gas collider, one might be concerned about backgrounds from e^-e^- collisions. In fact, this is only an issue for very low values of m_X. For an electron beam with energy 100 MeV, the center-of-mass energy of e^-e^- collisions is around 10 MeV, so radiative Møller scattering is only relevant for $m_X \lesssim 10$ MeV. We saw in Sec. 2.3.2 that such light bosons are already ruled out by direct constraints. Moreover, given the fact that we imagine using the recoiling proton and electron momentum as a handle on the collision process, particle identification should be sufficiently robust to distinguish e^-e^- from ep collisions. Finally, there are important experimental backgrounds, including event pileup and photon conversion, which we do not address in this study.

2.4.2 Resonance Reach

Since the X boson is very narrow, with infinitely good mass resolution and the relatively large X boson production rate, one could easily produce the few events required in the same e^+e^- invariant mass bin to conclude the existence of X. In practice, though, one must take into account finite experimental resolution. In Fig. 2.7, we plot the signal cross sections for fixed $\alpha_X = 10^{-8}$ as a function of m_X, and compare it to the QED background, imposing a cut that at least one e^+e^- pair within a 1 MeV mass bin around m_X. One can see that

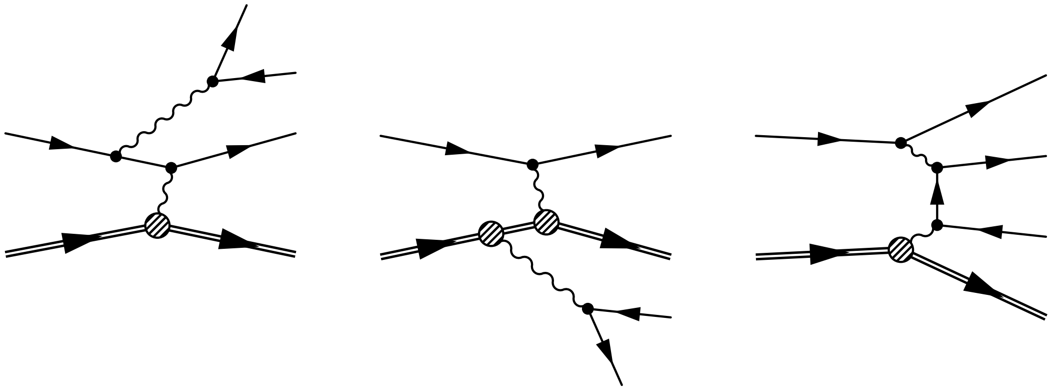

Figure 2.6: Representative diagrams contributing to the radiative QED background. With indistinguishable outgoing electrons, there are 12 diagrams in total, consisting of γ^* emission off the incoming/outgoing electron/proton lines and the Bethe-Heitler process. In this study, we ignore the electromagnetic form factor of the proton, which contributes at most a 5% correction.

the signal cross section is in the range 10^{-2} to 10^{2} pb, but the background size is generically four orders of magnitude larger than signal. Thus, one will need a very large integrated luminosity to establish the signal over statistical fluctuations in the background.

To assess the reach of experiment precisely, one would need to know the true resolution, efficiency, and dimensions of the detector. As a rough approximation to the detector geometry, we assume full azimuthal coverage, and consider a detector with pseudorapidity coverage of

$$-2 < \eta < 2, \qquad \eta \equiv -\ln\left(\tan\frac{\theta}{2}\right) \tag{2.10}$$

(i.e. a tracking system that covers angles as close as 15.4° to the beam line). As we will see later in Fig. 2.8, a more aggressive $-3 < \eta < 3$ coverage (i.e. tracking up to 5.7°) actually has a comparable reach. We also impose a constraint on the kinetic energy of the outgoing particles:

$$\mathrm{KE}_p > 0.5\ \mathrm{MeV}, \qquad \mathrm{KE}_{e^\pm} > 5\ \mathrm{MeV}. \tag{2.11}$$

Note that in this idealized study, knowing the proton's kinematics is strictly speaking not necessary, since the proton four-momentum could be reconstructed from the beam energy and the measured outgoing electron/positron tracks. In an actual experimental context, however, overconstraining the full kinematics will be crucial. Although we do not consider reducible backgrounds here, information on the proton is necessary to avoid mistaking pileup from multiple elastic- and Møller-scattering events for signal or irreducible background. Additionally, having full kinematic information means that the spread in the beam energy does not directly translate to smearing in the mass resolution, mitigating this intrinsic source of uncertainty.

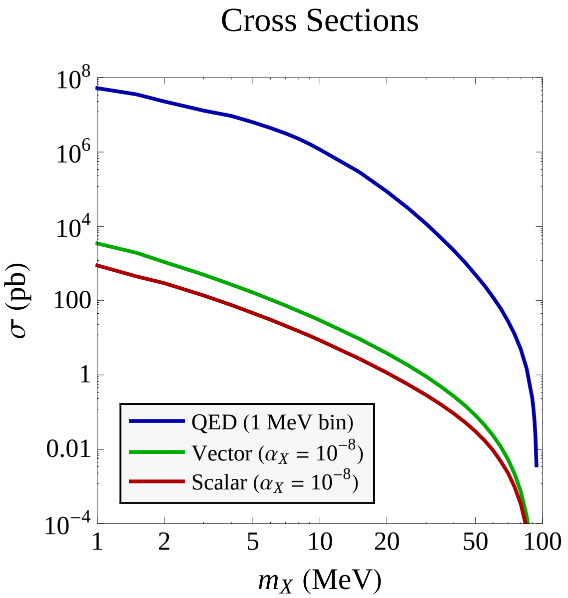

Figure 2.7: Cross section for the X boson signal with $\alpha_X = 10^{-8}$ and the QED background imposing that at least one e^+e^- pair is in the $m_X \pm 0.5$ MeV invariant mass bin. The signal cross section scales linearly with α_X. Generically, the expected signal is four orders of magnitude smaller than the background.

While we assume the detector is symmetric about $\eta = 0$, recall that we are considering a fixed target geometry, so the tracks dominantly appear in the forward part of the detector. Since the QED background has a large forward peak, the pseudorapidity restriction does improve the signal to background ratio compared to what is shown in Fig. 2.7. We only keep events where all four outgoing fermions are contained in the tracking volume.

As a baseline, we assume that the e^+e^- invariant mass resolution is 1 MeV of the target m_X value. We then calculate the value of α_X such that for a given luminosity, one can achieve a 5σ discovery with statistical uncertainties alone, meaning we find where $S/\sqrt{B} = 5$ in a 1 MeV mass bin centered on a candidate X mass. Since the background is relatively smooth over the kinematic range of interest, the required luminosity for discovery decreases linearly as the resolvable mass difference decreases:

$$\mathcal{L}(x \text{ MeV resolution}) = x\mathcal{L}(1 \text{ MeV resolution}). \tag{2.12}$$

The reach for 1 MeV resolution was shown above in Fig. 2.1, taking 3 MeV $< m_X <$ 100 MeV.

While we assume 1 MeV resolution as a conservative estimate, it is worth asking how this might be improved. In fact, a more accurate baseline would be 1% mass resolution [68], making required luminosity scale linearly with m_X as well. One can try to improve this resolution, either by increasing the strength of the magnetic field in the tracking region, or the size of the region itself, but at the low energies under consideration, multiple scattering is appreciable and puts fundamental constraints on the achievable resolution. We estimate

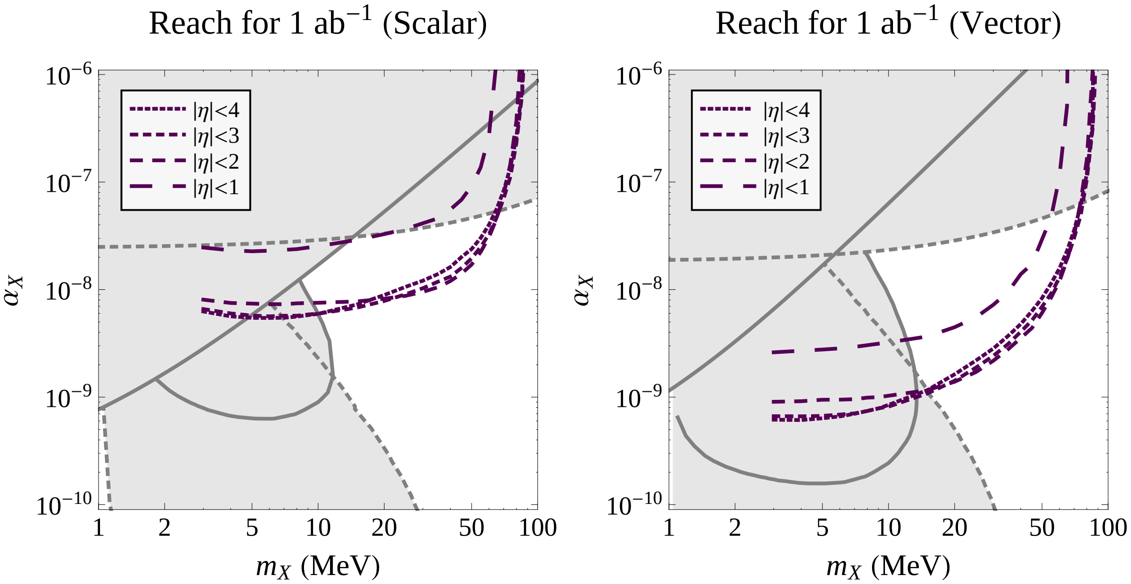

Figure 2.8: Reach plots for variable detector angular acceptance η. The grey shaded regions correspond to the indirect and direct constraints from Sec. 2.3. In all cases, we impose the criteria $\mathrm{KE}_p > 0.5$ MeV and $\mathrm{KE}_{e^\pm} > 5$ MeV. We again take an integrated luminosity of 1 ab^{-1} and assume 1 MeV $m_{e^+e^-}$ resolution. For small values of η, the reach deteriorates because the signal efficiency decreases. For large values of η, the reach deteriorates because the background has a large forward peak.

that achieving 0.5% mass resolution should be possible, but greater improvements would be extremely difficult.

In Fig. 2.8, we show how the reach changes as the angular acceptance is varied. Going from $|\eta| < 2$ to $|\eta| < 3$ slightly improves the reach for smaller values of m_X, though the effect is mild. As we will discuss more below, the reason the $|\eta| < 2$ geometry is so effective is that by cutting out the phase space close to the beam line, we decrease the background rate without sacrificing much on signal acceptance.

This $S/\sqrt{B}$ procedure to establish reach is only a crude estimate of the true sensitivity. In practice, the actual background distribution would have to be fit from the data using some kind of sidebanding procedure (see Sec. 2.6), and one also must pay a trials factor in looking for an invariant mass peak since the X boson could be anywhere. With those caveats, we see that with 1 ab^{-1} of data, one begins to probe the interesting parameter regime for the X boson.

2.4.3 Reach with Matrix Element Method

The reach plots in Fig. 2.1 do not include any kinematic cuts apart from the $-2 < \eta < 2$ cut on detector acceptance and the kinetic energy restriction from Eq. (2.11). As we will see in Sec. 2.6, the kinematic distributions for signal events do differ from the background, so one might hope that a set of optimized kinematic cuts might improve the reach for the X boson. Here we show that a factor of 3 improvement in the reach is in principle possible by using complete kinematic information via a matrix element method [69, 70].

The matrix element method is often described in terms of a discriminant function [71], but the essential statistics can be understood by considering a weighted measurement. For a very narrow resonance X, the signal and background matrix elements for $e^- p \to e^- p\, e^+ e^-$ are essentially functions of $\tilde{\Phi}_4$, which is the four-body final state phase space Φ_4 with an additional restriction that one of the electron/positron pairs reconstructs a given value of m_X. For simplicity, we will use the notation Φ to refer to $\tilde{\Phi}_4$.

For a differential signal cross section times luminosity $S(\Phi)$ and differential background times luminosity $B(\Phi)$, the naive reach calculation is equivalent to integrating over all of Φ with unit weight:

$$S = \int \mathrm{d}\Phi\, S(\Phi), \qquad B = \int \mathrm{d}\Phi\, B(\Phi). \tag{2.13}$$

The reach is determined by calculating $S/\delta B = S/\sqrt{B}$, where δ refers to the statistical uncertainty in the measurement. Now consider a weighted measurement

$$S_{\text{eff}} = \int \mathrm{d}\Phi\, S(\Phi) w(\Phi), \qquad B_{\text{eff}} = \int \mathrm{d}\Phi\, B(\Phi) w(\Phi), \tag{2.14}$$

where $w(\Phi)$ is some weight function. For example, a weight function corresponding to hard kinematic cuts is one where $w(\Phi)$ equals either 0 or 1. However, more general weight functions still give well-defined measurements.

The matrix element method calculates the optimal kinematic observable to discriminate signal from background, which corresponds to choosing the optimal function $w(\Phi)$ that maximizes $S_{\text{eff}}/\delta B_{\text{eff}}$. As derived in App. A.4, the ideal weighting function is

$$w_{\text{best}}(\Phi) = \frac{S(\Phi)}{B(\Phi)}, \tag{2.15}$$

which yields

$$\left[\frac{S_{\text{eff}}}{\delta B_{\text{eff}}}\right]_{\text{best}} = \sqrt{\int \mathrm{d}\Phi\, \frac{S(\Phi)^2}{B(\Phi)}}. \tag{2.16}$$

We can therefore recalculate the reach for the X boson using this ideal value for $S_{\text{eff}}/\delta B_{\text{eff}}$, and the results are shown in Fig. 2.9. As advertised, there is potential factor of 3 improvement in the reach by using the full kinematic information in the signal and background distributions.

Of course, the matrix element method assumes that the $w_{\text{best}}(\Phi)$ function is calculated using the true signal and background distributions, and this is not possible in practice, due to both theoretical uncertainties in the matrix elements and detector effects. Still, one might still hope to improve the reach by doing hard kinematic cuts that approximate $w_{\text{best}}(\Phi)$. As

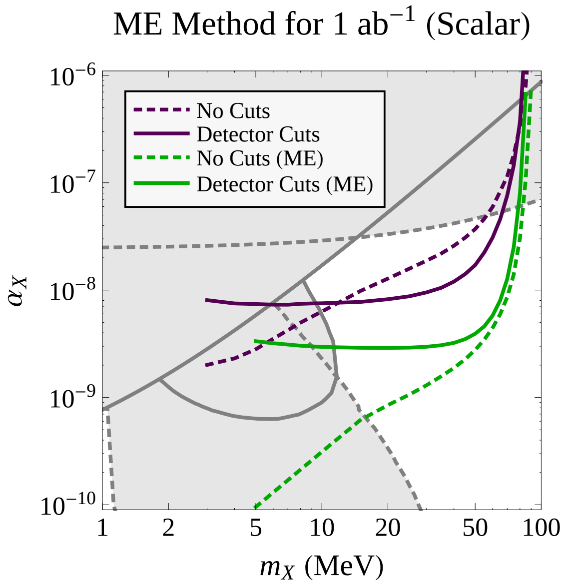

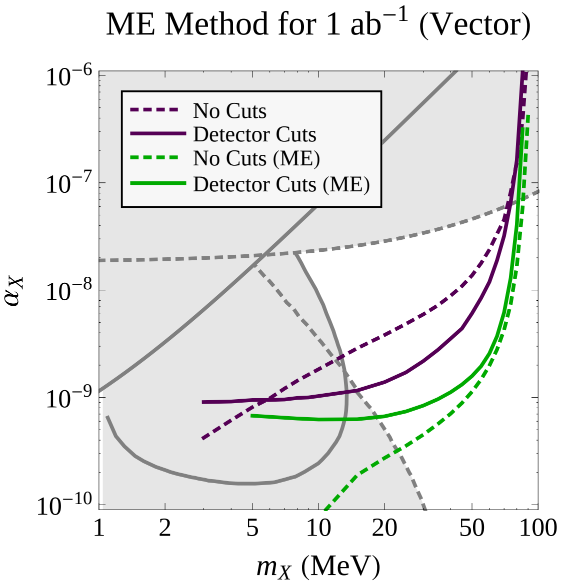

Figure 2.9: Reach plots using the matrix element method. The solid curves include the detector acceptance cuts $-2 < \eta < 2$, KE$_p > 0.5$ MeV, and KE$_{e^\pm} > 5$ MeV, while the dashed lines have no acceptance cuts. The green curves indicate the reach with the matrix element method, and the purple curves without. In all cases, we take an integrated luminosity of 1 ab^{-1}, and the reach corresponds to $S/\sqrt{B} = 5$ assuming $m_{e^+e^-}$ resolution of 1 MeV. The matrix element method can yield around a factor of 3 improvement in the reach. Note also that the detector geometry alone does act like a primitive matrix element method by cutting out the forward region.

an example of this, consider Fig. 2.9. There one sees noticeable improvement in $S/\sqrt{B}$ just from applying the fiducial detector geometry. In this way, the detector geometry does act like a primitive $w(\Phi)$. In Sec. 2.6, we will look at $w_{\text{best}}(\Phi)$ in more detail to see what other kinds of hard cuts could be most helpful in teasing out the signal. In principle, by using a polarized electron beam, one could obtain additional information from the full $ep \to ep + X$ matrix element, but we will not consider polarized beams in this chapter.

2.5 Comparison to Other Searches

We argued that low energy ep scattering with at least 1 ab^{-1} of data was a promising venue for looking for a light, weakly coupled X boson. Unlike beam dump experiments where the proton recoil spectrum is not measurable, a high intensity electron beam on a diffuse gas target allows for full event reconstruction.

However, ep scattering is certainly not the unique choice of experiment with full reconstruction potential, and electron-electron scattering or electron-position scattering also have large X boson production rates. Here, we will argue that for the same integrated luminosity,

ep, e^-e^-, and e^+e^- colliders all offer comparable search power. But given the very high instantaneous luminosity achievable at the JLab FEL, we believe that ep scattering is favored for X bosons in the range 10 MeV – 100 MeV.

Consider the following four scattering processes:

$$\begin{aligned} e^-p &\to e^-p + X \quad \text{(fixed target)}, \\ e^-e^- &\to e^-e^- + X \quad \text{(colliding beams)}, \\ e^+e^- &\to e^+e^- + X \quad \text{(colliding beams)}, \\ e^+e^- &\to \gamma + X \quad \text{(colliding beams)}. \end{aligned} \tag{2.17}$$

The first one is the ep scattering experiment in this chapter, the next two are the equivalent processes for e^-e^- and e^+e^- colliders, and the final search channel is only available for e^+e^-. The distinction between "fixed target" and "colliding beams" is only needed to determine the relation between the lab frame and the center-of-mass frame of the experiment. We assume the same detector technology for all four experiments, with pseudorapidity coverage in the lab frame of $-2 < \eta < 2$, the kinetic energy restriction from Eq. (2.11), and 1 MeV invariant mass resolution. For the $e^+e^- \to \gamma + X$ search, one would also need to impose a cutoff on photon energy, but as the photons are monochromatic for a given beam energy, this would merely correspond to no reach at all once the cutoff is reached and is thus not shown.

In Fig. 2.10, we show the reach in α_X as a function of the available beam energy

$$E_{\text{eff}} = \sqrt{s} - m_1 - m_2, \tag{2.18}$$

where $\sqrt{s}$ is the center-of-mass energy of the collider and m_i are the beam masses. (For ep scattering with a 100 MeV electron beam, $E_{\text{eff}} \simeq 95$ MeV.) We take a fixed $m_X = 50$ MeV and fixed integrated luminosity $\mathcal{L} = 1\ \text{ab}^{-1}$. The signal and background cross sections were calculated using the same method as in Sec. 2.4.

Given the same integrated luminosity and high enough values of E_{eff}, the reach for the searches involving four final state fermions are within a factor of 2 of each other. However, getting 1 ab^{-1} of data in the proposed FEL experiment requires only 1 month of data taking, while the maximal luminosity currently achieved in colliding beam experiments is $1.7 \cdot 10^{34}\ \text{cm}^{-2}\ \text{s}^{-1} \simeq 0.5\ \text{ab}^{-1}/\text{yr}$. Since high luminosity is critical to probe the parameter space of interest, this favors a fixed target experiment for the four fermion final states. For the same luminosity, the $e^+e^- \to \gamma + X$ search is 1 to 2 orders of magnitude more sensitive than the ep search, and we will comment more on this search below.

It should be noted that existing collider experiments, such as BaBar and Belle, already have data sets with integrated luminosities of $\sim 1\ \text{ab}^{-1}$. However, the collisions there occur at much higher energies. At those energies and for the same search strategy, many additional backgrounds, both reducible and irreducible, are present, increasing the difficulty of the analysis. In fact, studies of these detectors typically focus on the case with $m_X > 2m_\mu$, as the decay of the X boson to muons is more easily reconstructed than the decay to electrons [46, 60].

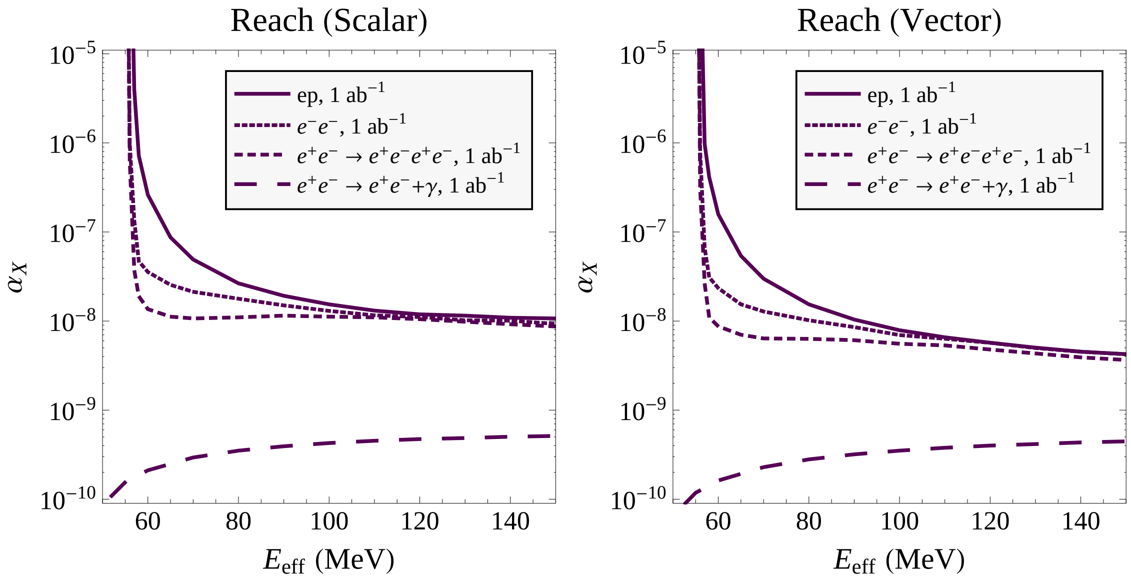

Figure 2.10: Reach for an 50 MeV X boson, varying $E_{\text{eff}} = \sqrt{s} - m_1 - m_2$. We compare the present *ep* scattering proposal with three alternative searches: $e^-e^- \to e^-e^- + X$, $e^+e^- \to e^+e^- + X$, and $e^+e^- \to \gamma + X$. In all cases, we assume a detector acceptance of $-2 < \eta < 2$, $\text{KE}_p > 0.5$ MeV, and $\text{KE}_{e^\pm} > 5$ MeV. While the in principle reach in $e^+e^- \to \gamma + X$ appears to be better than the other three, we discuss the challenges of that search in the text. For the same integrated luminosity and large enough E_{eff}, the three searches with four outgoing fermions have comparable reach, which favors the *ep* scattering proposal where high luminosity is more readily achievable.

On the other hand, even at the higher energies of existing data sets, the $e^+e^- \to \gamma + X$ channel does look quite promising for an X boson search due to the lack of hadronic backgrounds. That said, two factors lead this channel to be more complimentary than competitive with the search we propose. Our naive estimate of the $\gamma + X$ reach assumed perfect reconstruction of every event meeting the detector geometry cuts. This is significantly more difficult with a search using on-shell photons as there is no longer tracking information for every particle. In order to identify the single energetic photon in the event with high accuracy, it is necessary to put tighter cuts on the photon angle to get farther away from the beam pipe. Estimates in Ref. [44] indicate that when such cuts are put in place, the reach in coupling actually becomes comparable to that of the *ep* search. Additionally, the search for $\gamma + X$ is complicated by photon conversion in the tracking volume from the much larger $e^+e^- \to \gamma\gamma$ process. While this can be offset by cutting on displaced vertices, such an approach becomes difficult for e^+e^- mass bins below 50 MeV, and impossible in mass bins below 20 MeV [72]. For X bosons above 50 MeV, one should be able to extend the $\gamma + X$ search already done for $X \to \mu^+\mu^-$ [61] to $X \to e^+e^-$, making the search complementary to *ep* scattering by filling in the mass range between ~ 50 MeV and $2m_\mu$.

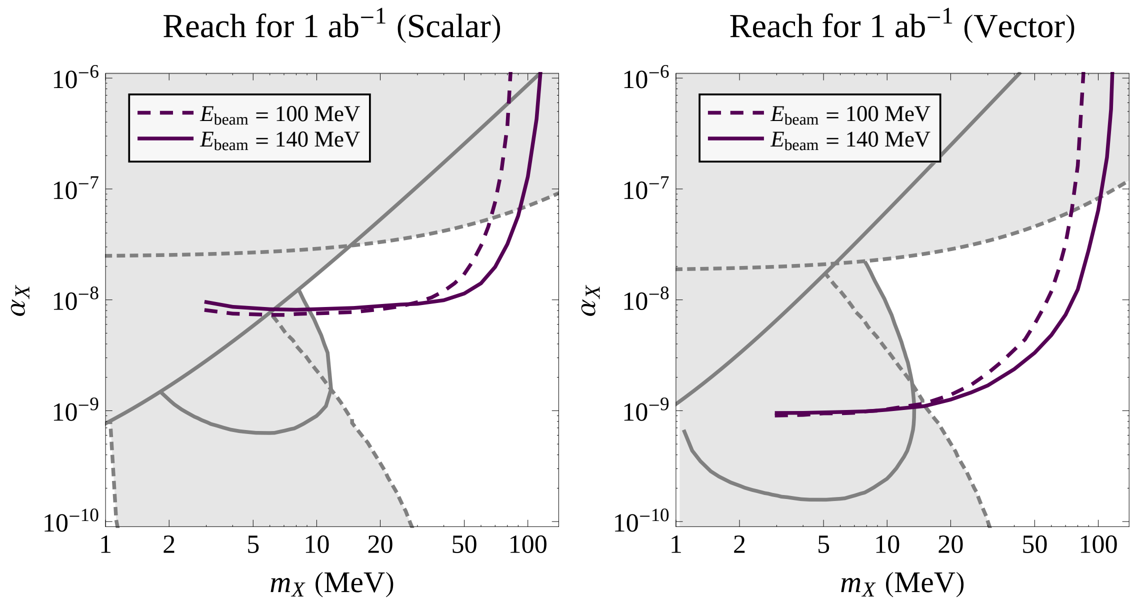

Figure 2.11: Reach plots for *ep* collisions, increasing the electron beam energy from $E_e =$ 100 MeV to $E_e = 140$ MeV, the maximal sustainable beam energy available at the JLab FEL. Assumptions about detector geometry, integrated luminosity, and energy resolution are the same as the previous figures.

The preceding discussion of the benefits of *ep* scattering applies for X bosons in the mass range 10 MeV $< m_X <$ 100 MeV. For higher values of m_X, the JLab FEL simply does not have the kinematic reach achievable in other colliders. The maximum sustainable FEL beam energy is around 140 MeV [55], limiting the in-principle reach to $m_X \lesssim 131$ MeV. Moreover, even if one were able to get higher energy electron beams, it is no longer clear whether *ep* scattering would pose any advantage, since for electron beam energies above the pion mass, inelastic scattering channels open up, increasing the number of tracks per beam crossing.

Below the pion mass threshold, though, the reach in *ep* collisions can be improved in going to somewhat higher E_{eff} as seen in Fig. 2.10. A more detailed look is shown in Fig. 2.11, which compares the reach for $E_e = 100$ MeV to the maximum sustainable FEL energy of $E_e = 140$ MeV. For X boson masses close to the kinematic limit, the higher energy electron beam gives improved sensitivity, though at low masses, most of which have already been ruled out by beam dump constraints, the reach gets slightly worse.

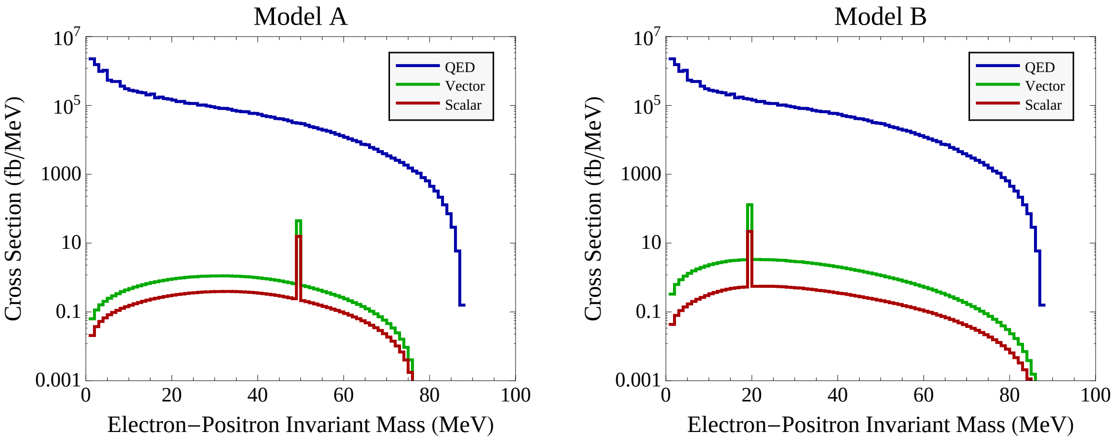

Figure 2.12: Invariant mass distribution for $m_{e^+e^-}$, comparing the QED background to benchmark models A (left) and B (right). The fluctuations in the background distribution at low $m_{e^+e^-}$ are from Monte Carlo statistics, and are not indicative of expected statistical fluctuations. The signal includes the combinatoric background from pairing the "wrong" electron with the positron. These plots include the detector acceptance criteria $-2 < \eta < 2$, $\mathrm{KE}_p > 0.5$ MeV, and $\mathrm{KE}_{e^\pm} > 5$ MeV. Note the four orders of magnitude difference between the expected signal and background.

2.6 Benchmark Studies

In this section, we consider two benchmark X boson scenarios, indicated on Fig. 2.1,

$$\mathrm{A}: \qquad m_X = 50\ \mathrm{MeV} \qquad \alpha_X = 10^{-8}, \tag{2.19}$$

$$\mathrm{B}: \qquad m_X = 20\ \mathrm{MeV} \qquad \alpha_X = 3 \cdot 10^{-9}, \tag{2.20}$$

with both scalar and vector couplings in each case. These points were chosen to be roughly close to the 1 ab^{-1} reach lines in Fig. 2.1. We will show an example analysis strategy for X boson signal extraction and then show various kinematic distributions to highlight which parts of phase space are most sensitive to X boson production.

To begin, consider reconstruction of the X boson resonance. In Fig. 2.12, we show the invariant mass distribution for e^+e^- pairs, taking the fiducial detector acceptance from Eqs. (2.10) and (2.11). Since the final state electrons are indistinguishable, the plot includes two histogram entries per event. In the case of the signal distribution, there is the expected spike at m_X accompanied by a combinatoric background from pairing the positron with the "wrong" electron. We see that there is a four orders of magnitude difference between signal and background, consistent with Fig. 2.7 which did not include any detector acceptance effects.

To show how the X boson resonance could be seen despite the large background, Fig. 2.13 shows a simulated distribution of $m_{e^+e^-}$ created as follows. First, we generate 1 ab^{-1} of background pseudo-data for the $m_{e^+e^-}$ distribution and add it to 1 ab^{-1} of signal pseudo-

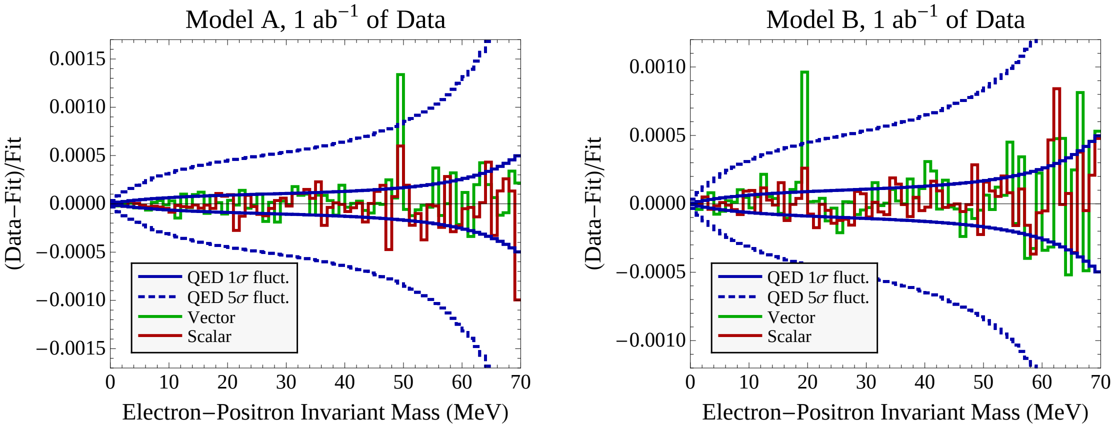

Figure 2.13: Simulated $m_{e^+e^-}$ distributions compared to a background fit. This plot was made with 1 ab^{-1} of signal and background pseudo-data, assuming 1 MeV invariant mass resolution. The blue curves show the expected statistical uncertainties in the background, 1σ (solid) and 5σ (dashed). For the vector couplings (green), both model A (left) and B (right) show a prominent bump in the dilepton invariant mass distribution, which is expected since these benchmark points lie above the 1 ab^{-1} reach line. For the scalar couplings (red), a bump cannot be seen, since these benchmark points lie below the 1 ab^{-1} reach line.

data. We take the combined signal plus background distribution, and fit it to an ad hoc functional form:

$$\frac{\mathrm{d}\sigma_{\text{fit}}}{\mathrm{d}m} = N(m)^a(m_{\max} - m)^b(e^m)^c, \tag{2.21}$$

where N, a, b, and c are fit coefficients, and $m_{\max}$ is the maximum kinematically allowed value for $m_{e^+e^-}$. We then plot the fractional difference between the pseudo-data and the final fit function in Fig. 2.13. For the case of the vector couplings where the benchmark points lie above the 1 ab^{-1} reach line, a peak at the $m_{e^+e^-}$ distribution at m_X is indeed visible above the expected statistical fluctuations in the background, showing that a sideband procedure for extracting the background is feasible. For the scalar benchmarks, no such peak is visible, as expected since these benchmarks lie below the 1 ab^{-1} reach line.

The X boson resonance signal could be further enhanced by using the matrix element method of Sec. 2.4.3, which would be applied at each value of $m_{e^+e^-}$. To see how the matrix element method would affect our two benchmark points, we plot some example kinematic distributions in Figs. 2.14, 2.15, 2.16, and 2.17. Except as indicated, these plots are made using the fiducial detector geometry cuts of $-2 < \eta < 2$, $\text{KE}_p > 0.5$ MeV, and $\text{KE}_{e^\pm} > 5$ MeV, and require that at least one electron/positron pair reconstructs m_X. The electron that reconstructs the candidate resonance is the active electron, and the other is the spectator electron. In addition to the raw background and signal cross sections, we also plot the ideal weighting function from Eq. (2.15).[9] Large values of the weighting function correspond to

---

[9] As a sanity check, we verified that the weighting function is approximately equal to the ratio of the

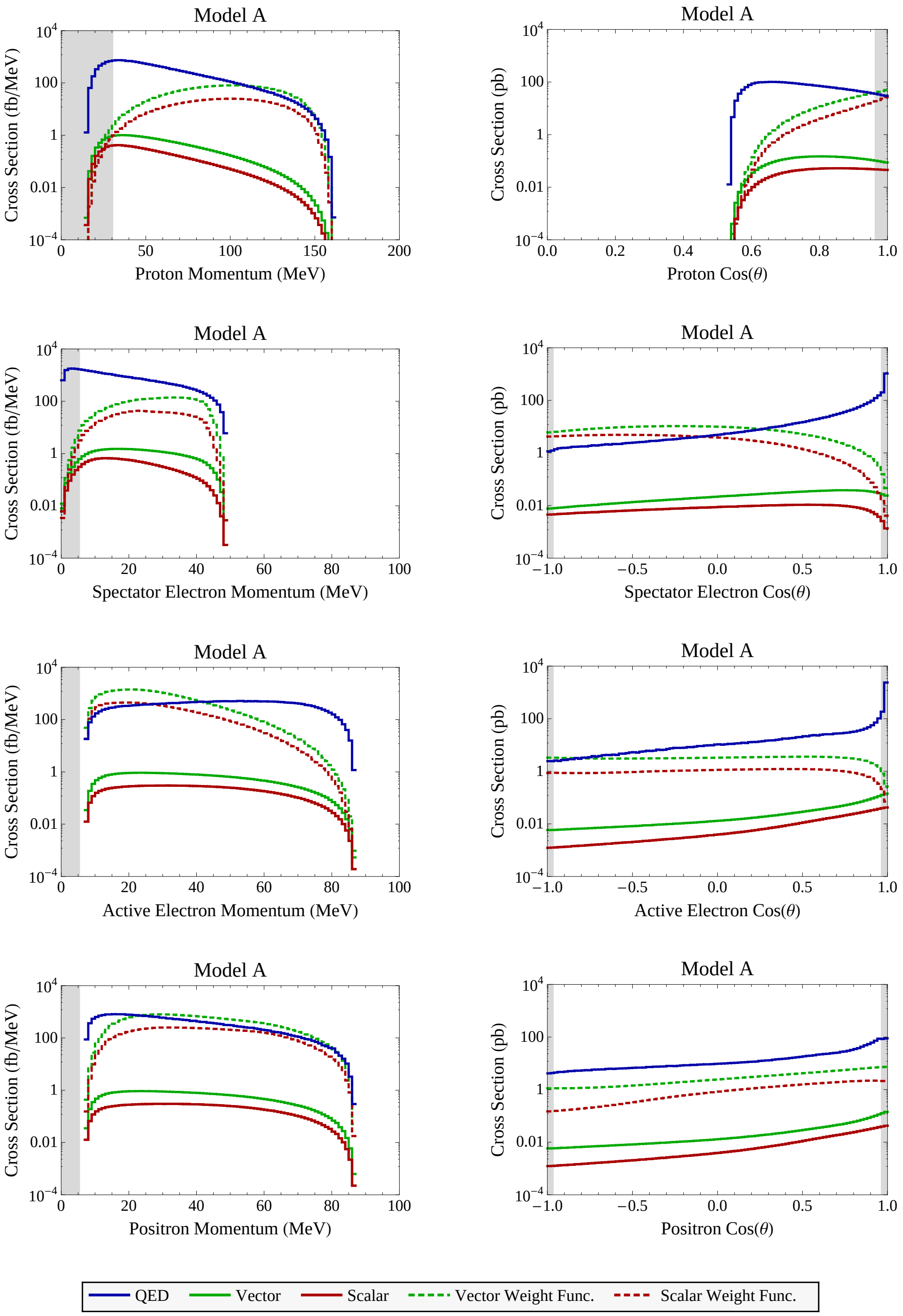

Figure 2.14: Momentum and angular distributions for model A, with $m_X = 50$ MeV and $\alpha_X = 10^{-8}$. The QED background is restricted to have one e^+e^- pair reconstruct m_X, and the corresponding electron is called the active electron while the other is the spectator electron. These plots include detector acceptance cuts, but the cut corresponding to the plotted distribution is indicated by shading. The solid blue curves are the QED background, and the solid red (green) curves are the scalar (vector) signal. The dashed red (green) curves are the ideal weighting functions for the scalar (vector) case with arbitrary normalization, which are large in the region of phase space most sensitive to X boson production.

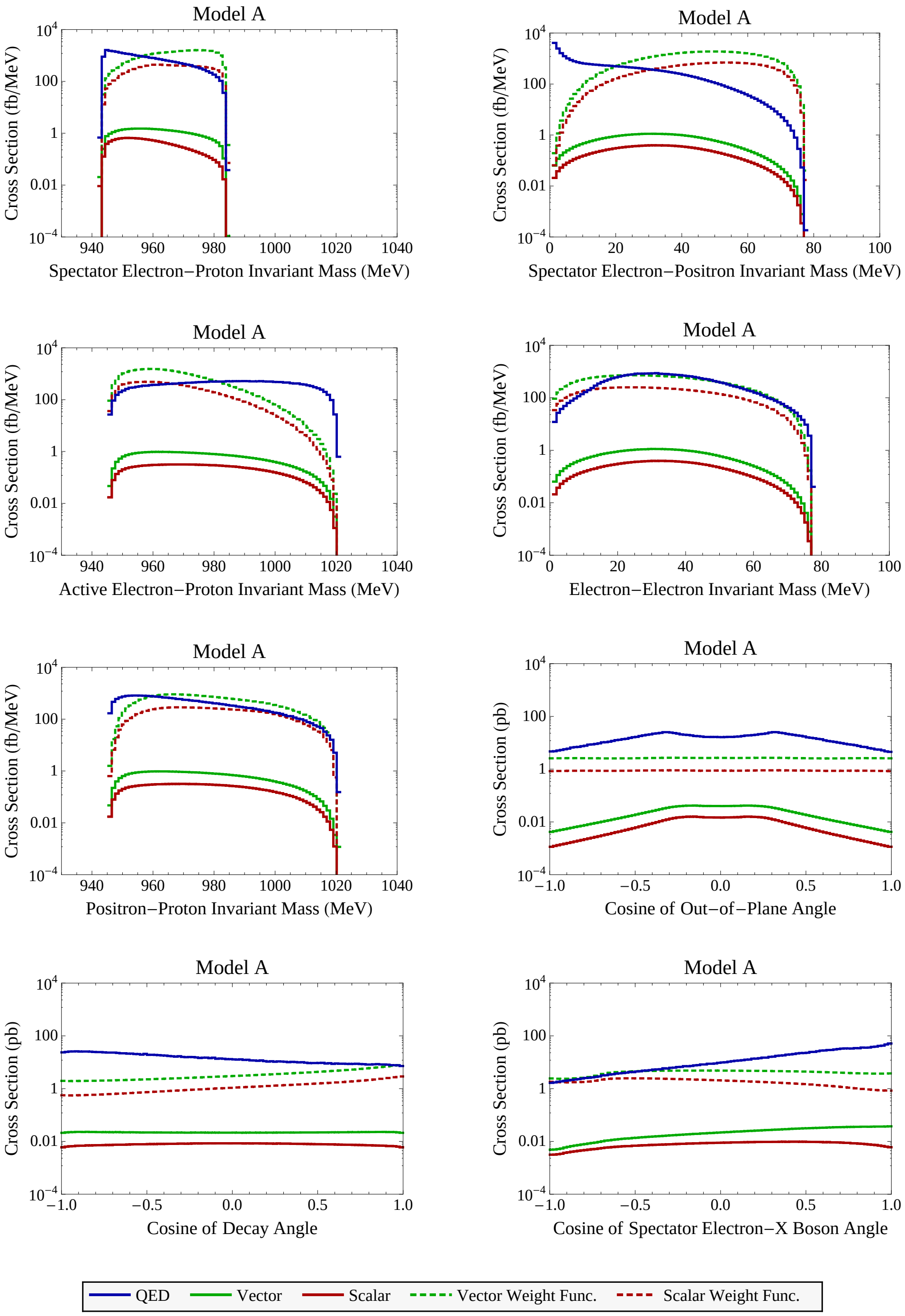

Figure 2.15: Additional kinematic distributions for model A, with the same criteria and labeling as Fig. 2.14. Shown are five pairwise invariant mass distributions (the active electron-positron invariant mass would of course just give a peak at m_X). The out-of-plane angle is the between the reconstructed X boson and the incoming electron/spectator electron plane. The decay angle is the angle of the X boson decay products relative to the X boson momentum, measured in the X rest frame. Also shown is the angle between the spectator electron and the reconstructed X boson.

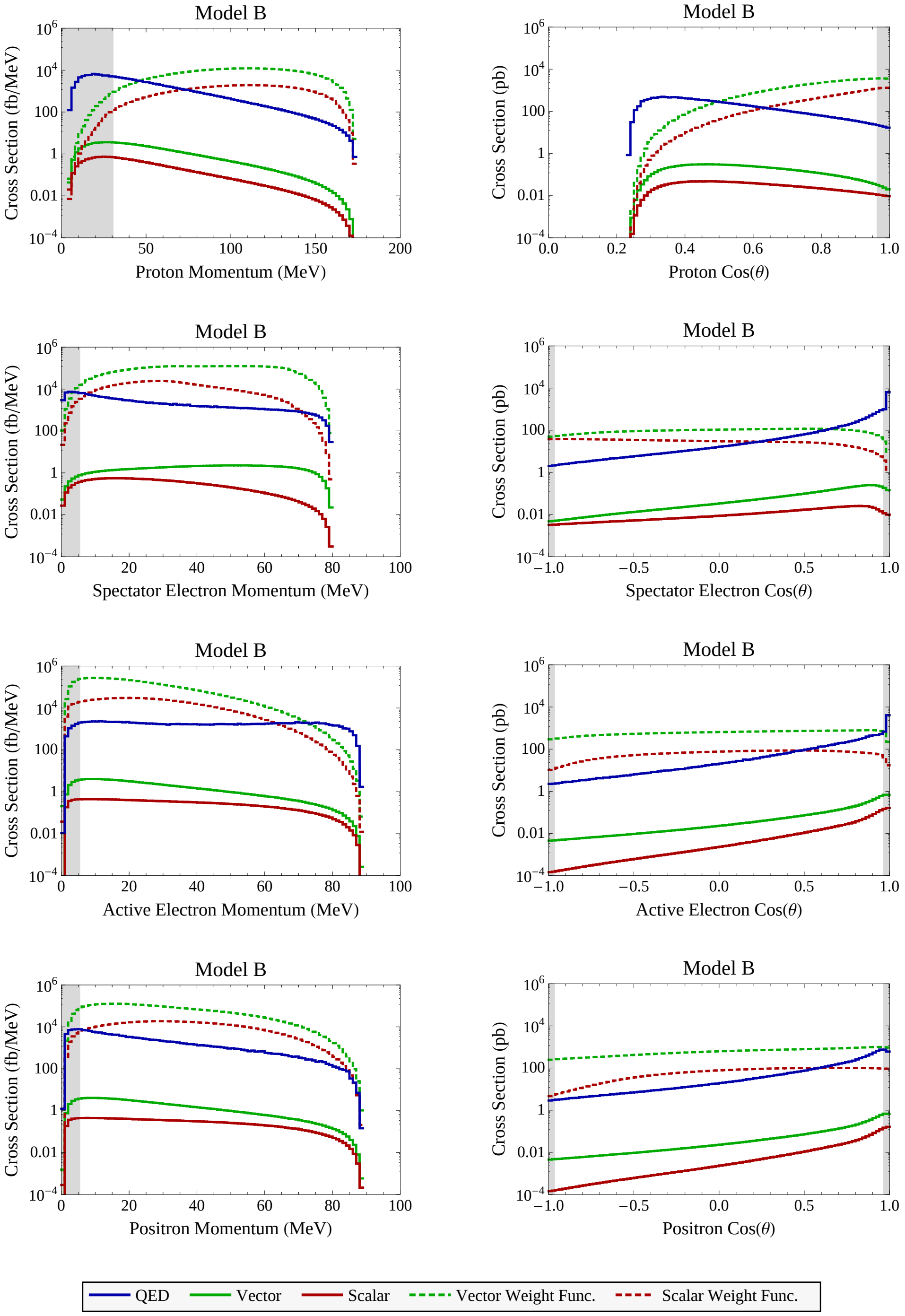

Figure 2.16: Momentum and angular distributions for model B, with $m_X = 20$ MeV and $\alpha_X = 3 \cdot 10^{-9}$, analogous to Fig. 2.14.

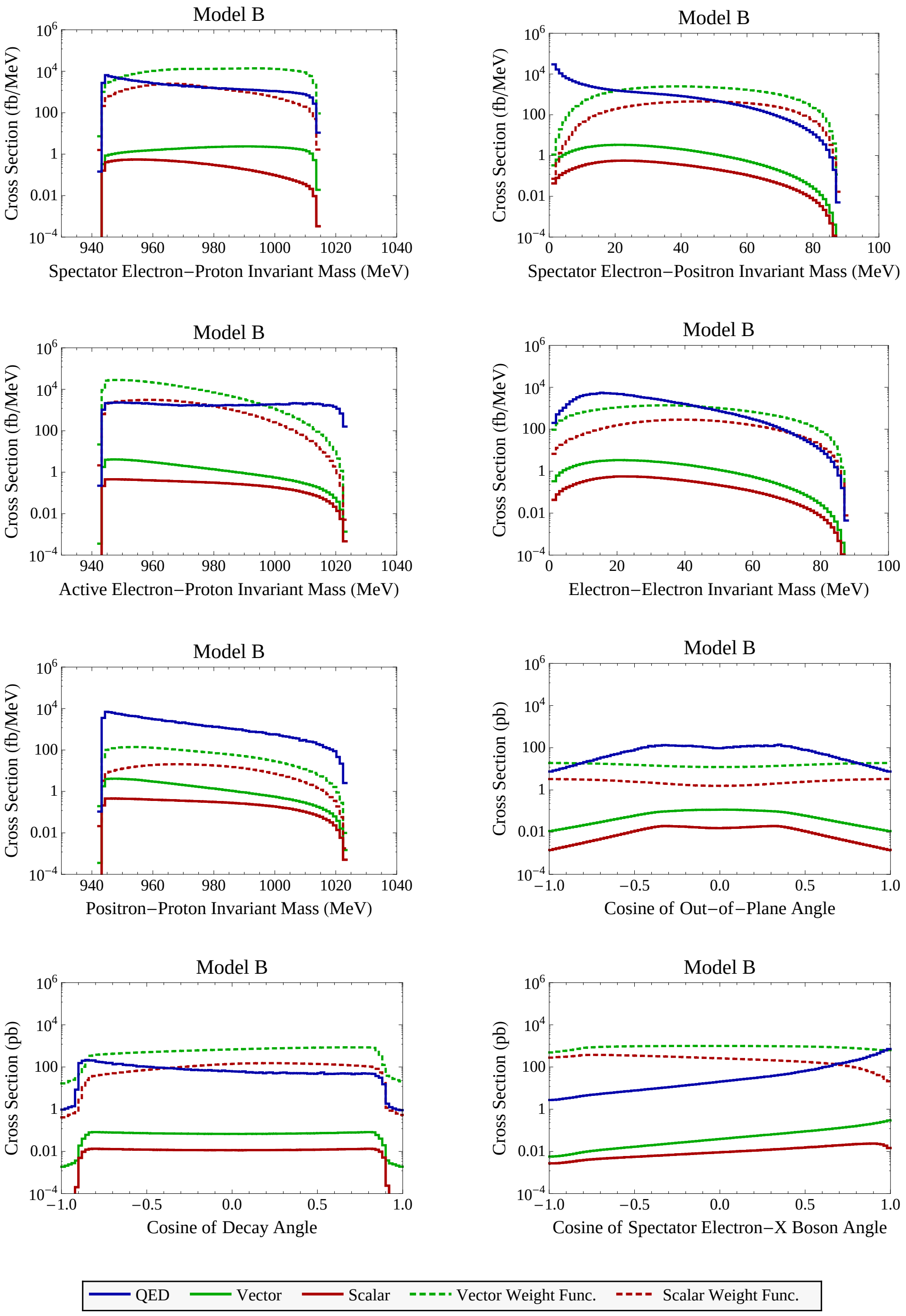

Figure 2.17: Additional kinematic distributions for model B, analogous to Fig. 2.15.

regions of phase space that have the highest sensitivity to the X boson.

In Figs. 2.14 and 2.16, we show the momentum and angular distributions for the four outgoing fermions. All of the detector geometry cuts are imposed, except that the cut corresponding to the plotted distribution is indicated via shading.

From the momentum distributions, we see that the kinetic energy cuts from Eq. (2.11) do not cut out much of the most sensitive region, and indeed the cut on proton and spectator electron kinetic energy enhances the signal relative to the background. For the angular distributions, because the background has a strong peak when an electron scatters in the forward direction, the weighting function is suppressed near $\cos(\theta_{\text{electron}}) = 1$. This explains why in Fig. 2.8, the reach did not improve much in going from an $|\eta| < 2$ cut to an $|\eta| < 3$ cut. Away from this peak, the weighting function has roughly flat sensitivity to the electron/positron angle, indicating that large angular acceptance is important for X boson reconstruction. Because of energy-momentum conservation, the proton can only scatter in the forward direction, and the most sensitive region is in fact in the most forward region.

In Figs. 2.15 and 2.17, we show the pair-wise invariant mass distributions, as well as three angular distributions. The out-of-plane angle is the angle the reconstructed X boson moves relative to the plane defined by the incoming electron beam and the spectator electron. The decay angle is the angle between the X boson momentum and the outgoing positron momentum, as measured in the X boson rest frame. Also plotted is the angle between the spectator electron and the reconstructed X boson.

The invariant mass distributions do show some ability to distinguish signal from background. Especially promising is the invariant mass between the spectator electron and the positron, which peaks at small values for the background. The angular distributions show less promise, as the ideal weighting functions are relatively flat. Note that the weighting function for the scalar and vector cases do have different shapes in the angular distributions, which explains why the reach plots in Sec. 2.4 have different m_X dependence even after correcting for the total signal cross section.

Once the X boson is discovered, the decay angle could be useful for distinguishing the scalar coupling from the vector case. This distribution is flat for the scalar signal, but encodes non-trivial angular information in the vector case. This angular variation is much smaller than the background, though, so a careful analysis would be necessary to extract the nature of the X boson coupling.

2.7 Prospects for Displaced Vertices

We saw in Sec. 2.3.2 that there is a region of parameter space where the X boson has not yet been ruled out by the beam dump experiments but has a lifetime long enough to leave a displaced vertex in *ep* collisions. While the X bosons produced in low energy *ep* collisions are generically not very boosted, there is enough of a tail in the lifetime distribution that a

---

signal and background in a given observable bin, appropriately normalized to the phase space volume of that bin. See App. A.4.

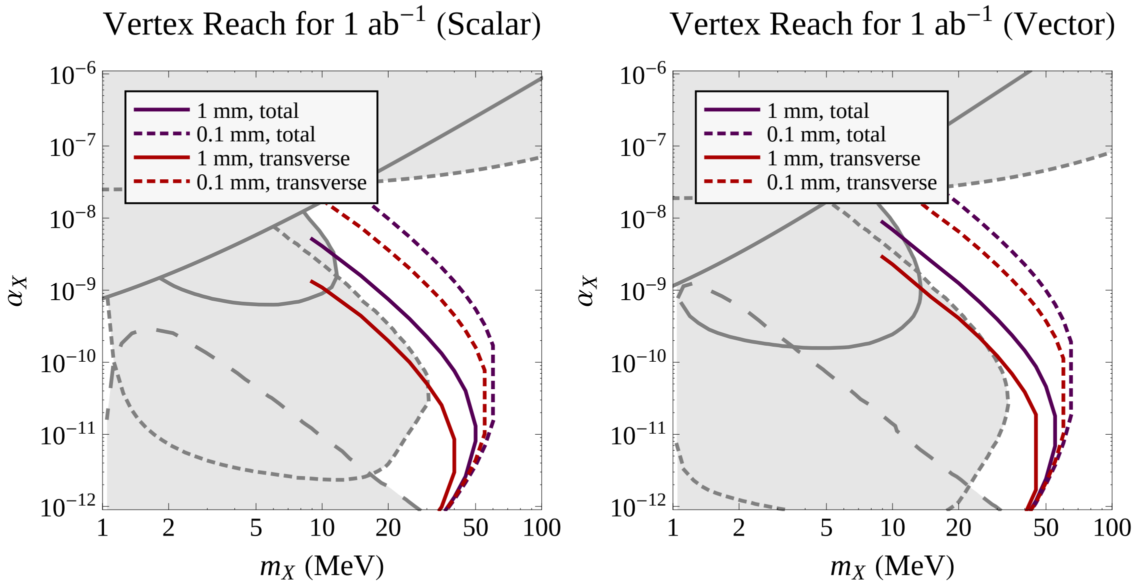

Figure 2.18: Reach in *ep* scattering using a displaced vertex search strategy. The curves correspond to producing 10 signal events with an integrated luminosity of 1 ab^{-1}. The purple curves assume that the total displacement between the interaction vertex and the X boson decay vertex can be measured. The red curves assume that only the transverse displacement from the beam axis can be measured. Note that the plotted range for α_X differs from the previous reach plots in this chapter, and that an additional bound from the E137 experiment is shown.

few X bosons will have large displacements. Moreover, with a diffuse gas target, one can in principle probe smaller vertex displacements than in a solid target.

Since the QED background does not generically lead to displaced vertices, this suggests that the reach could be extended beyond that presented in Sec. 2.4. Of course, there are instrumental effects that can lead to fake displacement, but we ignore these in this study. For the signal, the displacement can be straightforwardly calculated by convolving the X boson momentum spectrum with the exponentially falling lifetime curve, properly taking into account boost factors.

With no expected irreducible backgrounds, we estimate the naive reach by considering the region of parameter space where at least 10 displaced vertices would be observed. The expected reach using two different search strategies is presented in Fig. 2.18. The more aggressive strategy attempts to reconstruct the total displacement of the X boson. That is, the detected recoiling proton and spectator electron define the interaction vertex, and electron-positron pair from the X boson define the decay vertex. We plot the reach assuming a 1 mm or 0.1 mm total displacement could be observed. Since there can be multiple scatterings per beam crossing, this method faces a background from uncorrelated scattering events.

An alternative strategy is to merely reconstruct the transverse displacement of the decay vertex from the beam axis. Since the X boson momentum is peaked in the forward direction, this noticeably reduces the reach at the same displacement resolution. Assuming transverse vertex displacement is easier to detect than total displacement, one might imagine that increased resolution might compensate to make this the preferred strategy. Note that the transverse displacement search faces a possible background from photon conversion within the gas target.

Both displaced vertex strategies probe a different part of the parameter space from the search in Sec. 2.4, and therefore can be viewed as complementary to the QED background-limited analysis. In particular, X bosons with couplings two order of magnitude smaller than those accessible with a direct bump hunt could be seen. At such small couplings, other prior beam dump experiments come into play beyond those discussed earlier in Sec. 2.3.2. In Fig. 2.18, the beam dump constraint at the lowest couplings comes from the E137 experiment at SLAC [73], calculated analogously to the constraints in Sec. 2.3.2.

2.8 Conclusions

Low energy electron-proton scattering is one of the basic processes in the standard model. It is therefore intriguing that new physics might be discovered in a regime that is thought to be dominated by elastic and quasi-elastic QED processes. Recent astrophysical anomalies have motivated a new paradigm for dark matter, where heavy dark matter interacts with a light, weakly coupled boson. New low energy, high intensity scattering experiments are an ideal setting to constrain (or confirm) this exciting scenario.

We have argued an X boson with $\alpha_X \sim 10^{-8}$ and 10 MeV $< m_X <$ 100 MeV could be discovered in low energy ep scattering with around 1 ab^{-1} of data assuming 1 MeV invariant mass resolution. Since the search for $X \to e^+e^-$ is background limited, it is crucial to have an experiment with good energy resolution and very high statistics. We believe that the unique combination of high luminosity with full event reconstruction makes this a compelling experimental proposal for the JLab FEL. This proposal is complementary to the beam dump experiments envisioned in Refs. [43, 50], which are better suited for smaller value of α_X and larger values of m_X.

We have shown that a matrix element method which uses complete kinematic information about the signal and background can increase the sensitivity to the X boson by about a factor of 3. Though not studied in this chapter, a polarized electron beam could be useful in extracting additional matrix element information. Of course, the most straightforward way to increase the sensitivity of the experiment is to improve the invariant mass resolution beyond our fiducial value of 1 MeV. Finally, if reconstruction of 1 mm or 0.1 mm displaced vertices are possible, then ep scattering could probe an interesting region of X boson parameter space with smaller couplings.

Chapter 3

Constraining the Axion Portal[1] with $B \to K\ell^+\ell^-$

3.1 Introduction

Motivated by a variety of cosmic ray anomalies [21, 22, 23, 24], a new dark matter paradigm has emerged where TeV-scale dark matter interacts with GeV-scale bosons [27, 28, 29]. In one such scenario—dubbed the "axion portal" [30]—dark matter in the Milky Way halo annihilates into light pseudoscalar axions-like states. In order to explain the observed galactic electron/positron excess, the axion, a, is predicted to have a specific mass and decay constant [30]

$$360 < m_a \lesssim 800 \text{ MeV}, \qquad f_a \sim 1 - 3 \text{ TeV}. \tag{3.1}$$

These axions couple to standard model fermions proportional to their Yukawa couplings, and in this mass range the axion dominantly decays as $a \to \mu^+\mu^-$. Other novel dark matter scenarios involving axion-like states have also been proposed [75, 76, 77, 78, 79], which allow for broader range of axion masses and decay constants.

More generally, light axion-like states appear in variety of new physics scenarios, as they are the ubiquitous prediction of spontaneous Peccei-Quinn (PQ) [80] symmetry breaking. The most famous example is the Weinberg-Wilczek axion invoked to solve the strong CP problem [81, 82], as well as invisible axion variants [83, 84, 85, 86]. Light pseudoscalar particles appear in any Higgs sector with an approximate PQ symmetry, which often occurs in the minimal or next-to-minimal supersymmetric standard models (MSSM and NMSSM). Models of dynamical supersymmetry breaking typically predict an R-axion [87], whose couplings can mimic PQ-type axions. There has also been speculation [88] that the HyperCP anomaly [89] might be explained by a light axion. Therefore, searches for light axion-like states have the potential to confirm or exclude a variety of new physics models.

In this chapter, we show that flavor-changing neutral current $b \to s$ decays place stringent bounds on such models. While the coupling of the axion to fermions is flavor-diagonal,

---

[1] This chapter, as well as App. B, was co-written with Zoltan Ligeti and Jesse Thaler and published in [74].

the $b \to sa$ decay mediated by a top-W penguin diagram is enhanced by the top Yukawa coupling appearing in the top-axion vertex. To our knowledge, Refs. [90, 91, 92] were the first to consider this decay as a search channel for light pseudoscalars, where the a field was identified with the CP-odd Higgs A^0 in a two Higgs doublet model (2HDM). The analysis of this chapter highlights the potential off this search channel for models like the axion portal, where there is an a field which mixes with A^0.

In the parameter range of interest for the axion portal, the axion decays promptly to $\mu^+\mu^-$, and we find that existing $B \to K\ell^+\ell^-$ data (for $\ell = e, \mu$) can be used to derive multi-TeV constraints on the axion decay constant f_a, especially for small values of $\tan\beta$. For heavier axion-like states with reduced branching fractions to muons, $B \to K\ell^+\ell^-$ can still be used to place a bound, relevant for constraining light Higgs scenarios in the NMSSM [93, 94, 95]. The estimates in this chapter are likely improvable by dedicated $B \to Ka$ searches at BaBar and Belle, and can be further strengthened at LHCb and a possible super B-factory. These searches are complementary to $\Upsilon(nS) \to \gamma a$ searches recently performed by BaBar [96].

In the next section, we review the axion portal Lagrangian, which is relevant for any DFSZ-type (Dine-Fischler-Srednicki-Zhitnitsky) axion [83, 84], and use it to calculate the effective $b \to sa$ vertex in Sec. 3.3. We sketch the current experimental situation in Sec. 3.4 and derive corresponding bounds in Sec. 3.5. We conclude in Sec. 3.6.

3.2 Review of the Axion Portal

If one were only interested in studying the tree-level interactions of new axion-like states, it would be sufficient to introduce a new term in the Lagrangian of the form

$$\delta\mathcal{L}_{\text{int}} = \frac{c_\psi}{f_a}\,\overline{\psi}\gamma_\mu\gamma_5\psi\,\partial_\mu a\,, \tag{3.2}$$

where f_a is the axion decay constant and c_ψ is the fermion charge under the broken $U(1)$. By the equations of motion, such a coupling is proportional to the fermion mass parameter, leading to an effective coupling constant $c_\psi m_\psi/f_a$. However, the $b \to sa$ process we are interested in occurs via a top-W penguin loop. With only Eq. (3.2), such a diagram is logarithmically sensitive to the cutoff scale [90], so it is necessary to embed the axion coupling in a complete theory to get a reliable bound on f_a.

The axion portal [30] is an example of a class of theories where the $b \to sa$ amplitude is finite. The axion arises from spontaneous PQ-symmetry breaking in a 2HDM, of which the DFSZ axion is a special case. We show that the $b \to sa$ amplitude can be derived from the $b \to sA^0$ amplitude, where A^0 is the CP-odd Higgs boson in a PQ-symmetric 2HDM.

Consider a complex scalar field S carrying $U(1)_{\text{PQ}}$ charge that gets a vacuum expectation value $\langle S\rangle \equiv f_a$. This spontaneous symmetry breaking leads to a light axion-like state, a,

$$S = f_a \exp\left[\frac{i}{\sqrt{2}f_a}\,a\right]. \tag{3.3}$$

The assumption in the axion portal (and for any DFSZ-type axion) is that the only operator that transmits PQ charge from S to the standard model is

$$\delta\mathcal{L} = \lambda\, S^n h_u h_d + \text{h.c.}, \tag{3.4}$$

where λ is a (possibly dimensionful) parameter, and n is an integer. This coupling forces $h_u h_d$ to carry non-trivial PQ charge, and we assume that the entire Higgs potential preserves the $U(1)_{\text{PQ}}$ symmetry to a good approximation. The DFSZ axion [83, 84] corresponds to the case with $n = 2$, while for the PQ-symmetric NMSSM [97] $n = 1$. Either case can be used in the axion portal model of dark matter.

Since the vevs of S, h_u, and h_d all break the PQ symmetry, the physical axion will be a linear combination of the phases of all three fields.[2] However, in the $f_a \gg v_{\text{EW}}$ limit, it is calculationally more convenient to work in an "interaction eigenstate" basis, where the axion a only appears in S, and the CP-odd Higgs A^0 only appears in the two Higgs doublets in the form:

$$\begin{aligned} h_u &= \begin{pmatrix} v_u \exp\left[\dfrac{i\cot\beta}{\sqrt{2}v_{\text{EW}}}\,A^0\right] \\ 0 \end{pmatrix}, \\ h_d &= \begin{pmatrix} 0 \\ v_d \exp\left[\dfrac{i\tan\beta}{\sqrt{2}v_{\text{EW}}}\,A^0\right] \end{pmatrix}, \end{aligned} \tag{3.5}$$

where $\tan\beta \equiv v_u/v_d$,

$$v_{\text{EW}} \equiv \sqrt{v_u^2 + v_d^2} \equiv \frac{m_W}{g} \simeq 174\ \text{GeV}\,, \tag{3.6}$$

and we have omitted the charged Higgs $H^\pm$ and the CP-even Higgses for simplicity. The coefficients appearing in front of A^0 ensure that A^0 is orthogonal to the Goldstone boson eaten by the Z boson.

This exponential parameterization of A^0 is convenient for our purposes, since PQ symmetry implies that mass terms involving a and A^0 can only appear in Eq. (3.4). In this basis, the physical degrees of freedom are given by

$$\begin{aligned} a_{\text{phys.}} &= a\cos\theta - A^0 \sin\theta, \\ A^0_{\text{phys.}} &= a\sin\theta + A^0\cos\theta, \end{aligned} \tag{3.7}$$

with

$$\tan\theta \equiv n\,\frac{v_{\text{EW}}}{f_a}\,\frac{\sin 2\beta}{2}\,. \tag{3.8}$$

---

[2] This also means that the physical axion decay constant will be a function of the three vevs. The difference is negligible when $f_a \gg v_{\text{EW}}$, and we will continue to refer to f_a as the axion decay constant.

At this level, the physical axion is massless.[3] A small mass (beyond the contribution from the QCD anomaly) can be generated by a small explicit violation of the PQ symmetry, but the precise way this happens is irrelevant for our discussion.

The dominant decay mode for the axion depends on its mass, m_a. The axion decay width to an $\ell^+\ell^-$ lepton pair is given by

$$\Gamma(a \to \ell^+\ell^-) = n^2 \sin^4\beta \, \frac{m_a}{16\pi} \, \frac{m_\ell^2}{f_a^2} \sqrt{1 - \frac{4m_\ell^2}{m_a^2}} \, . \tag{3.9}$$

For $2m_e < m_a < 2m_\mu$, the dominant decay is $a \to e^+e^-$. In this mass range, however, strong bounds already exist from $K \to \pi a$ decays [98, 99]. With the axion decay to fermions being proportional to their mass-squared, $a \to \mu^+\mu^-$ dominates over $a \to e^+e^-$ for $m_a > 2m_\mu$. Note that in the mass range given in Eq. (3.1), the axion decays within the detector as long as $f_a \lesssim 1000$ TeV.

The axion decay becomes more complicated at higher masses when hadronic decay modes open up. Ref. [30] estimated that the $a \to 3\pi$ channel starts to dominate over the $\mu^+\mu^-$ channel at $m_a \simeq 800$ MeV. Hadronic channels dominate the axion decay until $m_a \gtrsim 2m_\tau$, when the $\tau^+\tau^-$ channel becomes dominant. However, as emphasized recently in [100], throughout the entire mass range $2m_\mu < m_a < 2m_b$, the branching ratio to $\mu^+\mu^-$ remains significant, and until the $\tau^+\tau^-$ threshold, it never drops below $\mathcal{O}(10^{-2})$. For $m_a > 2m_\tau$, the branching fraction to muons is approximately

$$\mathrm{Br}(a \to \mu^+\mu^-) \simeq \frac{m_\mu^2}{m_\tau^2} \simeq 0.003, \tag{3.10}$$

with the precise value depending on $\tan\beta$ through $\Gamma(a \to c\bar{c})$ and on the neglected phase space factor.

3.3 The Effective $b \to sa$ Coupling

By assumption, the physical axion state dominantly couples to standard model fields via its mixing with A^0. Therefore, at one-loop level, the amplitude for $b \to sa$ can be derived from

$$\mathcal{M}(b \to sa) = -\sin\theta \times \mathcal{M}(b \to sA^0)_{\mathrm{2HDM}}, \tag{3.11}$$

where “2HDM” refers to a (PQ-symmetric) 2HDM with no S field. Moreover, since the final state only contains a single axion field, there is no difference in the relevant Feynman rules between the exponential parameterization in Eq. (3.5) and the standard linear parameterization of A^0 in the two Higgs doublet literature. For concreteness, we will consider a type-II (MSSM-like) 2HDM.[4]

---

[3] For completeness, the physical A^0 mass is given by $m^2(A^0_{\mathrm{phys.}}) = \lambda\,(f_a)^n\,(2/\sin 2\beta)(1 + \tan^2\theta)$.

[4] The type-I 2HDM model gives the same $b \to sA^0$ amplitude to the order we are working; see Ref. [91].

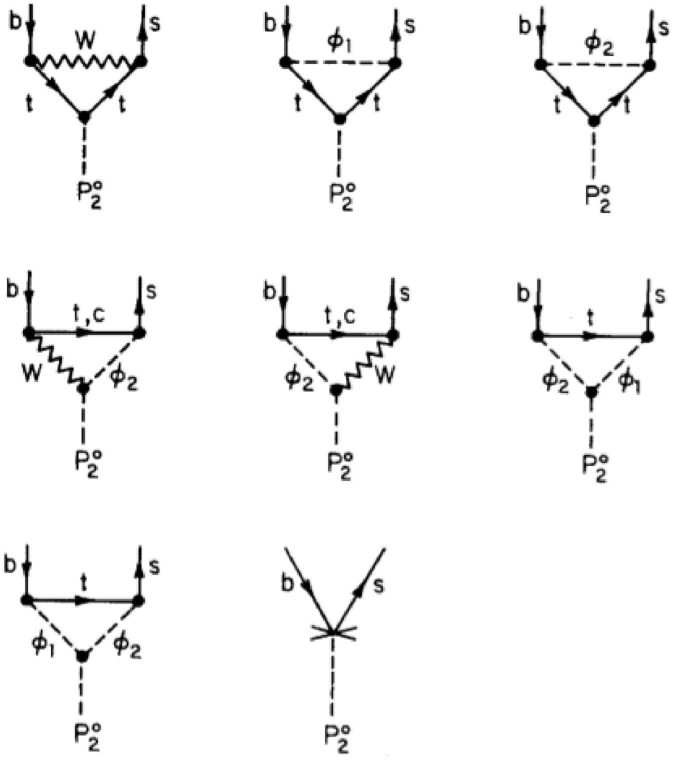

Figure 3.1: Diagrams contributing to $b \to sA^0$ coupling. Here ϕ_1 and ϕ_2 correspond to the charged Goldstone mode and the charged Higgs respectively, while P_2^0 is what is termed A^0 elsewhere. Figure from Ref. [91]

The radiatively induced $b \to sA^0$ coupling in a type-II 2HDM was calculated in the early 1980's independently in two papers [91, 92]. The dominant contributions come from penguin diagrams involving a top quark, a W boson and/or charged Higgs $H^\pm$ boson, and the $t\,\bar{t}A^0$ or $W^\pm H^\mp A^0$ couplings (and corresponding counterterms), as can be seen in Fig. 3.1. The one-loop $b \to sA^0$ amplitude is reproduced to lowest order (in the $m_{B,A^0} \ll m_{W,t,H}$ limit) by the tree-level matrix element of the effective Hamiltonian [91, 92][5]

$$\mathcal{H} = \frac{g^3\, V_{ts}^* V_{tb}}{128\,\pi^2}\, \frac{m_t^2}{m_W^3} \left(X_1 \cot\beta + X_2 \cot^3\beta\right) \bar{s}\gamma^\mu P_L b\, \partial_\mu A^0. \tag{3.12}$$

---

[5] The results published in these two papers differ, a fact which seems to have gone unnoticed—or at least unremarked upon—in the literature. We have redone the calculations both in the unitary gauge and in the Feynman gauge and agree with the result in Ref. [91]. We also agree with Ref. [92] if we replace in their Eq. (9) the second $\ln(m_t^2/m_W^2)$ term by $\ln(m_t^2/m_H^2)$, most likely indicating a simple typographical error. Several papers in the literature seem to use the result as printed in Ref. [92], which has qualitatively wrong implications. For example, it exhibits decoupling in the $m_H \to \infty$ limit and singularities when $m_H \to m_t$, whereas the correct result does not.

The functions X_1 and X_2 depend on the charged Higgs boson mass m_H, and are given by

$$\begin{aligned}
X_1 &= 2+\frac{m_H^2}{m_H^2-m_t^2}-\frac{3m_W^2}{m_t^2-m_W^2} \\
&\quad+\frac{3m_W^4(m_H^2+m_W^2-2m_t^2)}{(m_H^2-m_W^2)\,(m_t^2-m_W^2)^2}\ln\frac{m_t^2}{m_W^2} \\
&\quad+\frac{m_H^2}{m_H^2-m_t^2}\left(\frac{m_H^2}{m_H^2-m_t^2}-\frac{6m_W^2}{m_H^2-m_W^2}\right)\ln\frac{m_t^2}{m_H^2}\,, \\
X_2 &= -\frac{2m_t^2}{m_H^2-m_t^2}\left(1+\frac{m_H^2}{m_H^2-m_t^2}\ln\frac{m_t^2}{m_H^2}\right). \qquad (3.13)
\end{aligned}$$

From this effective Hamiltonian, we can calculate various B decay rates in the 2HDM. These are summarized in App. B for $B \to Ka$, $B \to K^*a$, and the inclusive $B \to X_s a$ rates. Using Eq. (3.11), the rates in any of these channels relevant for the axion portal are determined by

$$\Gamma(B \to Ka) = \sin^2\theta \times \Gamma(B \to KA^0)_{\text{2HDM}}. \qquad (3.14)$$

3.4 Experimental Bounds

In the parameter range of interest, the axion has a significant decay rate to leptons and decays promptly on collider timescales. Thus, the axion would manifest itself as a narrow dilepton peak in $b \to s\ell^+\ell^-$ decays.

The $b \to sa \to s\,\ell^+\ell^-$ process contributes to both inclusive and exclusive $B \to X_s\ell^+\ell^-$ decays [101, 102]. These final states receive large long-distance contributions from intermediate J/ψ and ψ' resonances decaying to $\ell^+\ell^-$, which result in removing the surrounding $q^2(\equiv m^2_{\ell^+\ell^-})$ regions from the measurements. The so-called low-q^2 region ($q^2 \lesssim 7-8$ GeV^2) can probe axion masses up to $m_a \sim 2.7$ GeV, while the high-q^2 region ($q^2 \gtrsim 14$ GeV^2) is above the $a \to \tau^+\tau^-$ threshold. In general, one can bound the axion contribution in both these regions.

In the low-q^2 region, and especially for $m_a \lesssim 800$ MeV as in Eq. (3.1), the exclusive mode $B \to K\ell^+\ell^-$ is particularly well-suited to constrain $b \to sa$. This is because $\mathrm{d}\Gamma(B \to K\ell^+\ell^-)/\mathrm{d}q^2$ varies slowly at small q^2, and $B \to K\ell^+\ell^-$ has a smaller rate than $B \to K^*\ell^+\ell^-$, thus it gives us the best bound by simply looking at the measured spectrum. In contrast, the exclusive $B \to K^*\ell^+\ell^-$ and the inclusive $B \to X_s\ell^+\ell^-$ decay modes receive large enhancements from the electromagnetic penguin operator, whose contribution rises steeply at small q^2, as $1/q^2$. This will complicate looking for a small excess in these modes in this region.

For $m_a \gtrsim 1$ GeV, we expect that the bounds from $B \to K\ell^+\ell^-$ and $K^*\ell^+\ell^-$ may be comparable (possibly even from $B \to X_s\ell^+\ell^-$ if a super B-factory is constructed), and a dedicated experimental analysis should explore how to set the strongest bound, using the rate predictions in App. B. For the remainder of this chapter, we focus on $B \to K\ell^+\ell^-$.

Since $B \to Ka$ contributes mostly to the $K\mu^+\mu^-$ final state, and much less to Ke^+e^-, to set the best possible bound on $B \to Ka$, one needs the $B \to K\mu^+\mu^-$ and $B \to Ke^+e^-$ spectra separately. This information does not seem to be available in the published papers [103, 104, 105]. Based on the latest world average, $\mathrm{Br}(B \to K\ell^+\ell^-) = (4.5 \pm 0.4) \times 10^{-7}$ [106, 103, 104, 105], and the spectrum in Fig. 1 in Ref. [104], it seems to us that

$$\mathrm{Br}(B \to Ka) \times \mathrm{Br}(a \to \mu^+\mu^-) < 10^{-7} \tag{3.15}$$

is a conservative upper bound for any value of the axion mass satisfying $m_a < m_B - m_K$.

As we emphasized, BaBar, Belle, and a possible super B-factory should be able to set a better bound on a narrow resonance contributing to $B \to K^{(*)}\mu^+\mu^-$ but not to $B \to K^{(*)}e^+e^-$. Moreover, LHCb will also be able to search for deviations from the standard model predictions in $B \to K^{(*)}\ell^+\ell^-$ with significantly improved sensitivity. While we could not find a recent LHCb study for the K mode (only for K^*), the fact that the signal to background ratio at the e^+e^- B-factories is not worse in $B \to K\ell^+\ell^-$ than in $B \to K^*\ell^+\ell^-$ suggests that LHCb should be able to carry out a precise measurement [107]. Interestingly, since the $B \to Ka$ signal is essentially a delta function in q^2, the bound in Eq. (3.15) can be improved as experimental statistics increase by considering smaller and smaller bin sizes, without being limited by theoretical uncertainties in form factors [108] (or by nonperturbative contributions [109]). The bound on f_a will increase compared to the results we obtain in the next section, simply by scaling with the bound on $1/\sqrt{\mathrm{Br}(B \to Ka)}$.

3.5 Interpretation

We now derive the bounds on f_a using the calculated $B \to Ka$ branching ratio in Eq. (3.14) and the experimental bound in Eq. (3.15). We start with the axion portal scenario with $\mathrm{Br}(a \to \mu^+\mu^-) \sim 100\%$ and where $\sin\theta$ is defined in terms of f_a by Eq. (3.8). We will then look at the bound on more general scenarios, including the light Higgs scenario in the NMSSM.

For the axion portal, Fig. 3.2 shows the constraints on f_a as a function of $\tan\beta$ and m_H, the charged Higgs boson mass[6]. For concreteness, we take $n = 1$; other values of n correspond to a trivial scaling of f_a. In the mass range in Eq. (3.1), the dependence on m_a is negligible for setting a bound. The bound on f_a is in the multi-TeV range for low values of $\tan\beta$ and weakens as $\tan\beta$ increases. At each value of $\tan\beta$, there is a value of m_H for which the $b \to sa$ amplitude in Eq. (3.12) changes signs, indicated by the dashed curve in Fig. 3.2, along which the bound disappears. Higher order corrections will affect where this cancellation takes place, but away from a very narrow region near this dashed curve, the derived bound is robust. The region $\tan\beta < 1$ is constrained by the top Yukawa

---

[6] While this chapter was being completed, Ref. [110] appeared, which claims much stronger bounds on f_a than our result. They use a different effective Hamiltonian from Eq. (3.12), which does not include the effect of charged Higgs bosons, crucial for bounding DFSZ-type axions.

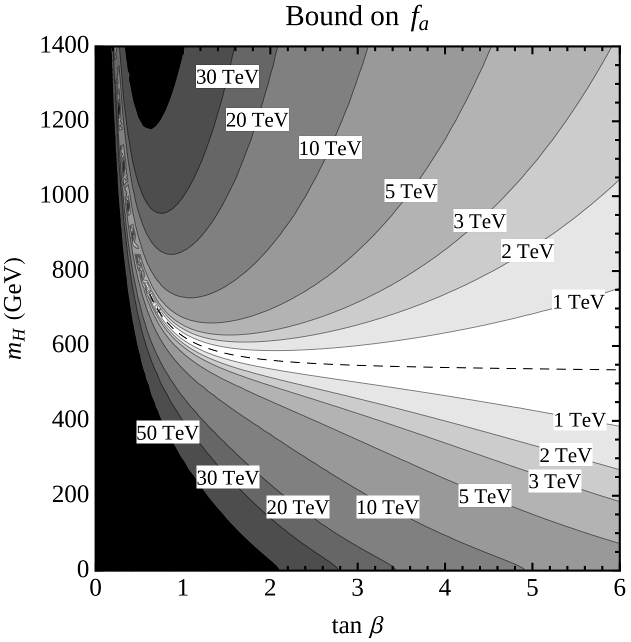

Figure 3.2: Bounds on f_a as a function of $\tan\beta$ and m_H for $n = 1$ in Eq. (3.8), for $m_a^2 \ll m_B^2$. For each displayed value of f_a there are two contour lines, and the region between them is allowed for f_a below the shown value. The bound disappears along the dashed curve, and gets generically weaker for larger $\tan\beta$.

coupling becoming increasingly nonpertubative; this region is included in Figs. 3.2 and 3.4, nevertheless, to provide a clearer illustration of the parametric dependence of the bounds.

As one goes to large values of $\tan\beta$, the X_1 piece of Eq. (3.12) dominates, and $\sin(2\beta)/2 = 1/\tan\beta + \mathcal{O}(1/\tan^3\beta)$. In this limit, the constraint takes a particularly simple form that only depends on the combination $f_a \tan^2\beta$, as shown in Fig. 3.3. Except in the region close to $m_H \sim 550$ GeV, the bound is better than $f_a \tan^2\beta \gtrsim$ few × 10 TeV.

These $B \to Ka$ bounds are complementary to those recently set by BaBar [96] in $\Upsilon(nS) \to \gamma\, a \to \gamma\, \mu^+\mu^-$:

$$f_a \gtrsim (1.4 \text{ TeV}) \times \sin^2\beta\,. \tag{3.16}$$

For example, for $m_H \simeq 400$ GeV, the Υ bound dominates for $\tan\beta \gtrsim 5$, while $B \to Ka$ dominates for $\tan\beta \lesssim 5$.

The bounds in Figs. 3.2 and 3.3 apply for a generic axion portal model where m_H and $\tan\beta$ are free parameters. One would like some sense of what the expected values of m_H and $\tan\beta$ might be in a realistic model. Ref. [30] considered a specific scenario based on the PQ-symmetric NMSSM [97]. In that model small $\tan\beta$ is preferred, since large $\tan\beta$ requires fine-tuning the Higgs potential. In addition, m_H is no longer a free parameter and

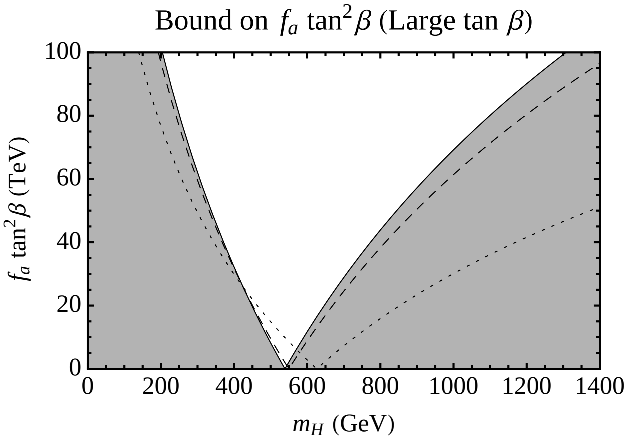

Figure 3.3: The shaded regions of $f_a \tan^2\beta$ are excluded in the large $\tan\beta$ limit. To indicate the region of validity of the large $\tan\beta$ approximation, the dashed (dotted) curve shows the bound for $\tan\beta = 3$ ($\tan\beta = 1$).

is approximately related to the mass of the lightest CP-even scalar s_0 via

$$m_H^2 \simeq m_W^2 + \left(\frac{2}{\sin^2 2\beta}\,\frac{m_{s_0} f_a}{v_{\mathrm{EW}}}\right)^2 . \tag{3.17}$$

In the context of dark matter, Ref. [30] required m_{s_0} to be $\mathcal{O}(10\text{ GeV})$ to achieve a Sommerfeld enhancement. Taking $m_{s_0} = 10$ GeV and $f_a = 2$ TeV as a benchmark, the $B \to Ka$ bound requires $2.5 \lesssim \tan\beta \lesssim 3.0$, corresponding to 490 GeV $\lesssim m_H \lesssim$ 650 GeV, in the vicinity of the cancellation region. This bound is very sensitive to m_{s_0}; for $m_{s_0} = 20$ GeV and $f_a = 2$ TeV, the bounds are $1.5 \lesssim \tan\beta \lesssim 1.7$ and 550 GeV $\lesssim m_H \lesssim$ 610 GeV. Note that models like [77] have no preferred value of m_H, can have larger values of f_a, and do not disfavor large $\tan\beta$.

As mentioned, these $B \to Ka$ constraints apply to any scenario where the branching ratio formula in Eq. (3.14) applies, i.e. where the axion couplings are determined via Eq. (3.7), and where $m_a < m_B - m_K$. For example, recent studies of light Higgs bosons in the NMSSM [93, 94, 95] and related dark matter constructions [76, 78] also contain a light pseudoscalar whose couplings to standard model fermions can be described in terms of a mixing angle θ, as in Eq. (3.8).[7] There, the mass of the a field is expected to be $2m_\tau < m_a < 2m_b$, with the $a \to \mu^+\mu^-$ branching fraction estimated in Eq. (3.10).

To show the constraints on such scenarios in a model independent way, we plot the bound on the combination $\sin^2\theta\,\mathrm{Br}(a \to \mu^+\mu^-)$ in Fig. 3.4, in the $m_a^2 \ll m_B^2$ limit for simplicity. We also show the large $\tan\beta$ limit in Fig. 3.5, where the bound is on the combination $\sin^2\theta\,\mathrm{Br}(a \to \mu^+\mu^-)/\tan^2\beta$. To apply these bounds for the case where m_a is not small

---

[7] In the literature, $\sin\theta$ is often referred to as the "non-singlet fraction" $\cos\theta_A$ [94].

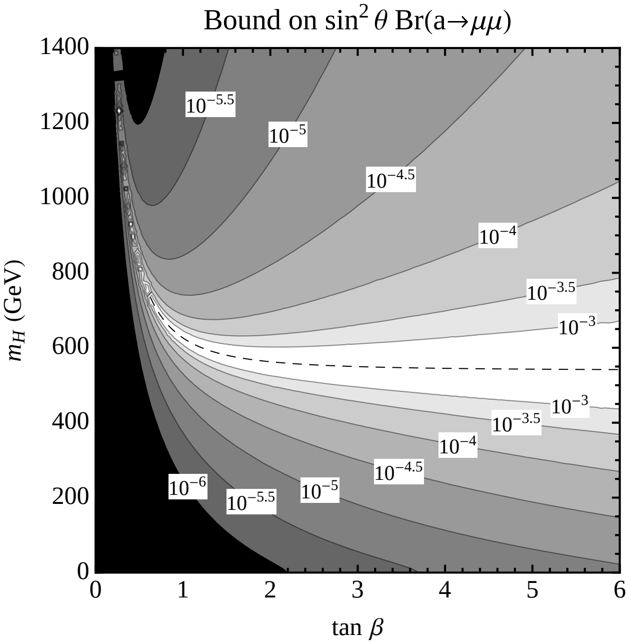
Bound on $\sin^2\theta\,\mathrm{Br}(a\to\mu\mu)$

Figure 3.4: Bounds on $\sin^2\theta\,\mathrm{Br}(a \to \mu^+\mu^-)$ as a function of $\tan\beta$ and m_H. Similar to Fig. 3.2, the successively darker regions going away from the dashed curve are allowed for $\sin^2\theta\,\mathrm{Br}(a \to \mu^+\mu^-)$ above the indicated values. When m_a is not small compared to m_B, these bounds should be modified by Eq. (3.18), but this is a small effect.

compared to m_B, one should make the replacement in Figs. 3.4 and 3.5 (see App. B),

$$\sin^2\theta \;\Rightarrow\; \sin^2\theta\,\frac{\lambda_K(m_a)\,\big[f_0(m_a^2)\big]^2}{(m_B^2 - m_K^2)\big[f_0(0)\big]^2} \equiv \sin^2\theta\,R(m_a)\,. \tag{3.18}$$

Using a simple pole form for the q^2 dependence of f_0 [108], we find that $R(m_a)$ deviates from unity by less than 20% for $m_a < 4.6$ GeV (i.e. nearly over the full kinematically allowed region), and so it is a good approximation to neglect $R(m_a)$. In the case of NMSSM scenarios, the precise bound depends strongly on the parameters of the theory. To give a sense of the strength of the bound, for $m_a \sim 4$ GeV, $m_H \sim 200$ GeV, and using Eq. (3.10), the bound at large $\tan\beta$ implies $\sin^2\theta/\tan^2\beta \lesssim 5\times10^{-4}$ (and $\sin^2\theta \lesssim 2\times10^{-4}$ for $\tan\beta = 1$), which is a significant constraint on large mixing angles or small $\tan\beta$.

3.6 Conclusions

In this chapter, we explored bounds on axion-like states from flavor-changing neutral current $b \to s$ decays. We found that the exclusive $B \to K\ell^+\ell^-$ decay is particularly well-suited to constrain such contributions. In the case of the axion portal (or equivalently,

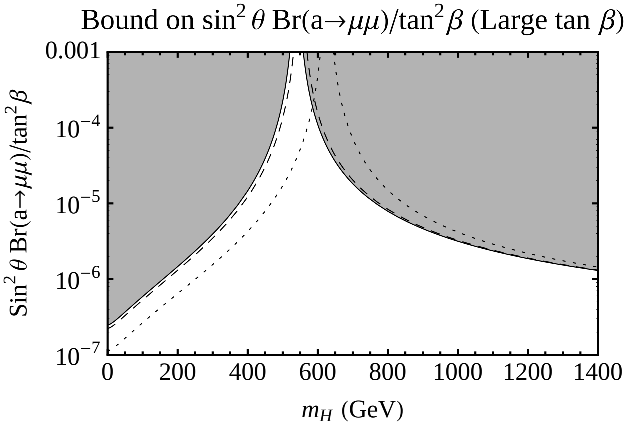

Figure 3.5: Bounds on $\sin^2\theta\,\mathrm{Br}(a \to \mu^+\mu^-)/\tan^2\beta$ in the large $\tan\beta$ limit. The shaded region is excluded, and the dashed (dotted) curve shows $\tan\beta = 3$ ($\tan\beta = 1$).

any DFSZ-type axion), we derived a bound from current B-factory data on the axion decay constant f_a. The bound is in the multi-TeV range, gets stronger for small $\tan\beta$, and depends sensitively on the value of the charged Higgs boson mass. This places tension on the axion portal model of dark matter in the parameter space given in Eq. (3.1). More generally, there is a constraint on any pseudoscalar with $2m_\mu < m_a < m_B - m_K$ whose couplings to standard model fermions arise via mixing with the CP-odd Higgs A^0. This is true even if $\mathrm{Br}(a \to \mu^+\mu^-) \sim \mathcal{O}(10^{-3})$, as is the case for light Higgs scenarios in the NMSSM.

We derived our bound using a conservative estimate from the q^2 distribution in $B \to K\ell^+\ell^-$. The bound could be improved through a dedicated search in existing B-factory data, and in searches at LHCb and a possible future super B-factory. The $B \to Ka$ search is complementary to axion searches in $\Upsilon(nS) \to \gamma a$, because for fixed mixing angle θ in a type-II 2HDM, the former scales like $1/\tan^2\beta$ while the latter scales like $\tan^2\beta$.

One way to extend our analysis would be to look at axions decaying to hadronic final states. We focused on the decay mode $a \to \mu^+\mu^-$, since the $a \to e^+e^-$ mode is already well-constrained by kaon decays, and we were motivated by the parameter space relevant for Ref. [30]. However, as the axion mass increases, other decay channels open up, such as $a \to \pi^+\pi^-\pi^0$, $a \to KK^*$, etc. These would also be worthwhile to search for in B-factory data, especially since dark matter models such as [77] are compatible with $a \to \pi^+\pi^-\pi^0$ decays. It appears to us that setting bounds in these modes is more complicated than for $B \to K\ell^+\ell^-$, and should be done in dedicated experimental analyses. For constraining higher mass axions, it would be interesting to study whether B-factories could search for narrow resonances in $B \to K\tau^+\tau^-$ at a level of sensitivity no weaker than m_τ^2/m_μ^2 times the corresponding bound in $B \to K\mu^+\mu^-$. Combining a number of search channels, one would be able to substantially probe scenarios containing light axion-like states.

Chapter 4

On dark matter models with uniquely spin-dependent detection possibilities[1]

4.1 Introduction

The sensitivity of DM direct detection experiments is undergoing rapid progress and is expected to continue in the next decade. There are a number of proposed experiments which will probe complementary aspects of dark matter properties with much better sensitivities than the existing ones: DM mass, spin-independent (SI) and spin-dependent (SD) cross sections, the dependence of the cross sections on the target nuclei, directional information, etc.

The focus, rightly, is often on the detection of spin-independent DM interactions, because, due to a coherence effect, the SI interaction cross section with heavy nuclei is enhanced by A^2, the number of nucleons in a nucleus, and is, therefore, expected in many models to be the dominant interaction in DM detectors.

There is a good chance that, in the not-too-distant future, direct detection experiments will be able to extend their sensitivity to cover the full detectable parameter space for SI cross sections, down to the 10^{-48} cm^2 level, below which atmospheric neutrinos constitute an irreducible background.

Prior studies [112, 113, 114, 115] have considered the relationship between SI and SD cross sections, concluding that the two are typically correlated when a viable dark matter candidate is present. Most of the discussions have been in the context of the minimal supersymmetric standard model. (Similar statements have been made about DM candidates in universal extra dimensions [112] and little Higgs models [114], as well.) In general, the common wisdom is that SI experiments have a much better chance of first direct detection discovery.

The generality of this conclusion cannot be addressed by merely considering operators; one must explore the underlying models which determine relationships between operator

---

[1] This chapter, as well as App. C, was co-written with Zoltan Ligeti and published in [111]

coefficients. For example, the conclusions stated above ultimately stemmed from the assumption of DM with electroweak charges, which generically implies both mediators with at least weak-scale masses to justify null results thus far and couplings to the Higgs leading to SI signals. Once this condition is relaxed, the relationship between SI and SD cross sections becomes weaker, and models in which SD interactions are more easily accessible, or even the only interaction accessible in direct detection experiments, become feasible.

Here we point out that in order to impose the last condition, i.e., uniquely SD detection, the consideration of subleading effects is crucial. Since, due to coherence effects, SI experiments are more sensitive than SD ones (currently by 5 orders of magnitude), a loop-induced SI process might be only marginally more difficult or possibly even as easy to detect than a tree-level SD one. Upon considering these additional operators, we find that models with light pseudoscalars are uniquely capable of generically evading such detection modes.

Although several ingredients of our analysis appear in the literature [116, 117], the impact of light mediators on a general analysis of operators has not been heretofore discussed, and the effect of loop corrections on DM scattering has not been considered in this context. In Sec. 4.2, we review current bounds on SI and SD cross sections and the expected improvements. Sec. 4.3 then constitutes the bulk of this chapter. We discuss operators relevant for the detection of DM particles, including operators which become important in the case of light mediators. We then consider which models could generate exclusively SD interactions, and calculate the loop-induced interactions that would simultaneously be present. In Sec. 4.4 we construct a viable model demonstrating this possibility, in which the SI interaction is out of reach, but the SD interaction may be detected in future experiments. Sec. 4.5 concludes.

4.2 Prospects of Direct Detection

XENON10 [118], CDMS [119], and XENON100 [120] currently provide the best SI direct detection bounds, with the highest sensitivity from XENON100 near 7×10^{-45} cm^2 at 50 GeV. In general, optimal sensitivity is for DM masses of order the mass of the recoiling nucleus. At higher masses, the sensitivity decreases roughly as $1/m_{\rm DM}$. Within the coming years, XENON100, LUX, and SuperCDMS can improve these bounds down to the 10^{-45} cm^2 or possibly near the 10^{-46} cm^2 level. Ultimately multi-ton Xenon or Germanium experiments can achieve sensitivities to 10^{-47} cm^2 or maybe even 10^{-48} cm^2, at which point atmospheric neutrinos form an irreducible background [121, 122, 123], and achieving sensitivity to lower SI DM-nucleon interactions seem unfeasible.

For SD detection, the best current limit for DM-proton interaction is near 4.2×10^{-39} cm^2 from SIMPLE [124] at 35 GeV, with slightly weaker bounds from COUPP [125], KIMS [126], and PICASSO [127], at similar optimal masses as above. For DM-neutron cross sections the best bound is from XENON10 [128] at 5×10^{-39} cm^2 at optimal sensitivity near 30 GeV. Within the next few years, COUPP [129], PICASSO [130], and XENON100 should improve these to few$\times10^{-40}$ cm^2, for both protons and neutrons. These limits could then be extended to near 5×10^{-41} cm^2 with experiments such as DMTPC, or to 5×10^{-43} cm^2 for a 500 kg

Operator		SI / SD	Suppression
$\mathcal{O}_1^s =$	$\phi^2\,\bar{q}q$	SI	—
$\mathcal{O}_2^s =$	$\phi^2\,\bar{q}\gamma^5 q$	SD	q^2
$\mathcal{O}_3^s =$	$\phi^\dagger\partial^\mu\phi\,\bar{q}\gamma_\mu q$	SI	—
$\mathcal{O}_4^s =$	$\phi^\dagger\partial^\mu\phi\,\bar{q}\gamma_\mu\gamma^5 q$	SD	v^2

Table 4.1: Operators relevant for scalar dark matter detection. The suppression factor given is for the relevant cross section. Operators $\mathcal{O}_3^s$ and $\mathcal{O}_4^s$ are only allowed for complex scalars.

extension of COUPP [131].

Bounds on direct detection cross sections can also come indirectly from other experiments. One source is from DM annihilation signals from the Sun. The annihilation at equilibrium is proportional to the rate of DM capture, which is driven by the same interactions as direct detection. In this case the SI terms are not so strongly enhanced over the SD ones, since this capture is mostly due to light nuclei, almost entirely hydrogen and helium. (Some enhancement does occur due to small amounts of Fe and O, but bounding the SD interaction neglecting the SI contribution is conservative.) Super-Kamiokande [132] and IceCube [133] used this to place limits on SD proton interactions at around 10^{-38} cm^2, assuming annihilations primarily to $b\bar{b}$. Above $m_{\rm DM} \sim 250$ GeV, IceCube could even place a bound at 2×10^{-40} cm^2 if the DM annihilated to W^+W^-. However, these indirect bounds do not apply in the case of light mediators which will be discussed below, since if the annihilations proceed through a light on-shell particle, decays to neither heavy quarks nor W bosons occur.

Other bounds can be placed from constraints on operators from collider searches [134, 135, 136]. In cases where the mediator can be integrated out, these searches place bounds on interactions of very light dark matter better than those of direct detection, while remaining competitive with them for SD interactions of DM that can be directly produced at the Tevatron. The expected LHC reach is expected to also remain competitive with direct detection sensitivites of upcoming expierments [135]. However, for mediators light enough to be produced on-shell, the bound deteriorates rapidly [136], and is also not applicable for the class of models we discuss below.

4.3 General Considerations

4.3.1 Operator Analysis

In order to survey possible models, we first identify all operators through which dark matter may interact with detectors. In doing so, we will see which interactions give us the signals we are looking for, and which operators need to be suppressed by small coefficients or forbidden by symmetries. Similar operator analyses have been considered before in Refs. [117,

Operator	SI / SD	Suppression
$\mathcal{O}_1^f = \bar{\chi}\chi\,\bar{q}q$	SI	—
$\mathcal{O}_2^f = \bar{\chi}i\gamma^5\chi\,\bar{q}q$	SI	q^2
$\mathcal{O}_3^f = \bar{\chi}\chi\,\bar{q}i\gamma^5 q$	SD	q^2
$\mathcal{O}_4^f = \bar{\chi}\gamma^5\chi\,\bar{q}\gamma^5 q$	SD	q^4
$\mathcal{O}_5^f = \bar{\chi}\gamma^\mu\chi\,\bar{q}\gamma_\mu q$	SI	—
$\mathcal{O}_6^f = \bar{\chi}\gamma^\mu\gamma^5\chi\,\bar{q}\gamma_\mu q$	SI	v^2
	SD	q^2
$\mathcal{O}_7^f = \bar{\chi}\gamma^\mu\chi\,\bar{q}\gamma_\mu\gamma^5 q$	SD	v^2 or q^2
$\mathcal{O}_8^f = \bar{\chi}\gamma^\mu\gamma^5\chi\,\bar{q}\gamma_\mu\gamma^5 q$	SD	—
$\mathcal{O}_9^f = \bar{\chi}\sigma^{\mu\nu}\chi\,\bar{q}\sigma_{\mu\nu}q$	SD	—
$\mathcal{O}_{10}^f = \bar{\chi}i\sigma^{\mu\nu}\gamma^5\chi\,\bar{q}\sigma_{\mu\nu}q$	SI	q^2

Table 4.2: Operators relevant for fermionic dark matter detection. Operators $\mathcal{O}_5^f$, $\mathcal{O}_7^f$, $\mathcal{O}_9^f$, $\mathcal{O}_{10}^f$ only exist if the dark matter is Dirac. Notations as in Table 4.1.

137, 113]. We present it here as a guide to possible types of underlying structure.

We assume that the mediator is heavy enough so that for the purposes of direct detection, describing the interaction of dark matter via a contact term is a reasonable approximation. Beyond this, we want to consider interactions with dark matter of arbitrary spin, without making additional assumptions, such as parity conservation. At the structural level of the operators this encompasses both elastic and inelastic scattering. Having two (or more) fields of different mass in the DM sector only leads to differences in kinematics and the presence of operators that are otherwise zero for Majorana fermions and real bosons for symmetry reasons (discussed below).

The smallest number of possible operators, as expected, are furnished by scalar dark matter candidates. These are listed in Table 4.1. Note that $\mathcal{O}_3^s$ and $\mathcal{O}_4^s$ are nonvanishing only if the dark matter candidate is complex.

For fermionic dark matter, the possible operators are listed in Table 4.2. If the dark matter candidate is a Majorana fermion, the operators $\mathcal{O}_5^f$, $\mathcal{O}_7^f$, $\mathcal{O}_9^f$, $\mathcal{O}_{10}^f$ are absent, as they are odd under charge conjugation. There are only two operators with tensor couplings. Since $\sigma^{\mu\nu}\gamma^5 = i\epsilon^{\mu\nu\rho\sigma}\sigma_{\rho\sigma}/2$, not all (pseudo)tensor-(pseudo)tensor combinations are linearly independent. In addition, $\mathcal{O}_7^f$ has separate SD terms suppressed independently by v^2 and q^2, while $\mathcal{O}_6^f$, commonly referred to as the anapole moment coupling, has contributions to both SI and SD cross sections with different suppression factors. (Here, as elsewhere in this chapter, v is the velocity of DM in the halo, approximately 10^{-3}, while q is the momentum transfer in the interaction.)

Finally, in Table 4.3, we give the possible operators for vector dark matter candidates. Similar to the case of scalar dark matter, the operators $\mathcal{O}_3^v$ and $\mathcal{O}_4^v$ are only present if the vector is complex.

Operator	SI / SD	Suppression
$\mathcal{O}_1^v = B^\mu B_\mu \, \bar{q}q$	SI	—
$\mathcal{O}_2^v = B^\mu B_\mu \, \bar{q}\gamma^5 q$	SD	q^2
$\mathcal{O}_3^v = B^\dagger_\mu \partial^\nu B^\mu \, \bar{q}\gamma_\nu q$	SI	—
$\mathcal{O}_4^v = B^\dagger_\mu \partial^\nu B^\mu \, \bar{q}\gamma_\nu \gamma^5 q$	SD	v^2
$\mathcal{O}_5^v = B^\mu \partial_\mu B^\nu \, \bar{q}\gamma_\nu q$	SI	$v^2 q^2$
$\mathcal{O}_6^v = B^\mu \partial_\mu B^\nu \, \bar{q}\gamma_\nu \gamma^5 q$	SD	q^2
$\mathcal{O}_7^v = \epsilon_{\mu\nu\rho\sigma} B^\mu \partial^\nu B^\rho \, \bar{q}\gamma^\sigma q$	SI	v^2
	SD	q^2
$\mathcal{O}_8^v = \epsilon_{\mu\nu\rho\sigma} B^\mu \partial^\nu B^\rho \, \bar{q}\gamma^\sigma \gamma^5 q$	SD	—

Table 4.3: Operators relevant for vector dark matter detection. Operators $\mathcal{O}_3^v$ and $\mathcal{O}_4^v$ only exit for complex vectors fields. Notations as in Table 4.1.

There are a large number of operators that could mediate SD interactions. However, for our purposes, some of these may be ignored right away. For example, $\mathcal{O}_6^f$ and $\mathcal{O}_7^v$ lead to both SD and SI interactions of comparable magnitudes. It may naively seem that all operators that come with kinematic suppression factors can be dismissed just as easily. After all, with DM in the galactic halo at such low velocities, the nonrelativistic limit is appropriate for detection, and traditionally such operators have indeed been neglected. Let us examine this assumption more carefully.

Within the dominant WIMP paradigm, the mediator has typically been assumed to be at the weak scale, with direct detection occurring with $\mathcal{O}(100$ MeV$)$ momentum transfers and $\mathcal{O}(100$ keV$)$ recoil energies. In that case, the integrated-out mediator sets the scale of the operators through a factor of $1/m_W^2$. In the nonrelativistic limit, terms like $\bar{\psi}\gamma^5\psi$ are suppressed by factors of $|\vec{q}|/2m_N$ or $|\vec{q}|/2m_{\rm DM}$, while others, like $\bar{\psi}\gamma^\mu\gamma^5\psi$, have some components scale as v. Operators with any of these factor can typically be dismissed, because they are suppressed by $O(10^3)$. This means that, even if present, such interactions can be ignored. For example, in the case of Majorana fermion dark matter, such as the neutralino in supersymmetric models, the only two operators that need to be considered are scalar – scalar and axial-vector – axial-vector [138, 122, 139]; all others are highly suppressed.

However, recent interest in explaining various possibly DM-related anomalies have introduced models with $O($GeV$)$ mediator particles. In this case, if the leading operators were suppressed or forbidden for some symmetry reason, the traditionally subleading operators could lead to contributions of the correct magnitude to be accessible to current or future direct detection experiments. As pointed out in Ref. [140], these two statements may in fact be connected, since the spontaneous breaking of a symmetry forbidding the appearance of certain operators can provide for a natural explanation for the presence of light (pseudo) Nambu–Goldstone scalars.

This opens up new possibilities. If SI operators without kinematic suppression actors are forbidden or highly suppressed for other reasons, the set of operators which may lead to a detectable SD signal becomes much larger.

4.3.2 Renormalizable Models

If we wish to remain agnostic about the nature of the DM-nucleon interactions, we can say no more. However, if a further step is to be taken, it seems most conservative to assume that the DM comes from some theory with renormalizable interactions in which the operators leading to direct detection come from heavy states that have been integrated out. One can then ask what sort of renormalizable interactions could lead to the operators given above. Such a procedure was followed in Ref. [116]. Here we quote their results, along with the additional possibilities afforded by interactions yielding kinematically suppressed operators.

For scalar DM, the only option for generating solely SD operators seems to be a t-channel exchange of a light pseudoscalar, which yields $\mathcal{O}_2^s$. While such an interaction breaks parity, given that parity is badly broken already in the standard model (SM), this is not a serious concern.

For fermionic DM, several possibilities present themselves. Once again a t-channel light pseudoscalar exchange produces solely SD interactions via $\mathcal{O}_4^f$. Additionally, for Majorana fermions, the t-channel exchange of a vector with axial couplings, either the SM Z or a new Z', will generate only a single kinematically unsuppressed operator, $\mathcal{O}_8^f$. Other options are an s or u-channel coupling through either a scalar or vector, provided the couplings are chiral, in which case $\mathcal{O}_8^f$ is generated again. If the couplings are not chiral, $\mathcal{O}_1^f$ is produced as well.

Finally, for vector DM, a light pseudoscalar in the t channel produces only $\mathcal{O}_2^v$, which breaks parity as in the scalar case. Alternatively an s or u-channel coupling through a fermion makes $\mathcal{O}_8^v$ the leading operator, if the coupling is chiral while the vector boson is real.

4.3.3 Loops and Subleading Interactions

Suppose that one is presented with a model in which one of the above SD interactions is the only one present, or dominant over other by many orders of magnitude. Does that mean that only an experiment sensitive to SD interactions would see a signal? Not necessarily.

The bounds on SI cross sections are currently $5-7$ orders of magnitude higher than the SD ones, and this looks to continue to be the case in the future. Therefore if any of the SD interactions discussed above induce subleading SI couplings, such an effect could potentially be visible in a SI experiment. There are two sources for such effects. First, there are kinematically suppressed contributions of tree level scattering that were ignored above. These are easily estimated from Tables 4.1–4.3 given earlier. Second, the tree-level SD interactions can induce SI couplings at loop level. These are not as simple to estimate, and should be calculated to confirm their effect.

Let us consider a Z (or Z' exchange) with a Majorana fermion, as in Fig. 4.1a. While the dominant contribution comes from $\mathcal{O}_8^f$, also present is $\mathcal{O}_6^f$, the anapole coupling. We see that

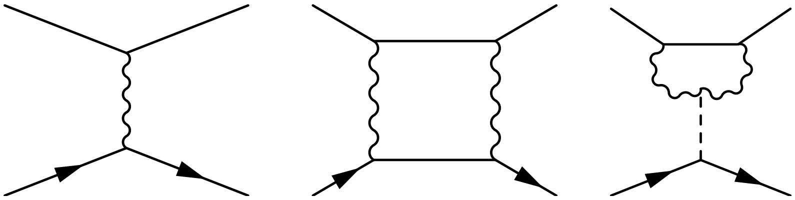

(a) Tree level

(b) Loop processes

Figure 4.1: The tree and loop level contributions to scattering of Majorana fermions through a Z boson. For all box diagrams, the crossed box diagram is included in calculations but not depicted. In the last diagram, a Higgs mediates the scattering through a Z loop.

this gives rise to a SI interaction suppressed by v^2. Similarly, both the scalar exchange of Fig. 4.2a and the equivalent diagram for vector exchange give an anapole coupling after using Fiertz identities. A fermion exchange of the same form in the case of vector DM produces $\mathcal{O}_7^v$ as well as $\mathcal{O}_8^v$ in the chiral limit, which again mediates a v^2 suppressed SI coupling. In all of these cases, there is a SI scattering cross section no more than $O(10^6)$ smaller than the SD one, independent of any other field content of a model. This means that such interactions would be seen in SI experiments simultaneously or in the next generation of experiements after they appear in SD ones. Only the pseudoscalar exchanges evade this, as they lead to no v^2 suppressed subleading contributions to DM-nucleon scattering at all.

All the aforementioned interactions should also be computed at the one-loop level. While these will be suppressed by loop factors and extra couplings, they may also generate SI interactions. For large enough couplings, these loops might even give rise to interactions larger than the kinematically-suppressed ones discussed above, and so might be even more readily detectable.

Without making any further assumptions about the underlying model, we can already identify diagrams which will produce SI interactions at loop-level. For SD interactions involving a t-channel exchange, at a minimum, exchanging two mediators in a box diagram will give rise to a SI interaction. For an s or u-channel processes, a SI loop level contribution can come from a loop with W or Z bosons exchanged between the quarks.

Consider the exchange of a Z with axial couplings to quarks. (We will discuss the case of a Z' shortly.) In that case, the quark level operator for tree-level scattering (Fig. 4.1a) is

$$\frac{g_2^2}{2\cos^2\theta_W}\,T_3^q\,\frac{Q}{2}\,\frac{1}{m_Z^2}\,\bar{\chi}\gamma^\mu\gamma^5\chi\,\bar{q}\gamma_\mu\gamma^5 q\,, \tag{4.1}$$

where Q is the coupling of the DM to the Z. Then the DM-proton SD cross section generated is (see Apps. C.1 and C.2 for details)

$$\sigma_{\rm SD}^{\chi p} \approx (1.5\times 10^{-39}\ {\rm cm}^2)\left(\frac{Q}{0.1}\right)^2, \tag{4.2}$$

(a) Tree level

(b) Loop processes

Figure 4.2: The tree and loop level contributions to scattering of Majorana fermions through a s-channel scalar.

with the DM-neutron cross sections about 20% smaller. In this case, two one-loop processes lead to SI effective interactions: one with two Z exchanges, and a Higgs coupling through a Z loop to the DM (Fig. 4.1b). We work in the limit $m_q \ll m_Z \ll m_{\mathrm{DM}}$. (This limit is generally the one in which the DM has the correct relic abundance in models where the only coupling of the DM to the quarks is through electroweak bosons, while foregoing the last inequality only yields $O(1)$ changes, see Ref. [141].) The SI contribution to the effective coupling is then [142, 141][2]

$$\frac{1}{4\pi}\,\frac{g_2^4\,Q^2}{\cos^4\theta_W\,m_Z}\left[\frac{(T_3^q)^2}{2m_Z^2}+\frac{1}{4m_h^2}\right]m_q\,\bar{\chi}\chi\,\bar{q}q\,. \tag{4.3}$$

Taking a reference value of $m_h = 120$ GeV, this interactions will induce a SI cross section of

$$\sigma_{\mathrm{SI}}^{\chi N} = (4\times 10^{-47}\ \mathrm{cm}^2)\left(\frac{Q^2}{0.1}\right)^2. \tag{4.4}$$

Asking that the SD signal be just beyond current SD experimental bounds implies $Q \sim 0.3$, giving a SI cross section of 4×10^{-47} cm^2. This, while not detectable in experiments underway, is feasible with ones in preparation.

This result would make the v^2-suppressed constribution to SI scattering dominant. However, it is worth mentioning that this cross section acts as a lower bound — it could be that the DM particle is part of larger representation of $SU(2)$, in which case additional loops involving Ws would also contribute. Generally, the size off the cross section grows as n^2,

---

[2] In deriving this result, along with those following, we have set several quark operators, such as

$$m_q\bar{\chi}\chi\bar{q}q,\quad \bar{\chi}\chi\bar{q}i\not{\partial}q,$$
$$\frac{4}{3m_{\mathrm{DM}}}\,\bar{\chi}i\partial_\mu\gamma_\nu\chi\,\bar{q}i\left(i\partial^\mu\gamma^\nu+\partial^\nu\gamma^\mu-\frac{1}{2}g^{\mu\nu}\not{\partial}\right)q,$$

which all simplify to $m_q\,\bar{\chi}\chi\,\bar{q}q$ on shell, but can have different nuclear matrix elements, to their on-shell value. In fact this seems to yield a conservative estimate, as out of the nuclear matrix elements known, the first one has the smallest value (for a detailed discussion of these issues see Ref. [143]).

(a) Tree level (b) Loop processes

Figure 4.3: The tree and loop level contributions to scattering DM mediated by a light pseudoscalar. The dotted line can represent either a scalar, fermion, or vector boson.

with n the dimension of the representation [142], making it possible for the loop contribution to be dominant, and not merely competitive with the kinetically suppressed contribution, and even being large enough to be discovered simultaneously with the SD signal.

If one wishes to consider models with a new Z', then the existence of a Z' with Higgs coupling becomes model dependent. To talk about a lower bound, we can then ignore the contribution of the second term in the effective coupling. The heavier mediator mass that such a model would entail would have to be offset with a larger coupling in order to be detectable. Thus, at loop level, one would generally expect the effective interaction to be of at least similar size, or possibly larger, due to the higher power of the coupling appearing in the loop-induced term.

If one considers the possibility of a light Z', which are not ruled out by collider constraints down to the GeV range for gauge couplings smaller than the SM by 10^{-2}, the situation discussed above would be reversed, and one would expect a smaller loop-induced contribution. However, the SI contribution due to kinematically suppressed operators is insensitive to changes in the mediator mass, and would still be present. Constructing a model without such operators and without significant fine-tuning seems extremely difficult. It is difficult to say more in generality, due to the large freedom in assigning masses and charges under a new gauge group.

Now let us consider DM with chiral couplings to the SM via an s or u-channel. The most model-independent loop-level processes here come from box diagrams with the quarks exchanging a W or Z boson, an example of which is given in Fig. 4.2b. The contributions of the loops have completely different forms depending on whether the coupling of the DM is left- or right-handed. However, in all cases the loop-level processes only give rise to suppressed SD contributions. In addition to DM of the form in Fig. 4.2, this is also true for the cases of fermionic DM with a vector mediator and vector DM with a fermion mediator of similar topologies. In this case, we find that the most reliable lower bound on a SI cross section in this case comes from the v^2 suppressed contribution to the tree-level interaction discussed earlier.

Finally, let us turn to the box diagrams induced in the cases of light pseudoscalar exchange, Fig. 4.3b. First, we consider the case of scalar DM. At tree level, the operator obtained after integrating out the pseudoscalar is

$$\frac{1}{m_a^2}\,\xi\,y_q\,m_\phi\,\phi^\dagger\phi\,\bar{q}i\gamma^5 q, \tag{4.5}$$

where y_q is the Yukawa coupling of the quark, so ξ absorbs both the coupling of the DM and mediator, and any scaling to Yukawas of the mediator-quark coupling. This leads to a a tree-level cross section of

$$\sigma_{\mathrm{SD}}^{\phi p} \approx (8\times 10^{-37}\ \mathrm{cm}^2)\left(\frac{\xi}{0.1}\right)^2\left(\frac{1\ \mathrm{GeV}}{m_a}\right)^4. \tag{4.6}$$

(See App. C.2 for the definition of the cross section in cases of kinematically suppressed operators.) For a mediator with mass of a few GeV and $\xi = 0.01$, this would be accessible to currently running searches.

The calculation of the loop diagram in the same limits as the previous Z-mediated case does not give as compact of an answer, but can be expressed in closed form in terms of Passarino–Veltman scalar integrals [144], computed with the use of `FeynCalc` [145] as

$$\begin{aligned}\frac{1}{(4\pi)^2}\,\xi^2\,y_q^2\,\Big[&C_0(m_\phi^2,0,m_\phi^2;m_\phi^2,m_a^2,0) - C_0(m_\phi^2,m_\phi^2,0;m_a^2,m_\phi^2,m_a^2)\\ &+ m_a^2\,D_0(m_\phi^2,m_\phi^2,0,0,0,m_\phi^2;m_a^2,m_\phi^2,m_a^2,0)\Big]\,\phi^\dagger\partial^\mu\phi\,\bar{q}\gamma_\mu q.\end{aligned} \tag{4.7}$$

A numerical evaluation of the coefficients show the C_0 and D_0 functions with these parameters to scale as $\ln(m_a/m_\phi)$ and $\ln^2(m_a/m_\phi)$, respectively, beyond their overall $1/m_\phi^2$ dependence. Using a fiducial value of $m_a/m_\phi = 0.01$ gives

$$\frac{1}{(4\pi)^2}\,\frac{\xi^2\,y_q^2}{m_\phi^2}\,C_S\,\phi^\dagger\partial^\mu\phi\,\bar{q}\gamma_\mu q\,, \tag{4.8}$$

where $C_S \approx 80$. Note that if the DM were real, this operator vanishes identically, and there is no loop induced coupling at one loop order at all. If present, the cross section induced is

$$\sigma_{\mathrm{SI}}^{\phi N} \approx (4\times 10^{-54}\ \mathrm{cm}^2)\left(\frac{\xi}{0.1}\right)^4\left(\frac{100\ \mathrm{GeV}}{m_\phi}\right)^4, \tag{4.9}$$

undetectable for any any choice of parameters that would make the SD cross section detectable.

The case of vector DM is very similar. For

$$\frac{1}{m_a^2}\,\xi\,y_q\,m_B\,B_\mu^\dagger B^\mu\,\bar{q}i\gamma^5 q, \tag{4.10}$$

the tree-level cross section takes the same value as Eq. (4.6). Meanwhile, the loop induced coupling is

$$\begin{aligned}\frac{1}{(4\pi)^2}\,\xi^2\,y_q^2\,\Big\{&C_0(m_B^2,0,m_B^2;m_B^2,m_a^2,0)-C_0(m_B^2,m_B^2,0;m_a^2,m_B^2,m_a^2)\\&+m_a^2\,D_0(m_B^2,m_B^2,0,0,0,m_B^2;m_a^2,m_B^2,m_a^2,0)\\&+\frac{1}{4m_B^2}\Big[B_0(m_B^2;m_a^2,m_B^2)-B_0(m_B^2;0,m_B^2)\Big]\Big\}\,B_\nu^\dagger\,\partial^\mu B^\nu\,\bar{q}\gamma_\mu q\,,\end{aligned}\tag{4.11}$$

which numerically evaluates to

$$\frac{1}{(4\pi)^2}\frac{\xi^2\,y_q^2}{m_B^2}\,C_V B_\nu^\dagger\,\partial^\mu B^\nu\,\bar{q}\gamma_\mu q\,,\tag{4.12}$$

with $C_V\approx 80$ very close to the scalar case, giving a loop induced SI cross section as in Eq. (4.9), and similarly giving no contribution if the DM were real.

The case of fermionic DM is slightly different. This is because the tree-level operator responsible for scattering is

$$\frac{1}{m_a^2}\,\xi\,y_q\,\bar{\chi}i\gamma^5\chi\,\bar{q}i\gamma^5 q,\tag{4.13}$$

and, therefore, is parametrically suppressed by q^4, instead of the previous cases' q^2. The tree level cross section then becomes

$$\sigma_{\rm SD}^{\chi p}\approx(3\times10^{-43}\ {\rm cm}^2)\left(\frac{\xi}{0.1}\right)^2\left(\frac{1\ {\rm GeV}}{m_a}\right)^4.\tag{4.14}$$

We see that due to the greater momentum suppression, we require a lighter mediator mass and cannot afford the coupling of the DM to be as small as in the bosonic case above. In this case a cross section detectable in current experiments would require, for example, a mediator with $m_a = 100$ MeV and $\xi = 0.1$.

Meanwhile, the effective coupling from computing the loop diagram in the same limits as the other cases is

$$\begin{aligned}\frac{1}{(4\pi)^2}\frac{\xi^2\,y_q^2}{m_\chi^2}\Big\{&\Big[\frac{1}{2}+\frac{m_\chi^2}{2}\,C_0(m_\chi^2,m_\chi^2,0;m_a^2,m_\chi^2,m_a^2)-m_\chi^2\,C_0(0,m_\chi^2,m_\chi^2;0,m_a^2,m_\chi^2)\Big]\,\bar{\chi}\gamma^\mu\chi\,\bar{q}\gamma_\mu q\\&+\frac{3}{8}\Big[1+B_0(m_\chi^2;0,m_\chi^2)-B_0(0;m_a^2,m_a^2)\\&\quad+4m_\chi^2\,C_0(m_\chi^2,0,m_\chi^2;m_\chi^2,m_a^2,0)-m_\chi^2\,C_0(m_\chi^2,m_\chi^2,0;m_a^2,m_\chi^2,m_a^2)\\&\quad\quad+3m_a^2m_\chi^2\,D_0(m_\chi^2,m_\chi^2,0,0,0,m_\chi^2;m_a^2,m_\chi^2,m_a^2,0)\Big]\,\frac{m_q}{m_\chi}\,\bar{\chi}\chi\,\bar{q}q\Big\}\end{aligned}\tag{4.15}$$

which numerically yields

$$\frac{1}{(4\pi)^2}\frac{\xi^2\,y_q^2}{m_\chi^2}\left(C_{F_1}\,\bar{\chi}\gamma^\mu\chi\,\bar{q}\gamma_\mu q + C_{F_2}\,\frac{m_q}{m_\chi}\,\bar{\chi}\chi\,\bar{q}q\right), \tag{4.16}$$

with $C_{F_1} \approx 4.8$ and $C_{F_2} \approx 170$. The magnitudes of these coefficients can be understood as arising from the $\ln(m_a/m_\phi)$ and $\ln^2(m_a/m_\phi)$ behavior of C_0 and D_0 mentioned above. The loop-level cross section is then

$$\sigma_{\rm SI}^{\chi N} \approx (3\times 10^{-56}\ {\rm cm}^2)\left(\frac{\xi}{0.1}\right)^4\left(\frac{100\ {\rm GeV}}{m_\chi}\right)^4. \tag{4.17}$$

We will confirm below in the explicit model of Sec. 4.4 that the loop induced coupling is indeed tiny, but it is simple to see here why this is generically so.

Unlike in the massive mediator cases, there are two mass scales in the dark sector, that of the DM itself and that of the mediator. At tree level, the lighter mediator mass is the one that appears in the denominator of the operator. However, at loop level, the value of the loop integral is parametrically controlled by the mass of the DM, the heaviest particle in the loop. Additionally, a pseudoscalar which is the Nambu–Goldstone boson of a broken symmetry would be expected to couple to quarks proportional to the masses of the quarks. Thus, at loop level, the effective operator would be expected to be suppressed by extra factors of quark Yukawa couplings. Together, both effects combine to make the loop-level coupling to be as many as 20 orders smaller than the tree level one, with higher order corrections to the non-relativistic scattering approximation coming at similar orders as q^2v^4, so that the SI induced interaction is expected to be completely negligible.

4.4 The Axion Portal

We have just seen that without tuning of couplings, models with light pseudoscalar mediators provide the unique method of avoiding any SI signal, while still producing a SD direct detection signature. Now we turn to the question of whether a viable model producing DM with the correct abundance can have these features.

Coupling a light pseudoscalar to quarks is most efficiently achieved by adding a scalar field which spontaneously breaks a global symmetry, and which, by mixing with the Higgs, gets a coupling to the SM. Allowing this scalar to have a new global charge, while adding new fermions charged under the same symmetry, ensures that the new scalar field is the only method for the new fermions to interact with the SM.

As a simple realization of such a mechanism, where the dominant interaction is $\mathcal{O}_4^f$ via a pseudoscalar interaction, we introduce, following Ref. [30], a scalar field charged under a new global $U(1)_X$ charge that is spontaneously broken to

$$S = \left(f_a + \frac{s}{\sqrt{2}}\right)\exp\left(\frac{ia}{\sqrt{2}f_a}\right). \tag{4.18}$$

This scalar field is coupled to a new fermion, which is vector-like under the SM, through $\mathcal{L} = -\xi S \chi \chi^c + \text{h.c.}$, so that after the scalar field acquires a vacuum expectation value, the fermion receives a mass of $m_\chi = \xi f_a$, allowing it to act as dark matter, with stability ensured by the remnant of $U(1)_X$ after breaking.

In order for the pseudoscalar to interact with the SM, some known particles must also carry charges under the new $U(1)_X$. In a two Higgs doublet model, this can be accomplished by adding a term of the form

$$\mathcal{L} = \lambda S^n H_u H_d + \text{h.c.}, \tag{4.19}$$

by assigning the appropriate charges to the Higgses and SM fermions, and promoting the $U(1)_X$ to a Peccei-Quinn (PQ) symmetry. For $n = 2$, this coupling is of the same form as in the case of the DFSZ axion [83, 84], while the $n = 1$ case functions like that of the PQ-symmetric limit of the next-to-minimal supersymmetric standard model [97] We now have a dark matter candidate coupling to the SM though a massive scalar and an axionlike Nambu–Goldstone boson. The Nambu–Goldstone boson is assumed to get a small mass through an unspecified mechanism. Anticipating making the scalar heavy, by virtue of

$$\langle \sigma v \rangle_{\chi\chi^c \to sa} = \frac{m_\chi^2}{64\pi f_a^4} \left(1 - \frac{m_s^2}{4m_\chi^2}\right) + O(v^4)\,, \tag{4.20}$$

a choice of, say, $m_s = f_a = 1$ TeV and $m_\chi = 1.1$ TeV (corresponding to $\xi = 1.1$) yields a cross section of 3×10^{-26} cm^3/s and so generates the correct order of magnitude for the relic abundance [30].

For direct detection, two channels present themselves. The scalar gives a SI cross section through the operator $\mathcal{O}_1^f$, due to mixing of the scalar with the two CP-even Higgses, while the light axionlike state yields a SD interaction, $\mathcal{O}_4^f$, by a similar mixing with the CP-odd Higgs. For our purposes, we need check whether this tree-level SI cross section can be small enough to be completely negligible.

The mixing of the scalar with the two CP-even Higgs has a lot of arbitrariness to it due to the 11 constants in the most general $U(1)_{\text{PQ}}$-preserving two-Higgs-doublet and one-singlet potential. However, we can say that barring accidental cancellations, this mixing will be $\epsilon = O(v_{\text{ew}}/f_a)$, so that we may write the tree-level SI cross section as

$$\sigma_{\text{SI}}^{\chi N} \approx (2 \times 10^{-42}\ \text{cm}^2)\, \xi^2\, \epsilon^2 \left(\frac{100\ \text{GeV}}{m_s}\right)^4 , \tag{4.21}$$

(See App. C.1 for a caveat on the values of the nuclear matrix elements in this calculation.) In the model considered in Ref. [30], m_s needed to be light, $O(10\ \text{GeV})$, in order to provide a mechanism for Sommerfeld enhancement to explain astrophysical anomalies. In that case, the direct detection cross section was in tension with the SI bound and could only be slightly beyond current limits, at a few × 10^{-43} cm^2. However, if we impose no such condition, m_s could be larger. If it is at the electroweak scale, then the cross section is at most a few × 10^{-45} cm^2, smaller than the sensitivity of the next generation of direct detection experiments. If $m_s \sim O(1\text{ TeV})$, a reasonable choice given the scale of f_a in this setup, then the cross section becomes undetectably small, below the irreducible atmospheric neutrino limit.

Let us next consider the pseudoscalar channel. With the interaction kinetically suppressed by the momentum transfer as q^4, we cannot merely compute the cross section in the limit of $q^2 \to 0$ as we did in the scalar exchange case. Instead, we must define a cross section at a fixed momentum transfer. (See App. C.2 for a more thorough discussion.) We choose to do so at $q^2_{\rm ref} = (100\text{ MeV})^2$. Because the signal is different from that of unsuppressed interactions relative to the expected recoil energies, the sensitivities of experiments are modified. This was studied in Ref. [140], with the result that at the same reference momentum transfer, optimal sensitivities of SD experiments to pseudoscalars remained at the same order of magnitude as in the unsuppressed case, but with $1/m_{\rm DM}$ scaling of the limits.

With this definition, we can compute the SD cross section for $q^2 = q^2_{\rm ref}$ as

$$\sigma^{\chi p}_{\rm SD} \approx (2\times 10^{-37}\text{ cm}^2)\,\xi^2 \sin^2\theta\,\frac{q^2_{\rm ref}}{4m_\chi^2}\left(\frac{1\text{ GeV}}{m_a}\right)^4, \tag{4.22}$$

where $\tan\theta = n\sin 2\beta\,[v_{\rm ew}/(2f_a)]$ is the mixing of the s with the Higgses [74]. From this we see that given a DM mass $m_\chi = 1.1$ TeV, a pseudoscalar with a mass $m_a \approx 300$ MeV generates a cross section of 3×10^{-40} cm^2, within the range of the next generation of direct SD detection experiments. In fact, in a two Higgs doublet model like this, the nuclear matrix element also has a dependence on β as up-type quarks couple with a coefficient proportional to $\cot\beta$, while down type ones couple proportional to $\tan\beta$. We have evaluated the matrix elements for the above cross section at $\tan\beta = 1$. At large values of $\tan\beta$ the cross section can rise by almost 2 orders of magnitude.

Given the tiny size of the tree-level SI cross section, and in keeping with the discussion of the previous section, we should confirm that the loop-induced couplings fail to produce a detectable SI cross section. The calculation mostly mirrors that of Sec. 4.3.3. The only substantial difference is the aforementioned different coupling to up and down type quarks. As before, we evaluate the nuclear matrix elements at $\tan\beta = 1$, but this time, varying $\tan\beta$ cannot only modify the cross section by a factor of $O(1)$ as the suppression of $\sin^2\theta$ at high $\tan\beta$ is too strong, so we find

$$\sigma^{\chi N}_{\rm SI} \approx (3\times 10^{-56}\text{ cm}^2)\left(\frac{\xi\,\sin\theta}{0.1}\right)^4\left(\frac{100\text{ GeV}}{m_\chi}\right)^4 \tag{4.23}$$

with no additional implicit $\tan\beta$ dependence.

4.5 Conclusions

As the sensitivity of both SI and SD direct DM detection experiments increases, it is worth asking to what extent the discovery potential of the two methods is complementary.

In this work we have pointed out that when one considers the full range of possible mediators, instead of being confined to new weak-scale particles, the range of possible viable interactions generating SD cross sections increases. At the same time, when one searches for interactions for which SD experiments are complimentary for discovery—ones which could not be seen in any SI experiments without the need for accidental cancellations or other tuning—it becomes necessary to take into account subleading contributions to scattering, such as suppressed operators and loop processes. The outcome is that the traditional models considered also generically produce SI interactions whose suppression is counterbalanced by the greater sensitivity of SI experiments. The list of viable candidates whose interaction with the SM can be described by tree-level mediators integrated out in a renormalizable model is then reduced to merely ones mediated by light pseudoscalars.

We have presented a realistic model of such interactions that generates the right DM abundance with a fermionic DM candidate without having other interactions generating detectable SI interactions.

Similar scenarios can also be considered with a scalar or vector dark matter candidate. Just as in the case of fermionic DM, $\mathcal{O}_1^{s,v}$ gives the leading interaction in the nonrelativistic limit, while $\mathcal{O}_2^{s,v}$ is kinematically suppressed. The necessary couplings between the pseudoscalar and the scalars or vectors cannot be generated in as simple a manner as those used above, so more model building will be required. However, the suppression is only by q^2, so the mass differences between the scalar and pseudoscalar do not have to be quite as large, and the couplings themselves can be smaller, so that the parameter space of couplings and the pseudoscalar mass are not as tightly limited by experiment, potentially making the exercise worthwhile.

Chapter 5

Summary and Outlook

In this dissertation, I considered several different plans of attack for the detection of either dark matter itself or light states present in the dark sector of a number of models proposed in the last several years. Together the different observations considered provide broad coverage of the available theory space.

I argued that an X boson with $\alpha_X \sim 10^{-8}$ and 10 MeV $< m_X <$ 100 MeV could be discovered in a low-energy, high-intensity ep scattering experiment with around 1 ab^{-1} of data assuming 1 MeV invariant mass resolution. Since the search for $X \to e^+e^-$ is background limited, it is crucial to have an experiment with good energy resolution and very high statistics. In fact, an experiment following these lines has been approved, and the DarkLight collaboration is currently in the midst of implementing a search at the Jefferson Lab free electron laser facility [146]. Such a search is complementary to the beam dump experiments envisioned in Refs. [43, 50], which are better suited for smaller value of α_X and larger values of m_X, and have also lead to active experimental efforts of their own.

To detect light states which the experimental efforts above miss, I looked at the utility of flavor-changing neutral current $b \to s$ decays to place bounds on axion-like states. I found that the exclusive $B \to K\ell^+\ell^-$ decay is particularly well-suited to constrain such contributions. In the case of the axion portal (or equivalently, any DFSZ-type axion), I derived a bound from current B-factory data on the axion decay constant f_a. The bound is in the multi-TeV range, gets stronger for small $\tan\beta$, and depends sensitively on the value of the charged Higgs boson mass, making it complementary to $\Upsilon(nS) \to \gamma a$ searches performed by BaBar [96]. This places tension on the axion portal model of dark matter in the parameter space given in Eq. (3.1). Such a bound has more general applicability as well, as there is a constraint on any pseudoscalar with $2m_\mu < m_a < m_B - m_K$ whose couplings to standard model fermions arise via mixing with the CP-odd Higgs A^0. Since the derivation of out bounds, analyses of $B \to K\ell^+\ell^-$ with larger datasets have been performed [147], but resonances in the lepton spectrum or hadronic final states have not yet been considered, still leaving the possibility of improvement.

As an alternative set of considerations which lead one to consider light axion-light states, I pointed out that when considering the full range of possible mediators, instead of being confined to new weak-scale particles, new classes of interactions that could lead to signals in spin-dependent dark matter detection experiments appear. The requirement that so signal is also observed in spin-independent experiments on similar timescales lead me to consider loop- and kinematically-suppressed contributions, and uniquely points to a light axion-light state coupling the DM to the standard model. In this way, the observation of a DM signal solely in spin-dependent scattering experiments would lead to a much more precise identification of the nature of dark matter interactions than was previously realized.

Bibliography

[1] F. Zwicky, "Die Rotverschiebung von extragalaktischen Nebeln," *Helv.Phys.Acta* **6** (1933) 110–127.

[2] H. Babcock, "The rotation of the Andromeda Nebula," *Lick Observatory Bulletin* **19** (1939) 41–51.

[3] V. C. Rubin, "One Hundred Years of Rotating Galaxies," *Publ.Astron.Soc.Pac.* **112** no. 772, (2000) 747–750. `http://www.jstor.org/stable/10.1086/316573`.

[4] J. Ostriker and P. Peebles, "A Numberical Study of Flattened Galaxies: or, can Cold Galaxies Survive?," *Astrophys.J.* **186** (Dec, 1973) 467–480.

[5] V. C. Rubin and W. K. Ford, Jr., "Rotation of the Andromeda Nebula from a Spectroscopic Survey of Emission Regions," *Astrophys.J.* **159** (1970) 379–403.

[6] D. Fabricant, M. Lecar, and P. Gorenstein, "X-ray measurements of the mass of M87," *Astrophys.J.* **241** (Oct, 1980) 552–560.

[7] R. Massey, T. Kitching, and J. Richard, "The dark matter of gravitational lensing," *Rept.Prog.Phys.* **73** (2010) 086901, `arXiv:1001.1739 [astro-ph.CO]`.

[8] D. Clowe, M. Bradac, A. H. Gonzalez, M. Markevitch, S. W. Randall, *et al.*, "A direct empirical proof of the existence of dark matter," *Astrophys.J.* **648** (2006) L109–L113, `arXiv:astro-ph/0608407 [astro-ph]`.

[9] **WMAP** Collaboration, E. Komatsu *et al.*, "Five-Year Wilkinson Microwave Anisotropy Probe (WMAP) Observations: Cosmological Interpretation," *Astrophys.J.Suppl.* **180** (2009) 330–376, `arXiv:0803.0547 [astro-ph]`.

[10] S. Sarkar, "Primordial nucleosynthesis and dark matter," `arXiv:astro-ph/9611232 [astro-ph]`.

[11] K. A. Olive, "Primordial nucleosynthesis and dark matter," `arXiv:astro-ph/9707212 [astro-ph]`.

[12] J. E. Carlstrom, G. P. Holder, and E. D. Reese, “Cosmology with the Sunyaev-Zel’dovich effect,” *Ann.Rev.Astron.Astrophys.* **40** (2002) 643–680, `arXiv:astro-ph/0208192 [astro-ph]`.

[13] D. H. Weinberg, R. Davé, N. Katz, and J. A. Kollmeier, “The Lyman-α forest as a cosmological tool,” *AIP Conf.Proc.* **666** (2003) 157–169, `arXiv:astro-ph/0301186 [astro-ph]`.

[14] G. R. Blumenthal, S. Faber, J. R. Primack, and M. J. Rees, “Formation of Galaxies and Large Scale Structure with Cold Dark Matter,” *Nature* **311** (1984) 517–525.

[15] J. R. Primack, “Dark matter and structure formation,” `arXiv:astro-ph/9707285 [astro-ph]`. 102 pgs. Published as Chapter 1 of Formation of Structure in the Universe, Proceedings of the Jerusalem Winter School 1996, edited by A. Dekel and J.P. Ostriker (Cambridge University Press).

[16] G. Bertone, D. Hooper, and J. Silk, “Particle dark matter: Evidence, candidates and constraints,” *Phys.Rept.* **405** (2005) 279–390, `arXiv:hep-ph/0404175 [hep-ph]`.

[17] J. L. Feng, “Dark Matter Candidates from Particle Physics and Methods of Detection,” *Ann.Rev.Astron.Astrophys.* **48** (2010) 495, `arXiv:1003.0904 [astro-ph.CO]`.

[18] J. R. Ellis, J. Hagelin, D. V. Nanopoulos, K. A. Olive, and M. Srednicki, “Supersymmetric Relics from the Big Bang,” *Nucl.Phys.* **B238** (1984) 453–476.

[19] D. P. Finkbeiner, “WMAP microwave emission interpreted as dark matter annihilation in the inner galaxy,” `arXiv:astro-ph/0409027 [astro-ph]`.

[20] D. Hooper, D. P. Finkbeiner, and G. Dobler, “Possible evidence for dark matter annihilations from the excess microwave emission around the center of the Galaxy seen by the Wilkinson Microwave Anisotropy Probe,” *Phys.Rev.* **D76** (2007) 083012, `arXiv:0705.3655 [astro-ph]`.

[21] **PAMELA** Collaboration, O. Adriani *et al.*, “An anomalous positron abundance in cosmic rays with energies 1.5-100 GeV,” *Nature* **458** (2009) 607–609, `arXiv:0810.4995 [astro-ph]`.

[22] **The Fermi LAT** Collaboration, A. A. Abdo *et al.*, “Measurement of the Cosmic Ray $e^+ + e^-$ spectrum from 20 GeV to 1 TeV with the Fermi Large Area Telescope,” *Phys.Rev.Lett.* **102** (2009) 181101, `arXiv:0905.0025 [astro-ph.HE]`.

[23] **H.E.S.S.** Collaboration, F. Aharonian *et al.*, “The energy spectrum of cosmic-ray electrons at TeV energies,” *Phys.Rev.Lett.* **101** (2008) 261104, `arXiv:0811.3894 [astro-ph]`.

[24] **H.E.S.S.** Collaboration, F. Aharonian *et al.*, “Probing the ATIC peak in the cosmic-ray electron spectrum with H.E.S.S,” *Astron.Astrophys.* **508** (2009) 561, `arXiv:0905.0105 [astro-ph.HE]`.

[25] G. Weidenspointner, C. Shrader, J. Knoedlseder, P. Jean, V. Lonjou, *et al.*, “The sky distribution of positronium annihilation continuum emission measured with SPI/INTEGRAL,” *Astron.Astrophys.* **450** (2006) 1013–1021, `arXiv:astro-ph/0601673 [astro-ph]`.

[26] J. Knodlseder, V. Lonjou, P. Jean, M. Allain, P. Mandrou, *et al.*, “Early SPI / INTEGRAL contraints on the morphology of the 511 keV line emission in the 4th galactic quadrant,” *Astron.Astrophys.* **411** (2003) L457–L460, `arXiv:astro-ph/0309442 [astro-ph]`.

[27] D. P. Finkbeiner and N. Weiner, “Exciting Dark Matter and the INTEGRAL/SPI 511 keV signal,” *Phys.Rev.* **D76** (2007) 083519, `arXiv:astro-ph/0702587 [astro-ph]`.

[28] M. Pospelov, A. Ritz, and M. B. Voloshin, “Secluded WIMP Dark Matter,” *Phys.Lett.* **B662** (2008) 53–61, `arXiv:0711.4866 [hep-ph]`.

[29] N. Arkani-Hamed, D. P. Finkbeiner, T. R. Slatyer, and N. Weiner, “A Theory of Dark Matter,” *Phys.Rev.* **D79** (2009) 015014, `arXiv:0810.0713 [hep-ph]`.

[30] Y. Nomura and J. Thaler, “Dark Matter through the Axion Portal,” *Phys.Rev.* **D79** (2009) 075008, `arXiv:0810.5397 [hep-ph]`.

[31] P. Candelas, G. T. Horowitz, A. Strominger, and E. Witten, “Vacuum Configurations for Superstrings,” *Nucl.Phys.* **B258** (1985) 46–74.

[32] M. Goodsell and A. Ringwald, “Light Hidden-Sector U(1)s in String Compactifications,” *Fortsch.Phys.* **58** (2010) 716–720, `arXiv:1002.1840 [hep-th]`.

[33] P. Fayet, “U-boson production in e^+e^- annihilations, ψ and Υ decays, and Light Dark Matter,” *Phys.Rev.* **D75** (2007) 115017, `arXiv:hep-ph/0702176 [hep-ph]`.

[34] N. Arkani-Hamed and N. Weiner, “LHC Signals for a SuperUnified Theory of Dark Matter,” *JHEP* **0812** (2008) 104, `arXiv:0810.0714 [hep-ph]`.

[35] C. Cheung, J. T. Ruderman, L.-T. Wang, and I. Yavin, “Kinetic Mixing as the Origin of Light Dark Scales,” *Phys.Rev.* **D80** (2009) 035008, `arXiv:0902.3246 [hep-ph]`.

[36] D. E. Morrissey, D. Poland, and K. M. Zurek, “Abelian Hidden Sectors at a GeV,” *JHEP* **0907** (2009) 050, `arXiv:0904.2567 [hep-ph]`.

[37] M. Freytsis, G. Ovanesyan, and J. Thaler, “Dark Force Detection in Low Energy e-p Collisions,” *JHEP* **1001** (2010) 111, `arXiv:0909.2862 [hep-ph]`.

[38] **SDSS** Collaboration, J. K. Adelman-McCarthy *et al.*, “The Fourth Data Release of the Sloan Digital Sky Survey,” *Astrophys.J.Suppl.* **162** (2006) 38–48, `arXiv:astro-ph/0507711 [astro-ph]`.

[39] U. G. Briel and J. P. Henry, “An x-ray temperature map of coma,” `arXiv:astro-ph/9711237 [astro-ph]`.

[40] M. Goodsell, J. Jaeckel, J. Redondo, and A. Ringwald, “Naturally Light Hidden Photons in LARGE Volume String Compactifications,” *JHEP* **0911** (2009) 027, `arXiv:0909.0515 [hep-ph]`.

[41] M. Pospelov, “Secluded U(1) below the weak scale,” *Phys.Rev.* **D80** (2009) 095002, `arXiv:0811.1030 [hep-ph]`.

[42] Y. Kahn, M. Schmitt, and T. M. Tait, “Enhanced rare pion decays from a model of MeV dark matter,” *Phys.Rev.* **D78** (2008) 115002, `arXiv:0712.0007 [hep-ph]`.

[43] M. Reece and L.-T. Wang, “Searching for the light dark gauge boson in GeV-scale experiments,” *JHEP* **0907** (2009) 051, `arXiv:0904.1743 [hep-ph]`.

[44] N. Borodatchenkova, D. Choudhury, and M. Drees, “Probing MeV dark matter at low-energy e+e- colliders,” *Phys.Rev.Lett.* **96** (2006) 141802, `arXiv:hep-ph/0510147 [hep-ph]`.

[45] B. Batell, M. Pospelov, and A. Ritz, “Probing a Secluded U(1) at B-factories,” *Phys.Rev.* **D79** (2009) 115008, `arXiv:0903.0363 [hep-ph]`.

[46] R. Essig, P. Schuster, and N. Toro, “Probing Dark Forces and Light Hidden Sectors at Low-Energy e+e- Colliders,” *Phys.Rev.* **D80** (2009) 015003, `arXiv:0903.3941 [hep-ph]`.

[47] P.-f. Yin, J. Liu, and S.-h. Zhu, “Detecting light leptophilic gauge boson at BESIII detector,” *Phys.Lett.* **B679** (2009) 362–368, `arXiv:0904.4644 [hep-ph]`.

[48] E. Riordan, M. Krasny, K. Lang, P. De Barbaro, A. Bodek, *et al.*, “A SEARCH FOR SHORT LIVED AXIONS IN AN ELECTRON BEAM DUMP EXPERIMENT,” *Phys.Rev.Lett.* **59** (1987) 755.

[49] A. Bross, M. Crisler, S. H. Pordes, J. Volk, S. Errede, *et al.*, “A Search for Shortlived Particles Produced in an Electron Beam Dump,” *Phys.Rev.Lett.* **67** (1991) 2942–2945.

[50] J. D. Bjorken, R. Essig, P. Schuster, and N. Toro, “New Fixed-Target Experiments to Search for Dark Gauge Forces,” *Phys.Rev.* **D80** (2009) 075018, `arXiv:0906.0580 [hep-ph]`.

[51] S. Heinemeyer, Y. Kahn, M. Schmitt, and M. Velasco, “An Experiment to search for light dark matter in low-energy *ep* scattering,” `arXiv:0705.4056 [hep-ex]`.

[52] C. Boehm and P. Fayet, “Scalar dark matter candidates,” *Nucl.Phys.* **B683** (2004) 219–263, `arXiv:hep-ph/0305261 [hep-ph]`.

[53] B. Wojtsekhowski, “Searching for a U-boson with a positron beam,” *AIP Conf.Proc.* **1160** (2009) 149–154, `arXiv:0906.5265 [hep-ex]`.

[54] M. Baumgart, C. Cheung, J. T. Ruderman, L.-T. Wang, and I. Yavin, “Non-Abelian Dark Sectors and Their Collider Signatures,” *JHEP* **0904** (2009) 014, `arXiv:0901.0283 [hep-ph]`.

[55] R. Milner. Private communication, 2009.

[56] G. Neil, C. Behre, S. Benson, M. Bevins, G. Biallas, *et al.*, “The JLab high power ERL light source,” *Nucl.Instrum.Meth.* **A557** (2006) 9–15.

[57] **Particle Data Group** Collaboration, C. Amsler *et al.*, “Review of Particle Physics,” *Phys.Lett.* **B667** (2008) 1–1340.

[58] R. Sinha, “Anomalous Magnetic Moment of Electron and Constraint on Composite Bosons of Weak Interaction,” *Phys.Rev.* **D34** (1986) 1509.

[59] J. P. Leveille, “The Second Order Weak Correction to (g-2) of the Muon in Arbitrary Gauge Models,” *Nucl.Phys.* **B137** (1978) 63.

[60] **BaBar** Collaboration, B. Aubert *et al.*, “Search for Dimuon Decays of a Light Scalar in Radiative Transitions $\Upsilon(3S) \to \gamma A^0$,” `arXiv:0902.2176 [hep-ex]`. submitted to Aspen-2009.

[61] **BaBar** Collaboration, B. Aubert *et al.*, “Search for a Narrow Resonance in e^+e^- to Four Lepton Final States,” `arXiv:0908.2821 [hep-ex]`. submitted to Lepton-Photon 2009.

[62] **CHARM** Collaboration, F. Bergsma *et al.*, “Search for axion-like particle production in 400-GeV proton-copper interactions,” *Phys.Lett.* **B157** (1985) 458.

[63] B. Batell, M. Pospelov, and A. Ritz, “Exploring Portals to a Hidden Sector Through Fixed Targets,” *Phys.Rev.* **D80** (2009) 095024, `arXiv:0906.5614 [hep-ph]`.

[64] M. S. Turner, “Axions from SN 1987a,” *Phys.Rev.Lett.* **60** (1988) 1797.

[65] **KTeV** Collaboration, E. Abouzaid *et al.*, “Measurement of the rare decay $pi^0 \to e^+e^-$,” *Phys.Rev.* **D75** (2007) 012004, `arXiv:hep-ex/0610072 [hep-ex]`.

[66] E. Boos, V. Bunichev, M. Dubinin, L. Dudko, V. Edneral, *et al.*, “CompHEP 4.5 Status Report,” *PoS* **ACAT08** (2008) 008, `arXiv:0901.4757 [hep-ph]`.

[67] J. Alwall, P. Demin, S. de Visscher, R. Frederix, M. Herquet, *et al.*, “MadGraph/MadEvent v4: The New Web Generation,” *JHEP* **0709** (2007) 028, `arXiv:0706.2334 [hep-ph]`.

[68] P. Fisher. Private communication, 2009.

[69] **CDF** Collaboration, A. Abulencia *et al.*, “Top quark mass measurement from dilepton events at CDF II,” *Phys.Rev.Lett.* **96** (2006) 152002, `arXiv:hep-ex/0512070 [hep-ex]`.

[70] **D0** Collaboration, V. Abazov *et al.*, “A precision measurement of the mass of the top quark,” *Nature* **429** (2004) 638–642, `arXiv:hep-ex/0406031 [hep-ex]`.

[71] **D0** Collaboration, V. Abazov *et al.*, “Measurement of the top quark mass in the lepton+jets final state with the matrix element method,” *Phys.Rev.* **D74** (2006) 092005, `arXiv:hep-ex/0609053 [hep-ex]`.

[72] Y. G. Kolomensky. Private communication, 2009.

[73] J. Bjorken, S. Ecklund, W. Nelson, A. Abashian, C. Church, *et al.*, “Search for Neutral Metastable Penetrating Particles Produced in the SLAC Beam Dump,” *Phys.Rev.* **D38** (1988) 3375.

[74] M. Freytsis, Z. Ligeti, and J. Thaler, “Constraining the Axion Portal with $B \to K\ell^+\ell^-$,” *Phys.Rev.* **D81** (2010) 034001, `arXiv:0911.5355 [hep-ph]`.

[75] M. Ibe, Y. Nakayama, H. Murayama, and T. T. Yanagida, “Nambu-Goldstone Dark Matter and Cosmic Ray Electron and Positron Excess,” *JHEP* **0904** (2009) 087, `arXiv:0902.2914 [hep-ph]`.

[76] Y. Bai, M. Carena, and J. Lykken, “The PAMELA excess from neutralino annihilation in the NMSSM,” *Phys.Rev.* **D80** (2009) 055004, `arXiv:0905.2964 [hep-ph]`.

[77] J. Mardon, Y. Nomura, and J. Thaler, “Cosmic Signals from the Hidden Sector,” *Phys.Rev.* **D80** (2009) 035013, `arXiv:0905.3749 [hep-ph]`.

[78] D. Hooper and T. M. Tait, “Neutralinos in an extension of the minimal supersymmetric standard model as the source of the PAMELA positron excess,” *Phys.Rev.* **D80** (2009) 055028, `arXiv:0906.0362 [hep-ph]`.

[79] M. Ibe, H. Murayama, S. Shirai, and T. T. Yanagida, “Cosmic Ray Spectra in Nambu-Goldstone Dark Matter Models,” *JHEP* **0911** (2009) 120, `arXiv:0908.3530 [hep-ph]`.

[80] R. Peccei and H. R. Quinn, "CP Conservation in the Presence of Instantons," *Phys.Rev.Lett.* **38** (1977) 1440–1443.

[81] S. Weinberg, "A New Light Boson?," *Phys.Rev.Lett.* **40** (1978) 223–226.

[82] F. Wilczek, "Problem of Strong p and t Invariance in the Presence of Instantons," *Phys.Rev.Lett.* **40** (1978) 279–282.

[83] M. Dine, W. Fischler, and M. Srednicki, "A Simple Solution to the Strong CP Problem with a Harmless Axion," *Phys.Lett.* **B104** (1981) 199.

[84] A. Zhitnitsky, "On Possible Suppression of the Axion Hadron Interactions. (In Russian)," *Sov.J.Nucl.Phys.* **31** (1980) 260.

[85] J. E. Kim, "Weak Interaction Singlet and Strong CP Invariance," *Phys.Rev.Lett.* **43** (1979) 103.

[86] M. A. Shifman, A. Vainshtein, and V. I. Zakharov, "Can Confinement Ensure Natural CP Invariance of Strong Interactions?," *Nucl.Phys.* **B166** (1980) 493.

[87] A. E. Nelson and N. Seiberg, "R symmetry breaking versus supersymmetry breaking," *Nucl.Phys.* **B416** (1994) 46–62, `arXiv:hep-ph/9309299 [hep-ph]`.

[88] X.-G. He, J. Tandean, and G. Valencia, "Light Higgs production in hyperon decay," *Phys.Rev.* **D74** (2006) 115015, `arXiv:hep-ph/0610274 [hep-ph]`.

[89] **HyperCP** Collaboration, H. Park *et al.*, "Evidence for the decay $\Sigma^+ \to p\mu^+\mu^-$," *Phys.Rev.Lett.* **94** (2005) 021801, `arXiv:hep-ex/0501014 [hep-ex]`.

[90] M. B. Wise, "Radiately Induced Flavor Changing Neutral Higgs Boson Couplings," *Phys.Lett.* **B103** (1981) 121.

[91] L. J. Hall and M. B. Wise, "Flavor Changing Higgs-Boson Couplings," *Nucl.Phys.* **B187** (1981) 397.

[92] J. Frere, J. Vermaseren, and M. Gavela, "The Elusive Axion," *Phys.Lett.* **B103** (1981) 129–133.

[93] R. Dermisek and J. F. Gunion, "Escaping the large fine tuning and little hierarchy problems in the next to minimal supersymmetric model and $h \to aa$ decays," *Phys.Rev.Lett.* **95** (2005) 041801, `arXiv:hep-ph/0502105 [hep-ph]`.

[94] S. Chang, R. Dermisek, J. F. Gunion, and N. Weiner, "Nonstandard Higgs Boson Decays," *Ann.Rev.Nucl.Part.Sci.* **58** (2008) 75–98, `arXiv:0801.4554 [hep-ph]`.

[95] R. Dermisek and J. F. Gunion, "Many Light Higgs Bosons in the NMSSM," *Phys.Rev.* **D79** (2009) 055014, `arXiv:0811.3537 [hep-ph]`.

[96] **BaBar** Collaboration, B. Aubert *et al.*, "Search for Dimuon Decays of a Light Scalar Boson in Radiative Transitions $\Upsilon \to \gamma A^0$," *Phys.Rev.Lett.* **103** (2009) 081803, `arXiv:0905.4539 [hep-ex]`.

[97] L. J. Hall and T. Watari, "Electroweak supersymmetry with an approximate $U(1)_{(PQ)}$," *Phys.Rev.* **D70** (2004) 115001, `arXiv:hep-ph/0405109 [hep-ph]`.

[98] **E949** Collaboration, V. Anisimovsky *et al.*, "Improved measurement of the $K^+ \to \pi^+ \nu \bar{\nu}$ branching ratio," *Phys.Rev.Lett.* **93** (2004) 031801, `arXiv:hep-ex/0403036 [hep-ex]`.

[99] **E787** Collaboration, S. Adler *et al.*, "Further evidence for the decay $K^+ \to \pi^+ \nu \bar{\nu}$," *Phys.Rev.Lett.* **88** (2002) 041803, `arXiv:hep-ex/0111091 [hep-ex]`.

[100] M. Lisanti and J. G. Wacker, "Discovering the Higgs with Low Mass Muon Pairs," *Phys.Rev.* **D79** (2009) 115006, `arXiv:0903.1377 [hep-ph]`.

[101] A. Ali, P. Ball, L. Handoko, and G. Hiller, "A Comparative study of the decays $B \to (K,\, K^*)\ell^+\ell^-$ in standard model and supersymmetric theories," *Phys.Rev.* **D61** (2000) 074024, `arXiv:hep-ph/9910221 [hep-ph]`.

[102] G. Hiller, "B physics signals of the lightest CP odd Higgs in the NMSSM at large tan β," *Phys.Rev.* **D70** (2004) 034018, `arXiv:hep-ph/0404220 [hep-ph]`.

[103] **Belle** Collaboration, I. Adachi *et al.*, "Measurement of the Differential Branching Fraction and Forward-Backward Asymmetry for $B \to K^{(*)}\ell^+\ell^-$," `arXiv:0810.0335 [hep-ex]`.

[104] **Belle** Collaboration, J.-T. Wei *et al.*, "Measurement of the Differential Branching Fraction and Forward-Backword Asymmetry for $B \to K^{(*)}\ell^+\ell^-$," *Phys.Rev.Lett.* **103** (2009) 171801, `arXiv:0904.0770 [hep-ex]`.

[105] **BaBar** Collaboration, B. Aubert *et al.*, "Direct CP, Lepton Flavor and Isospin Asymmetries in the Decays $B \to K^{(*)}\ell^+\ell^-$," *Phys.Rev.Lett.* **102** (2009) 091803, `arXiv:0807.4119 [hep-ex]`.

[106] **Heavy Flavor Averaging Group** Collaboration, E. Barberio *et al.*, "Averages of $b-$hadron and $c-$hadron Properties at the End of 2007," `arXiv:0808.1297 [hep-ex]`. Updates at http://www.slac.stanford.edu/xorg/hfag/.

[107] U. Uwer. Private communication, 2009.

[108] P. Ball and R. Zwicky, "New results on $B \to \pi, K, \eta$ decay formfactors from light-cone sum rules," *Phys.Rev.* **D71** (2005) 014015, `arXiv:hep-ph/0406232 [hep-ph]`.

[109] M. Bartsch, M. Beylich, G. Buchalla, and D.-N. Gao, "Precision Flavour Physics with $B \to K\nu\bar{\nu}$ and $B \to K\ell^+\ell^-$," *JHEP* **0911** (2009) 011, `arXiv:0909.1512 [hep-ph]`. Additionally references therein.

[110] B. Batell, M. Pospelov, and A. Ritz, "Multi-lepton Signatures of a Hidden Sector in Rare B Decays," *Phys.Rev.* **D83** (2011) 054005, `arXiv:0911.4938 [hep-ph]`.

[111] M. Freytsis and Z. Ligeti, "On dark matter models with uniquely spin-dependent detection possibilities," *Phys.Rev.* **D83** (2011) 115009, `arXiv:1012.5317 [hep-ph]`.

[112] G. Bertone, D. G. Cerdeno, J. Collar, and B. C. Odom, "WIMP identification through a combined measurement of axial and scalar couplings," *Phys.Rev.Lett.* **99** (2007) 151301, `arXiv:0705.2502 [astro-ph]`.

[113] V. Barger, W.-Y. Keung, and G. Shaughnessy, "Spin Dependence of Dark Matter Scattering," *Phys.Rev.* **D78** (2008) 056007, `arXiv:0806.1962 [hep-ph]`.

[114] G. Belanger, E. Nezri, and A. Pukhov, "Discriminating dark matter candidates using direct detection," *Phys.Rev.* **D79** (2009) 015008, `arXiv:0810.1362 [hep-ph]`.

[115] T. Cohen, D. J. Phalen, and A. Pierce, "On the Correlation Between the Spin-Independent and Spin-Dependent Direct Detection of Dark Matter," *Phys.Rev.* **D81** (2010) 116001, `arXiv:1001.3408 [hep-ph]`.

[116] P. Agrawal, Z. Chacko, C. Kilic, and R. K. Mishra, "A Classification of Dark Matter Candidates with Primarily Spin-Dependent Interactions with Matter," `arXiv:1003.1912 [hep-ph]`.

[117] J. Fan, M. Reece, and L.-T. Wang, "Non-relativistic effective theory of dark matter direct detection," *JCAP* **1011** (2010) 042, `arXiv:1008.1591 [hep-ph]`.

[118] **XENON** Collaboration, J. Angle *et al.*, "First Results from the XENON10 Dark Matter Experiment at the Gran Sasso National Laboratory," *Phys.Rev.Lett.* **100** (2008) 021303, `arXiv:0706.0039 [astro-ph]`.

[119] **The CDMS-II** Collaboration, Z. Ahmed *et al.*, "Dark Matter Search Results from the CDMS II Experiment," *Science* **327** (2010) 1619–1621, `arXiv:0912.3592 [astro-ph.CO]`.

[120] **XENON100 Collaboration** Collaboration, E. Aprile *et al.*, "Dark Matter Results from 100 Live Days of XENON100 Data," *Phys.Rev.Lett.* **107** (2011) 131302, `arXiv:1104.2549 [astro-ph.CO]`.

[121] B. Cabrera, L. M. Krauss, and F. Wilczek, "Bolometric Detection of Neutrinos," *Phys.Rev.Lett.* **55** (1985) 25.

[122] A. Drukier, K. Freese, and D. Spergel, “Detecting Cold Dark Matter Candidates,” *Phys.Rev.* **D33** (1986) 3495–3508.

[123] L. E. Strigari, “Neutrino Coherent Scattering Rates at Direct Dark Matter Detectors,” *New J.Phys.* **11** (2009) 105011, `arXiv:0903.3630 [astro-ph.CO]`.

[124] M. Felizardo, T. Girard, T. Morlat, A. Fernandes, F. Giuliani, *et al.*, “Final Analysis and Results of the Phase II SIMPLE Dark Matter Search,” `arXiv:1106.3014 [astro-ph.CO]`.

[125] E. Behnke, J. Behnke, S. Brice, D. Broemmelsiek, J. Collar, *et al.*, “Improved Limits on Spin-Dependent WIMP-Proton Interactions from a Two Liter CF_3I Bubble Chamber,” *Phys.Rev.Lett.* **106** (2011) 021303, `arXiv:1008.3518 [astro-ph.CO]`.

[126] **KIMS** Collaboration, H. Lee *et al.*, “Limits on WIMP-nucleon cross section with CsI(Tl) crystal detectors,” *Phys.Rev.Lett.* **99** (2007) 091301, `arXiv:0704.0423 [astro-ph]`.

[127] S. Archambault, F. Aubin, M. Auger, E. Behnke, B. Beltran, *et al.*, “Dark Matter Spin-Dependent Limits for WIMP Interactions on ^{19}F by PICASSO,” *Phys.Lett.* **B682** (2009) 185–192, `arXiv:0907.0307 [hep-ex]`.

[128] J. Angle, E. Aprile, F. Arneodo, L. Baudis, A. Bernstein, *et al.*, “Limits on spin-dependent WIMP-nucleon cross-sections from the XENON10 experiment,” *Phys.Rev.Lett.* **101** (2008) 091301, `arXiv:0805.2939 [astro-ph]`.

[129] **COUPP** Collaboration, E. Behnke *et al.*, “Improved Spin-Dependent WIMP Limits from a Bubble Chamber,” *Science* **319** (2008) 933–936, `arXiv:0804.2886 [astro-ph]`.

[130] **PICASSO** Collaboration, M. Barnabe-Heider *et al.*, “Improved spin dependent limits from the PICASSO dark matter search experiment,” *Phys.Lett.* **B624** (2005) 186–194, `arXiv:hep-ex/0502028 [hep-ex]`.

[131] **COUPP** Collaboration, E. Behnke *et al.*, “COUPP-500: A Proposal for a Ton-Scale Bubble Chamber for Dark Matter Detection.” Availible at http://www-coupp.fnal.gov/public/500kg PAC Proposal.pdf.

[132] **Super-Kamiokande** Collaboration, S. Desai *et al.*, “Search for dark matter WIMPs using upward through-going muons in Super-Kamiokande,” *Phys.Rev.* **D70** (2004) 083523, `arXiv:hep-ex/0404025 [hep-ex]`.

[133] **ICECUBE** Collaboration, R. Abbasi *et al.*, “Limits on a muon flux from neutralino annihilations in the Sun with the IceCube 22-string detector,” *Phys.Rev.Lett.* **102** (2009) 201302, `arXiv:0902.2460 [astro-ph.CO]`.

[134] J. Goodman, M. Ibe, A. Rajaraman, W. Shepherd, T. M. Tait, *et al.*, "Constraints on Light Majorana dark Matter from Colliders," *Phys.Lett.* **B695** (2011) 185–188, `arXiv:1005.1286 [hep-ph]`.

[135] J. Goodman, M. Ibe, A. Rajaraman, W. Shepherd, T. M. Tait, *et al.*, "Constraints on Dark Matter from Colliders," *Phys.Rev.* **D82** (2010) 116010, `arXiv:1008.1783 [hep-ph]`.

[136] Y. Bai, P. J. Fox, and R. Harnik, "The Tevatron at the Frontier of Dark Matter Direct Detection," *JHEP* **1012** (2010) 048, `arXiv:1005.3797 [hep-ph]`.

[137] A. Kurylov and M. Kamionkowski, "Generalized analysis of weakly interacting massive particle searches," *Phys.Rev.* **D69** (2004) 063503, `arXiv:hep-ph/0307185 [hep-ph]`.

[138] M. W. Goodman and E. Witten, "Detectability of Certain Dark Matter Candidates," *Phys.Rev.* **D31** (1985) 3059.

[139] I. Wasserman, "Possibility of Detecting Heavy Neutral Fermions in the Galaxy," *Phys.Rev.* **D33** (1986) 2071–2078.

[140] S. Chang, A. Pierce, and N. Weiner, "Momentum Dependent Dark Matter Scattering," *JCAP* **1001** (2010) 006, `arXiv:0908.3192 [hep-ph]`.

[141] R. Essig, "Direct Detection of Non-Chiral Dark Matter," *Phys.Rev.* **D78** (2008) 015004, `arXiv:0710.1668 [hep-ph]`.

[142] M. Cirelli, N. Fornengo, and A. Strumia, "Minimal dark matter," *Nucl.Phys.* **B753** (2006) 178–194, `arXiv:hep-ph/0512090 [hep-ph]`.

[143] M. Drees and M. Nojiri, "Neutralino-nucleon scattering revisited," *Phys.Rev.* **D48** (1993) 3483–3501, `arXiv:hep-ph/9307208 [hep-ph]`.

[144] G. Passarino and M. Veltman, "One Loop Corrections for e^+e^- Annihilation Into $\mu^+\mu^-$ in the Weinberg Model," *Nucl.Phys.* **B160** (1979) 151.

[145] R. Mertig, M. Bohm, and A. Denner, "FEYN CALC: Computer algebraic calculation of Feynman amplitudes," *Comput.Phys.Commun.* **64** (1991) 345–359.

[146] **DarkLight** Collaboration. `http://dmtpc.mit.edu/DarkLight/`.

[147] **BaBar** Collaboration, J. Lees *et al.*, "Measurement of Branching Fractions and Rate Asymmetries in the Rare Decays $B \to K^{(*)}\ell^+\ell^-$," `arXiv:1204.3933 [hep-ex]`.

[148] I. Bars and M. Yoshimura, "Muon magnetic moment in a finite theory of weak and electromagnetic interaction," *Phys.Rev.* **D6** (1972) 374–376.

[149] T. Donnelly, S. Freedman, R. Lytel, R. Peccei, and M. Schwartz, “Do Axions Exist?,” *Phys.Rev.* **D18** (1978) 1607.

[150] M. Block and J. D. Jackson, “Applications of a Cluster Decomposition of Many Dimensional Phase Space to High-Energy Collisions,” *Z.Phys.* **C3** (1980) 255.

[151] M. Srednicki, “Axion Couplings to Matter. 1. CP Conserving Parts,” *Nucl.Phys.* **B260** (1985) 689.

[152] H.-Y. Cheng, “Low-Energy Interactions of Scalar and Pseudoscalar Higgs Bosons with Baryons,” *Phys.Lett.* **B219** (1989) 347.

[153] M. E. Peskin and D. V. Schroeder, *An Introduction to quantum field theory.* Addison-Wesley, Reading, MA, 1995. pgs. 842.

[154] **HyperCP** Collaboration, H. Park *et al.*, “Observation of the decay $K^- \to \pi^- \mu^+ \mu^-$ and measurements of the branching ratios for $K^\pm \to \pi^\pm \mu^+ \mu^-$,” *Phys.Rev.Lett.* **88** (2002) 111801, `arXiv:hep-ex/0110033 [hep-ex]`.

[155] P. Gondolo, J. Edsjo, P. Ullio, L. Bergstrom, M. Schelke, *et al.*, “DarkSUSY: Computing supersymmetric dark matter properties numerically,” *JCAP* **0407** (2004) 008, `arXiv:astro-ph/0406204 [astro-ph]`.

[156] P. Ball and R. Zwicky, “$B_{d,s} \to \rho, \omega, K^*, \phi$ decay form-factors from light-cone sum rules revisited,” *Phys.Rev.* **D71** (2005) 014029, `arXiv:hep-ph/0412079 [hep-ph]`.

[157] M. C. Arnesen, B. Grinstein, I. Z. Rothstein, and I. W. Stewart, “A Precision model independent determination of $|V_{ub}|$ from $B \to \pi \ell \nu$,” *Phys.Rev.Lett.* **95** (2005) 071802, `arXiv:hep-ph/0504209 [hep-ph]`.

[158] C. Uhlemann and N. Kauer, “Narrow-width approximation accuracy,” *Nucl.Phys.* **B814** (2009) 195–211, `arXiv:0807.4112 [hep-ph]`.

[159] R. Young and A. Thomas, “Octet baryon masses and sigma terms from an SU(3) chiral extrapolation,” *Phys.Rev.* **D81** (2010) 014503, `arXiv:0901.3310 [hep-lat]`.

[160] **MILC** Collaboration, D. Toussaint and W. Freeman, “The Strange quark condensate in the nucleon in 2+1 flavor QCD,” *Phys.Rev.Lett.* **103** (2009) 122002, `arXiv:0905.2432 [hep-lat]`.

[161] **Particle Data Group** Collaboration, K. Nakamura *et al.*, “Review of particle physics,” *J.Phys.G* **G37** (2010) 075021. See the “Axions and other similar particles” minireview.

[162] **JLQCD** Collaboration, K. Takeda *et al.*, “Nucleon strange quark content from two-flavor lattice QCD with exact chiral symmetry,” *Phys.Rev.* **D83** (2011) 114506, `arXiv:1011.1964 [hep-lat]`.

[163] **JLQCD** Collaboration, K. Takeda *et al.*, "Nucleon strange quark content in 2+1-flavor QCD," *PoS* **LATTICE2010** (2010) 160, `arXiv:1012.1907 [hep-lat]`.

Appendix A

Exact Expressions for *ep* Scattering

A.1 Finite Mass Calculations

A.1.1 Anomalous Magnetic Moment

A new light boson, whether it is a scalar or vector, will contribute to the anomalous magnetic moment ($a = \frac{g-2}{2}$) of leptons at the one-loop level. In the low masses being considered for the X boson, limits on new contributions to the moment are the main indirect constraint and must be calculated accurately. In the scalar/pseudoscalar case, a convenient choice of parameterization yields [58]

$$\delta a_{s/p} = \frac{m_\ell^2}{16\pi^2}\int_0^1 dz \frac{\lambda_s^2(1-z)(1-z^2) - \lambda_p^2(1-z)^3}{zm_X^2 + (1-z)^2 m_\ell^2} \tag{A.1}$$

$$\approx \frac{1}{16\pi^2}\frac{m_\ell^2}{m_X^2}\left(\lambda_s^2\left(\log\frac{m_\ell^2}{m_X^2} - \frac{7}{6}\right) - \lambda_p^2\left(\log\frac{m_\ell^2}{m_X^2} - \frac{11}{6}\right)\right). \tag{A.2}$$

This final form only holds in the limit $m_\ell \ll m_X$, and is thus not appropriate for a_μ.

For the case of a vector coupling, the term proportional to $p^\mu p^\nu$ in the numerator of the propagator drops out of the calculation entirely due to the Ward identity. However, for axial coupling this is not the case. At the same time, the extra factor of $1/m_X^2$ this term introduces means it only contributes at $\mathcal{O}(m_e^4/m_X^4)$. Thus, it can be safely ignored in the electron case, but for constraints from the muon anomalous magnetic moment it must be included for accurate results. The full calculation yields [59]

$$\delta a_{v/a} = \frac{m_\ell^2}{16\pi^2}\int_0^1 dz \frac{4\lambda_v^2 z(1-z)^2 - 4\lambda_a^2\left(z(1-z)(3+z) + 2(1-z)^3\frac{m_\ell^2}{m_X^2}\right)}{zm_X^2 + (1-z)^2 m_\ell^2} \tag{A.3}$$

$$\approx \frac{1}{16\pi^2}\frac{m_\ell^2}{m_X^2}\left(\lambda_v^2\frac{4}{3} - \lambda_a^2\frac{20}{3}\right), \tag{A.4}$$

where again the approximate form only holds for $m_\ell \ll m_X$.

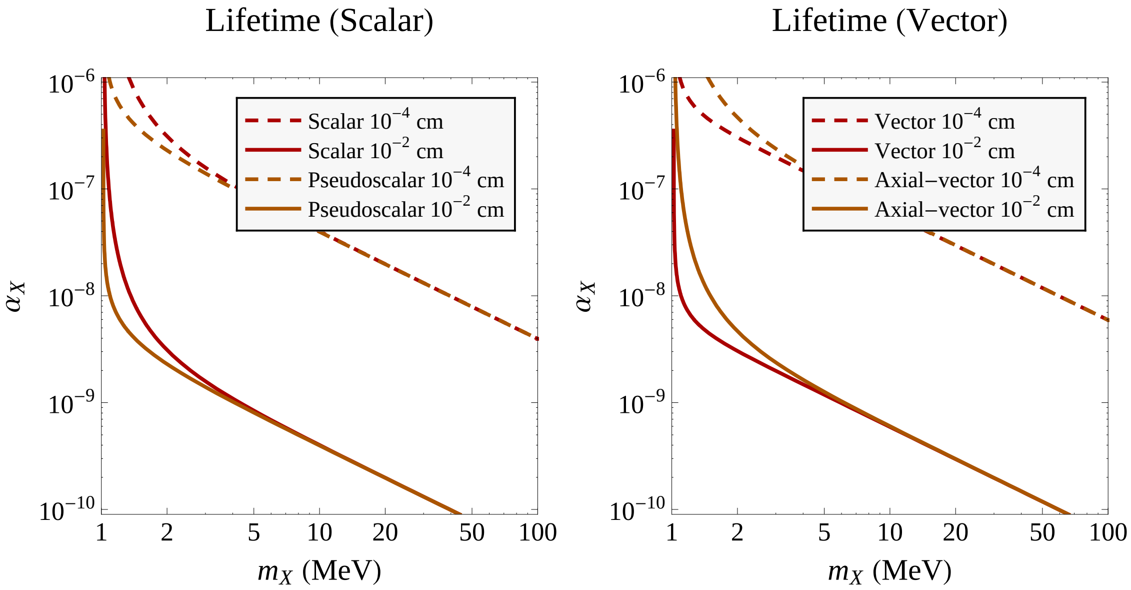

Figure A.1: Curves of constant X boson lifetime on the α_X vs. m_X plane.

A.1.2 Lifetime

If $m_X < 2m_\mu$, then for the couplings envisioned in Sec. 2.3, the only allowed decay mode of the X boson is $X \to e^+e^-$. In more general scenarios, the X boson might decay to neutrinos or photons or other new light fields, but such final states face very different backgrounds and are outside the scope of this study.

The tree-level widths from the couplings described in Sec. 2.3 are

$$\Gamma_{s/p} = \frac{m_X}{8\pi}\left((\lambda_s^2 + \lambda_p^2) - \lambda_s^2\frac{4m_e^2}{m_X^2}\right)\sqrt{1 - \frac{4m_e^2}{m_X^2}}, \tag{A.5}$$

$$\Gamma_{v/a} = \frac{m_X}{12\pi}\left((\lambda_v^2 + \lambda_a^2) + 2(\lambda_v^2 - 2\lambda_a^2)\frac{m_e^2}{m_X^2}\right)\sqrt{1 - \frac{4m_e^2}{m_X^2}}. \tag{A.6}$$

In the limit $m_e \ll m_X$, these simplify to $\Gamma_{s/p} = \frac{m_X}{8\pi}(\lambda_s^2 + \lambda_p^2)$ and $\Gamma_{v/a} = \frac{m_X}{12\pi}(\lambda_v^2 + \lambda_a^2)$. A plot of the X lifetime is shown in Fig. A.1 with full m_e dependence, which introduces small differences in the scalar/pseudoscalar and vector/axial-vector cases at masses close to the electron mass.

A.2 Signal Calculation

In this appendix, we review the narrow width approximation and apply it to X boson production. The signal for X boson production is $e^-p \to e^-p + X \to e^-p\,e^+e^-$. While other diagrams with internal X boson propagators can contribute to the $e^-p\,e^-e^+$ final state, only the diagrams shown in Fig. 2.5 yield a narrow peak in the e^+e^- invariant mass distribution near m_X.

It is well-known that processes involving a resonance with a small width can be treated by the so-called narrow width approximation (see Ref. [158] and references therein). In the case of X boson production, the idea is to write the square of the full two-to-four matrix element of diagrams in Fig. 2.5 as

$$|M(2 \to 4)|^2 = |\tilde{M}|^2(q, ...) \times D(q), \qquad D(q) = \frac{1}{(q^2 - m_X^2)^2 + \Gamma_X^2 m_X^2}, \tag{A.7}$$

where q is the four-momentum flowing through the X boson propagator. One then approximates the square of the X boson propagator as

$$D(q) \approx \frac{\pi}{m_X \Gamma_X} \delta(q^2 - m_X^2). \tag{A.8}$$

Using the cluster decomposition of four-body phase space into a product of three-body and two-body phase space,

$$\mathrm{d}\Phi_4 = \frac{1}{2\pi} \mathrm{d}\Phi_3 \, \mathrm{d}q^2 \, \mathrm{d}\Phi_2, \tag{A.9}$$

the fully differential cross section takes the form

$$\begin{aligned} \sigma_{\text{signal}} &= \frac{1}{F} \int \mathrm{d}\Phi_4 \frac{1}{4} \sum_{\text{spins}} |M(2 \to 4)|^2 \\ &= \frac{1}{F} \frac{1}{\Gamma_X} \int \mathrm{d}\Phi_3 \int \mathrm{d}\Phi_2 \frac{1}{4} \sum_{\text{spins}} |\tilde{M}(q, ...)|^2 \frac{1}{2m_X}. \end{aligned} \tag{A.10}$$

Here, F is the incoming flux, which in the case of a fixed target experiment with incoming electron energy E_e equals

$$F = 4 E_e m_p. \tag{A.11}$$

When the X boson has scalar or pseudoscalar couplings, the matrix element of the full two-to-four process takes a convenient factorized form:

$$|\tilde{M}(q, ...)_S|^2 = |M_S(2 \to 3)|^2 \, |M_S(1 \to 2)|^2. \tag{A.12}$$

For calculating the total cross section, one can perform the $\mathrm{d}\Phi_2$ integral in Eq. (A.10) analytically:

$$\sigma_{\text{signal scalar}} = \frac{1}{F} \int \mathrm{d}\Phi_3 \frac{1}{4} \sum_{\text{spins}} |M_S(2 \to 3)|^2 \left(\frac{\Gamma_{X \to e^+e^-}}{\Gamma_X} \right). \tag{A.13}$$

The factor in parentheses is just the branching fraction of X to the e^+e^- final state. Of course, for any real observable, there are always cuts present, at minimum on the detector geometry. So in practice, one must use the full formula in Eq. (A.10) and multiply the integrand by the desired observable function.

When the X boson has vector or axial-vector couplings, the matrix element does not factorize, but the amplitude does factorize into a contraction between the production of the resonance, the decay of the resonance, and the numerator of the X boson propagator:

$$|\tilde{M}_V(q, ...)|^2 = \left| M_V^\mu(2 \to 3) M_V^\nu(1 \to 2) \left(g_{\mu\nu} - \frac{q_\mu q_\nu}{M_X^2} \right) \right|^2. \tag{A.14}$$

It is worth mentioning that in the vector case, the $q_\mu q_\nu$ term in the propagator vanishes because of Ward identity:

$$q_\nu M_V^\nu(1 \to 2) = 0, \tag{A.15}$$

since the external electron/positron are on-shell. In the axial-vector case, the Ward identity is no longer true, but because of chiral symmetry, the correction from the $q_\mu q_\nu$ term is suppressed by powers of m_e and therefore small. Because of the X boson propagator factor, there are non-trivial angular correlations in the X boson decay.

There is one subtlety in using the narrow width approximation with identical particles in the final state. Experimentally, we cannot determine which final state electron came from the decay of the resonance and which one is the scattered incoming electron. Therefore, in principle, we must add to the diagrams in Fig. 2.5 another two diagrams with the electron legs in the final state interchanged. However, the effect of adding these diagrams but including a symmetry factor of 1/2 into the phase space for identical electrons leaves Eq. (A.10) unchanged. Since Eq. (A.10) is valid for all regions of phase space, the differential distribution in $m_{e^+e^-}$ will include not just a delta function spike at m_X, but also the correct combinatoric background. For any real experimental observable, this delta function spike will be properly smeared out by the experimental resolution, as long as the experimental resolution is coarser than Γ_X.

A.3 Background Calculation

The background to X boson production consists of quasi-elastic QED interactions, with example diagrams given in Fig. 2.6. Since we are considering incoming beam energies below the pion mass, no QCD interaction are relevant, and the proton remains intact after being struck by the electron. This simplifies the analysis of the standard model background to the proposed signal dramatically. Also, since our target is hydrogen gas, we do not have to worry about nuclear excitations.

Given that the background is QED, we can safely consider tree-level diagrams alone, since loops are suppressed by the small electromagnetic coupling. That said, while the one-loop corrections to the background are much smaller than the tree-level result, they are also expected to be much larger than our signal. However, one-loop corrections are not expected to dramatically change the shape of the background (and certainly not give a peak at finite $m_{e^+e^-}$), so for the purposes of extracting a signal peak in the invariant mass distribution, the tree-level background result will suffice.

The largest correction we are neglecting comes from the electric form factor of the proton

$$f_E(q^2) \simeq \left(\frac{m_0^2}{m_0^2 + q^2}\right)^2, \tag{A.16}$$

which had been included in the study in Ref. [51]. With $m_0 \sim 700$ MeV and $q \lesssim E_e = 100$ MeV, this will at most yield a 5% change in the background calculation. Like the one-loop effects, though, the electromagnetic form factor is not expected to dramatically change the background shape.

There are twelve QED diagrams that contribute to the process $e^- p \to e^- p\, e^+ e^-$. Just as in Møller scattering, one must be mindful that the interchange of identical fermionic legs adds an additional minus sign to the Feynman rules [153]. The background cross section equals

$$\sigma_{\text{background}}(\mathcal{O}) = \frac{1}{F} \int \mathrm{d}\Phi_4 \frac{1}{2}\frac{1}{4} \sum_{\text{spins}} |M_{\text{background}}|^2 \mathcal{O}(\Phi_4), \tag{A.17}$$

where 1/2 is a symmetry factor from having two identical electrons in the final state, 1/4 the average over initial polarizations and $\mathcal{O}(\Phi_4)$ is an arbitrary observable. Since, unlike the signal calculation, the narrow width approximation does not apply, no ad hoc steps need to be taken to account for combinatorics in the background. The factor of 1/2 above with a sum over all diagrams suffices to reproduce the full background.

In particular, for calculating the background in the signal bin for a given value of m_X, we use the theta function

$$\mathcal{O}(\Phi_4) = \theta\left((m_X - \Delta m/2)^2 < q^2 < (m_X + \Delta m/2)^2\right), \tag{A.18}$$

where q^2 is the invariant mass of an outgoing e^+e^- pair, and Δm is the invariant mass resolution. (Since there are two outgoing electrons, this theta function could pick up either e^+e^- pair.) Because the background is a steeply falling distribution in q^2, as shown in Fig. 2.12, this way of calculating the binned background gives slightly more realistic values than

$$\mathcal{O}(\Phi_4) = 2 m_X \Delta m\, \delta(q^2 - m_X^2), \tag{A.19}$$

though both measurements agree in the small Δm limit.

A.4 Matrix Element Method

In this appendix, we derive the ideal weighting function to be used in the matrix element method from Sec. 2.4.3. To start, consider an unweighted measurement

$$S = \int \mathrm{d}\Phi\, S(\Phi), \qquad B = \int \mathrm{d}\Phi\, B(\Phi). \tag{A.20}$$

The statistical uncertainty in the background δB can be determined in terms of the Poisson uncertainty at each point in phase space $\delta B(\Phi)$,

$$\delta B(\Phi) = \sqrt{B(\Phi)}, \qquad \delta B = \sqrt{\int \mathrm{d}\Phi \, [\delta B(\Phi)]^2} = \sqrt{B}, \tag{A.21}$$

and we recover the familiar formula that $S/\delta B = S/\sqrt{B}$.[1]

Now imagine doing a weighted measurement over phase space:

$$S_{\text{eff}} = \int \mathrm{d}\Phi \, S(\Phi) w(\Phi), \qquad B_{\text{eff}} = \int \mathrm{d}\Phi \, B(\Phi) w(\Phi). \tag{A.22}$$

The statistical uncertainty in B_{eff} is

$$\delta B_{\text{eff}} = \sqrt{\int \mathrm{d}\Phi \, [\delta B(\Phi)]^2 \, w(\Phi)^2} = \sqrt{\int \mathrm{d}\Phi \, B(\Phi) w(\Phi)^2}. \tag{A.23}$$

Note that the reach in $S_{\text{eff}}/\delta B_{\text{eff}}$ is independent of the normalization of $w(\Phi)$.

To find the ideal measurement function, we simply need to use a variational method to solve for the condition

$$\frac{\mathrm{d}}{\mathrm{d}w(\Phi)} \left(\frac{S_{\text{eff}}}{\delta B_{\text{eff}}} \right) = 0. \tag{A.24}$$

Using the fact that

$$\frac{\mathrm{d}}{\mathrm{d}w(\Phi)} S_{\text{eff}} = S(\Phi), \qquad \frac{\mathrm{d}}{\mathrm{d}w(\Phi)} \delta B_{\text{eff}} = \frac{B(\Phi) w(\Phi)}{\delta B_{\text{eff}}}, \tag{A.25}$$

it is straightforward to solve Eq. (A.24) to find

$$w_{\text{best}}(\Phi) = \frac{(\delta B_{\text{eff}})^2}{S_{\text{eff}}} \frac{S(\Phi)}{B(\Phi)} \Rightarrow \frac{S(\Phi)}{B(\Phi)}, \tag{A.26}$$

where we have used the fact that the overall normalization of $w_{\text{best}}(\Phi)$ is irrelevant for determining the reach. Plugging $w_{\text{best}}(\Phi)$ into $S_{\text{eff}}/\delta B_{\text{eff}}$, we find

$$\left[\frac{S_{\text{eff}}}{\delta B_{\text{eff}}} \right]_{\text{best}} = \sqrt{\int \mathrm{d}\Phi \, \frac{S(\Phi)^2}{B(\Phi)}}. \tag{A.27}$$

For $S(\Phi)$ proportional to $B(\Phi)$ (i.e. no kinematic shape differences between the signal and background), this formula reverts to the standard $S/\sqrt{B}$.

---

[1] Strictly speaking, we should really consider statistical uncertainties in both the signal and background, but the background is so much larger than the signal that this is superfluous.

When we plot the weighting function in Figs. 2.14, 2.15, 2.16, and 2.17, we are actually plotting

$$\int \mathrm{d}\Phi \, w_{\mathrm{best}}(\Phi) \, \mathcal{O}(\Phi), \tag{A.28}$$

where $\mathcal{O}(\Phi)$ is the observable corresponding to a histogram bin. As a cross check of the weighting function, we checked that for most observables, this function is well-approximated by

$$\frac{\int \mathrm{d}\Phi \, S(\Phi) \, \mathcal{O}(\Phi)}{\int \mathrm{d}\Phi \, B(\Phi) \, \mathcal{O}(\Phi)} \int \mathrm{d}\Phi \, \mathcal{O}(\Phi), \tag{A.29}$$

i.e. the binned signal over background ratio corrected by a phase space volume factor.

A.5 Generalized Couplings

In order to study the X boson phenomenology in a model-independent way, we assumed in Sec. 2.3 that the X boson only had couplings to electrons and not to protons. Here, we relax this assumption within the context of several proposed models, to see how the X boson reach using ep scattering is affected. We find that, for varying reasons, couplings to the proton can be ignored.

A.5.1 Kinematic Mixing

In some of the best motivated dark force scenarios, the couplings of the X boson are proportional to the electromagnetic couplings [28, 29]. This occurs when the X is a vector boson that kinematically mixes with the photon. That is, the vector X_μ couples directly to the electromagnetic current, albeit with a suppression factor ϵ,

$$\mathcal{L} = \epsilon g_{\mathrm{em}} J^{\mu}_{\mathrm{em}} X_{\mu}. \tag{A.30}$$

This yields $\alpha_X = \epsilon^2 \alpha_{\mathrm{EM}}$, where in concrete models, typical ϵ values are 10^{-3} to 10^{-4}.[2]

Adding the X boson coupling to the proton allows for additional diagrams for X boson production. Therefore, there is the potential for noticeable contributions to the signal cross section from the proton coupling, whether through a direct contribution to the cross section or through constructive or destructive interference. By explicit computation, however, we have checked that the proton coupling is largely irrelevant, and the essential physics can be understood by working out the kinematics of the relevant situations.

The two differences in producing an X off the photon or electron are the presence of an electron versus a proton propagator and the momentum transfer through the exchanged t-channel photon. If one notes that neither the proton nor the X boson are very relativistic in the energy range under consideration, one can approximately say that $E_p \simeq m_p$, $E_X \simeq m_X$,

---

[2] In these models, the typical X boson mass is around 1 GeV. However, models with lighter X bosons closer to 100 MeV are still plausible.

and $E_e \simeq m_X$ at any point along the electron line. Then, the fermion propagator can be shown to be $\mathcal{O}(1/m_X)$ in both cases. However, by seeing how momentum flows through the t-channel photon propagator, one can show that in the case of X boson production off the electron line, $|t| \simeq \mathcal{O}(m_X^2)$, while off the proton line, $|t| \simeq \mathcal{O}(m_X m_p)$. Thus, the cross section for X boson production off the proton line is suppressed by $\mathcal{O}(m_X^2/m_p^2)$.

This suppression can be understood intuitively as arising from the fact that with a proton at rest, enough energy needs to be exchanged in the t-channel to actually create an X boson, while with the electron already having sufficient energy, one only needs enough momentum transfer to move the electron into a kinematically valid region for X radiation.

One might worry that because of interference terms, the suppression would only be $\mathcal{O}(m_X/m_p)$. However, in addition to the mass dependence, the momentum exchanged through the t-channel photon has angular dependence. This is minimized when the X boson is produced collinearly with the fermion line off which it is produced. This means that the matrix elements for X production off the electron and off the proton are peaked in entirely different regions of phase space, producing little overlap. The interference terms end up being suppressed by another 2 orders of magnitude when the diagrams are explicitly calculated and integrated over. Thus for $m_X \lesssim 100$ MeV, the corrections to the cross sections from including proton couplings are around 1%, and do not measurably change the reach plots displayed earlier.

A.5.2 Axion-Like Coupling

An alternative framework for the X boson is where the dark sector couples to the standard model through a pseudo Nambu-Goldstone boson, termed an axion portal [30]. In that case, one expects a coupling of $\lambda_p = m_\ell/f_a$ for elementary fermions, where f_a is the axion decay constant. In such a setup, the constraints from the muon anomalous magnetic moment completely rules out the region of electron couplings that might be probed in our setup, as discussed in Sec. 2.3.1.

However, most axion portal models predict couplings of $\lambda_p \sim m_f/f_a$ for composite particles like the proton. Thus, with the coupling to the proton $\mathcal{O}(10^3)$ greater than to the electron, one might think it possible to still see a signal from X boson production off the proton, despite the kinematic suppression discussed above. It turns out, though, that a decay constant small enough for this to be possible has already been ruled out by K decay branching ratios [154], which placed a lower bound of $f_a = \mathcal{O}(100 \text{ TeV})$ for axion masses $\leq 2\mu$. This leads to a coupling to the proton of at most $\alpha_X = \mathcal{O}(10^{-10})$ which, combined with the kinematic suppression, would not be detectable with this search.

Appendix B

Decay Rates for *B* Mesons

In this appendix, we list the B decay rates to $K^{(*)}A^0$ and X_sA^0 in the 2HDM, using the effective Hamiltonian in Eq. (3.12). These should be combined with Eq. (3.14) to bound the axion models.

Defining

$$\Gamma_0 = \frac{G_F^3 |V_{ts}^* V_{tb}|^2}{\sqrt{2}\, 2^{12}\, \pi^5}\, m_t^4\, m_B^3 \big(X_1 \cot\beta + X_2 \cot^3\beta\big)^2, \tag{B.1}$$

and

$$\lambda_{K^{(*)}} = \sqrt{\big(m_B^2 - m_{A^0}^2 - m_{K^{(*)}}^2\big)^2 - 4 m_{A^0}^2 m_{K^{(*)}}^2}\,, \tag{B.2}$$

the $B \to KA^0$ decay rate is given by

$$\Gamma(B \to KA^0) = \Gamma_0\, \frac{\lambda_K (m_B^2 - m_K^2)^2}{m_B^6} \big[f_0(m_{A^0}^2)\big]^2. \tag{B.3}$$

The $B \to K^* a$ decay rate is

$$\Gamma(B \to K^* A^0) = \Gamma_0\, \frac{\lambda_{K^*}^3}{m_B^6} \big[A_0(m_{A^0}^2)\big]^2. \tag{B.4}$$

In both decays we used the standard definitions [101] of the form factors,

$$\begin{aligned} \langle K(p-q)| \bar{s}\, \not{q} P_L b\, |B(p)\rangle &= \frac{1}{2}(m_B^2 - m_K^2)\, f_0(q^2)\,, \\ \langle K^*(p-q)| \bar{s}\, \not{q} P_L b\, |B(p)\rangle &= -i\, m_{K^*} (\varepsilon^* \cdot p)\, A_0(q^2)\,. \end{aligned} \tag{B.5}$$

(We caution the reader not to confuse A^0 and A_0, each of which are standard in the respective contexts.)

In Eq. (B.1) it is the $\overline{\text{MS}}$ top quark mass which enters, appropriate both for the coupling to Higgses and in loop integrals. While this distinction is formally a higher order correction, since the rates are proportional to m_t^4, we use the Tevatron average top mass, converted to $\overline{\text{MS}}$ at one-loop, $\overline{m}_t = m_t[1 - 4\alpha_s/(3\pi)] \approx 165$ GeV.

The largest hadronic uncertainty in evaluating the implication of the bound in Eq. (3.15) is the model dependence in the calculations of the form factor $f_0(m_a^2)$, which is an increasing function of q^2. For $f_0(0)$, QCD sum rule calculations obtain values around 0.33, with an order 10% uncertainty [108]. To be conservative, in evaluating the bound on f_a, we only assume $f_0(0) > 0.25$ for $m_a \ll m_B$ (which also covers lower values motivated by SCET-based fits [157]). For $m_a \gtrsim 2m_\tau$, relevant for Eq. (3.18), we use the approximation $f_0(q^2) = f_0(0)/(1 - q^2/37.5\ \text{GeV}^2)$ [108], which should be good enough for our purposes. For recent QCD sum rule calculations of $A_0(q^2)$, relevant for setting a bound using $B \to K^* \ell^+ \ell^-$, see Ref. [156].

The inclusive $B \to X_s\, a$ decay rate, which can be calculated (strong interaction) model independently in an operator product expansion, is given at leading order in Λ_{QCD}/m_b by

$$\Gamma(B \to X_s A^0) = 2\Gamma_0\, \frac{m_b^3}{m_B^3} \left(1 - \frac{m_{A^0}^2}{m_b^2}\right). \tag{B.6}$$

Appendix C

Dark Matter Detection Formulæ

C.1 Nuclear Matrix Elements

Here we summarize how to compute the dark matter-nucleon interaction cross sections from quark-level interactions. Much of this has been discussed in the DM literature, with the exception of the pseudoscalar matrix element, as it only plays a role in momentum suppressed cross sections.

For a vector coupling, nuclear matrix elements are straightforward to compute, since a vector coupling to quarks is a conserved current, so the coupling to a nucleon is obtained from the sum of the currents of the valence quarks.

In the case of a scalar coupling to quarks, we are interested in the effective nucleon coupling induced by a quark level coupling:

$$a_q \, m_q \, \bar{q}q \quad \rightarrow \quad f_N \, m_N \, \bar{N}N. \tag{C.1}$$

We define the nuclear matrix elements conventionally by

$$\langle N|m_q\bar{q}q|N\rangle = m_N f_{Tq}^{(N)}. \tag{C.2}$$

On including the coupling to gluons induced by integrating out heavy quark loops, f_N is given by

$$f_N = \sum_{q=u,d,s} f_{Tq}^{(N)} \, a_q + \frac{2}{27} f_{TG}^{(N)} \sum_{q=c,b,t} a_q \, , \tag{C.3}$$

where $f_{TG}^{(N)} = 1 - \sum_{q=u,d,s} f_{Tq}^{(N)}$.

Unlike the u and d matrix elements, which can be extracted from πN scattering, the uncertainty associated with the strange quark matrix element $f_{Ts}^{(N)}$ is higher, which introduces a substantial uncertainty in the SI coupling to nucleons. Most studies use numerical values $f_{Ts}^{(N)} \gg f_{Tu,d}^{(N)}$ based on older calculations. A representative set of values is that used by the

DarkSUSY package [155], wherein,

$$f_{Tu}^{(p)} = 0.023\,, \quad f_{Td}^{(p)} = 0.034\,, \quad f_{Ts}^{(p)} = 0.14\,,$$
$$f_{Tu}^{(n)} = 0.019\,, \quad f_{Td}^{(n)} = 0.041\,, \quad f_{Ts}^{(n)} = 0.14\,. \tag{C.4}$$

These are the values used for the numerical estimates given above, and in most of the literature. However, recent lattice QCD results give substantially smaller values, $f_{Ts}^{(N)} = 0.013 \pm 0.020$ [162, 163] (see also [159, 160]), and so the SI cross section from scalar exchange (if it couples proportionally to mass) may be smaller by a factor of $2-5$ than numerical results quoted by many calculations.

For SD interaction we need to consider the nuclear matrix elements induced by the quark level axial-vector and pseudoscalar couplings,

$$d_q\,\bar{q}\gamma_\mu\gamma^5 q \quad \to \quad a_N\,\bar{N}s_\mu^{(N)}N, \tag{C.5}$$

and

$$c_q\,m_q\,\bar{q}i\gamma^5 q \quad \to \quad g_N\,m_N\,\bar{N}i\gamma^5 N. \tag{C.6}$$

For the axial-vector current, defining

$$\langle N|\bar{q}\gamma_\mu\gamma^5 q|N\rangle = s_\mu^{(N)}\Delta q^{(N)}, \tag{C.7}$$

where $s_\mu^{(N)}$ is the spin of the nucleon, we have

$$a_N = \sum_{q=u,d,s} d_q\,\Delta q^{(N)}. \tag{C.8}$$

The matrix elements coming from polarized deep inelastic scattering carry much smaller uncertainties than for the scalar SI interaction above. For our numerical results, we use again the DarkSUSY values,

$$\Delta u^{(p)} = \Delta d^{(n)} = 0.77\,,$$
$$\Delta d^{(p)} = \Delta u^{(n)} = -0.40\,,$$
$$\Delta s^{(p)} = \Delta s^{(n)} = -0.12\,. \tag{C.9}$$

More recent determinations favor slightly different values, and the PDG quotes $\Delta s^{(n)} = -0.09$, $\Delta d^{(n)} = 0.84$, $\Delta u^{(n)} = -0.43$, with a 0.02 uncertainty for each [161]; the effect on our numerical results is negligible.

For the pseudoscalar current in Eq. (C.6) the nucleon-level coupling is determined by the same axial-vector matrix elements above. The relationship is established through generalized Goldberger–Treiman relations. While not normally considered in dark matter detection, it has been well-studied in the axion literature [151, 149]. Taking divergences of the axial currents and using the equations of motion for the quarks yields [152]

$$\begin{aligned} g_N = {} & (c_u - \bar{c}_q\eta)\,\Delta u^{(N)} \\ & + (c_d - \bar{c}_q\eta z)\,\Delta d^{(N)} + (c_s - \bar{c}_q\eta w)\,\Delta s^{(N)}\,, \end{aligned} \tag{C.10}$$

where $\eta = (1 + z + w)^{-1}$, $z = m_u/m_d$, and $w = m_u/m_s$, while $\bar{c}_q$ is the mean of the quark coupling coefficients. Due to uncertainties in the value of z, the value of g_N can vary by as much as a factor of 2.

C.2 Cross Sections

In this Appendix, we provide a summary of cross sections for DM-nucleon interactions relevant for calculating the various cross sections discussed above in the non-relativistic limit.

We first consider the unsuppressed operors in the limit of zero momentum transfer. SI cross sections can come from either scalar or vector quark couplings. Effective DM-nucleon scalar interactions for fermions of the form

$$f_N \, \bar{\chi}\chi \, \bar{N}N, \tag{C.11}$$

which are derived from the quark-level couplings using nuclear matrix elements, as explained in App. C.1, lead to a DM-nucleus cross section

$$\hat{\sigma} = \frac{4}{\pi} \, \hat{\mu}^2 \big[Z f_p + (A - Z) f_n \big]^2, \tag{C.12}$$

for Majorana DM fermions. (For Dirac fermions, all results for Majorana fermions are divided by 4.) Here $\hat{\mu}$ is the reduced mass of the DM-nucleus system. The per-nucleon cross section, which is usually quoted for comparisons, is

$$\sigma = \frac{4}{\pi} \, \mu^2 \frac{1}{A^2} \big[Z f_p + (A - Z) f_n \big]^2, \tag{C.13}$$

where μ is the reduced mass of the DM-nucleon system.

For scalar or vector dark matter, the relevant operators are (we include the DM mass to give all operators the same dimension)

$$f_N \, m_\phi \, \phi\phi \, \bar{N}N \quad \text{or} \quad f_N \, m_B \, B^\mu B_\mu \, \bar{N}N, \tag{C.14}$$

the nucleon cross section for either operator is

$$\sigma = \frac{1}{\pi} \, \mu^2 \frac{1}{A^2} \big[Z f_p + (A - Z) f_n \big]^2. \tag{C.15}$$

Vector interactions for fermions only exist in the case of Dirac DM:

$$b_N \, \bar{\chi}\gamma^\mu\chi \, \bar{N}\gamma_\mu N, \tag{C.16}$$

where, $b_p = 2b_u + b_d$ and $b_n = b_u + 2b_d$, due to vector current conservation, as discussed above in App. C.1. Then

$$\sigma = \frac{1}{\pi} \, \mu^2 \frac{1}{A^2} \big[Z b_p + (A - Z) b_n \big]^2. \tag{C.17}$$

For the operators

$$b_N\,\phi^\dagger\partial_\mu\phi\,\bar{N}\gamma^\mu N \quad \text{or} \quad b_N\,B_\nu^\dagger\partial_\mu B^\nu\,\bar{N}\gamma^\mu N, \tag{C.18}$$

which only exist for complex scalars or vectors, the cross section is

$$\sigma = \frac{1}{\pi}\,\mu^2\frac{1}{A^2}\big[Zb_p + (A-Z)b_n\big]^2. \tag{C.19}$$

Unsuppressed SD interactions come solely from the quarks' axial currents. In the case of

$$a_N\,\bar{\chi}\gamma^\mu\gamma^5\chi\,\bar{N}\gamma_\mu\gamma^5 N, \tag{C.20}$$

the DM-nucleus cross section is

$$\hat{\sigma} = \frac{16}{\pi}\,\hat{\mu}^2\,a_N^2\,J_N(J_N+1), \tag{C.21}$$

and for a nucleon

$$\sigma = \frac{12}{\pi}\,\mu^2\,a_N^2. \tag{C.22}$$

The only other unsuppressed SD interaction is for vector DM and comes from

$$a_N\,\epsilon^{\mu\nu\sigma\rho}B_\mu\partial_\nu B_\sigma\,\bar{N}\gamma_\rho\gamma^5 N\,. \tag{C.23}$$

Here, the DM-nucleon cross section is

$$\sigma = \frac{2}{\pi}\,\mu^2\,a_N^2. \tag{C.24}$$

All of the above cross sections are quoted in the $q^2 \to 0$ limit. In this limit, interactions mediated by light pseudoscalars are all zero, so we need another way of expressing such cross sections. To do so, we will use the fact that while in the nonrelativistic limit $\bar{\psi}\psi \sim 2m$, $\bar{\psi}\gamma^5\psi \sim q^i\xi^\dagger\sigma^i\xi$, so that using the results above we can write (since $q^2 \approx |\vec{q}|^2$ in the nonrelativistic limit).

$$\bar{\chi}\gamma^5\chi\,\bar{N}\gamma^5 N \sim \frac{q^2}{4m_\chi^2}\,\frac{q^2}{4m_N^2}\,\bar{\chi}\gamma^\mu\gamma^5\chi\,\bar{N}\gamma_\mu\gamma^5 N\,. \tag{C.25}$$

We then compute the cross section as above, and quote a result at a reference value of q^2. We have chosen $q^2 = (100\text{ MeV})^2$ since with $q^2 = 2m_N E_R$, where E_R is the recoil energy of the nucleus, this is a typical value for most SD detectors. Other momentum-suppressed operators can be handled the same way.